ISSN 0016-2523

FUJITSU SCIENTIFIC & TECHNICAL JOURNAL

Winter 1991 VOL. 27, NO. 4

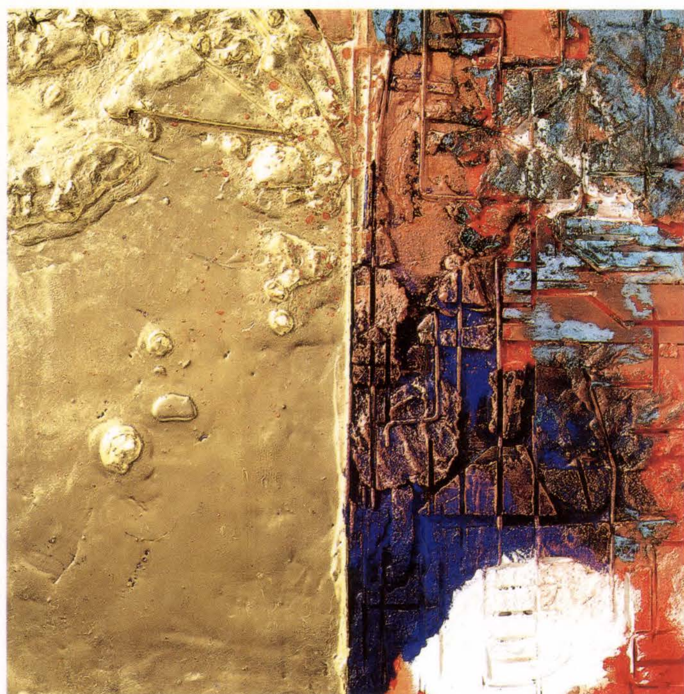

FUJITSU Sci. Tech. J., **27**, 4, pp. 299-378, Kawasaki Winter, 1991

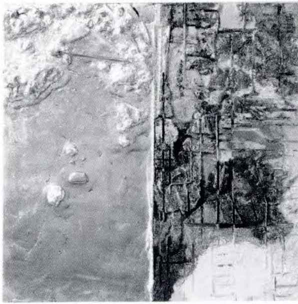

The Issue's Cover :
Phase by Hirofumi OHKUMA
When supercooled water changes from the liquid to solid phase, the change is rapid.
One molecule sets off a chain reaction that results in an expansion due to the supercooling energy.

FUJITSU Scientific & Technical Journal is published quarterly by FUJITSU LIMITED of Japan to report the results of research conducted by FUJITSU LIMITED, FUJITSU LABORATORIES LTD., and their associated companies in communications, electronics, and related fields. It is the publisher's intent that FSTJ will promote the international exchange of such information, and we encourage the distribution of FSTJ on an exchange basis. All correspondence concerning the exchange of periodicals should be addressed to the editor.

FSTJ can be purchased through KINOKUNIYA COMPANY LTD., 38-1, Sakuragaoka 5-Chome, Setagaya-ku, Tokyo 156, Japan, (Telephone : +81-3-3439-0162, Facsimile : +81-3-3706-7479).

The price is US$7.00 per copy, excluding postage.

FUJITSU LIMITED reserves all rights concerning the republication and publication after translation into other languages of articles appearing herein.

Permission to publish these articles may be obtained by contacting the editor.

FUJITSU LIMITED Tadashi Sekizawa, President
FUJITSU LABORATORIES LTD. Mikio Ohtsuki, President

Editorial Board
Editor Shigeru Sato
Associated Editor Hideo Takahashi
Editorial Representatives

Sadao Fujii, Tetsuya Isayama, Ken-ichi Itoh
Yoshihiko Kaiju, Yoshimasa Miura, Makoto Mukai
Yasushi Nakajima, Hiroshi Nishi, Hajime Nonogaki
Seiya Ogawa, Shinji Ohkawa, Shinya Okuda
Hirofumi Okuyama, Teruo Sakurai, Tohru Sato
Yoshio Tago, Shozo Taguchi, Hirobumi Takanashi
Mitsuhiko Toda, Toru Tsuda, Takao Uehara
Akira Yoshida

Editorial Coordinators
Yukichi Iwasaki
Kazuo Yono

FUJITSU LIMITED 1015 Kamikodanaka, Nakahara-ku,
Kawasaki 211, Japan
Cable Address : FUJITSULIMITED KAWASAKI
Telephone : +81-44-777-1111
Facsimile : +81-44-754-3562

Printed by MIZUNO PRITECH Co., Ltd. in Japan
© 1991 FUJITSU LIMITED (December 14, 1991)

SCIENTIFIC & TECHNICAL JOURNAL

Winter 1991 VOL.27, NO.4

CONTENTS

Reviews

299 **Photoexcited Processes for Semiconductors I: Low Temperature Epitaxy**
• Tatsuya Yamazaki • Takashi Ito

317 **Photoexcited Processes for Semiconductors II: Dry Cleaning and Dry Etching**
• Yasuhisa Sato • Rinshi Sugino • Takashi Ito

329 **Semiconductor Laser Light Sources and Receivers for Next Generation Optical Communication Systems**
• Hiroshi Ishikawa

Papers

338 **Report on Computer Algebra Research**
• Taku Takeshima • Masayuki Noro • Kazuhiro Yokoyama

360 **Boron/Magnesium Sintered Composites for Computer Peripherals**
• Eiji Horikoshi • Takehiko Sato

369 **Moving-Fiber Optical Switch Using $LiNbO_3$ Piezoelectric Actuator**
• Noboru Wakatsuki • Hisashi Sawada • Masanori Ueda

UDC 621.3.049.771.14.002.2
FUJITSU Sci. Tech. J., **27**, 4. pp. 299-316(1991)

Photoexcited Processes for Semiconductors I: Low Temperature Epitaxy

• Tatsuya Yamazaki • Takashi Ito

Photoenhanced processing promotes low-temperature growth of Si epitaxial layers. Irradiation of the wafer surface with high power UV light excites both the vapor phase reactions of the disilane source gas and the surface reactions; this reduces the crystal growth temperature to 500 °C and increases the growth rate. Here authors report that heavy boron doping up to 1×10^{20} cm^{-3} produced superior crystal quality at 500 °C with an abrupt impurity profile. Photoexcitation allowed also low-temperature selective epitaxy without microfacets or crystal defects.

A photoenhanced low-temperature epitaxial layer-used in high-speed bipolar transistors achieved a cutoff frequency of 43 GHz, and a 1/8-static frequency divider using the transistors operated up to 11.8 GHz.

UDC 621.3.049.771.14.002.2
FUJITSU Sci. Tech. J., **27**, 4, pp. 317-328(1991)

Photoexcited Processes for Semiconductors II: Dry Cleaning and Dry Etching

• Yasuhisa Sato • Rinshi Sugino • Takashi Ito

A photoexcited dry cleaning process using highly purified chlorine gas was developed as an ultraclean process for silicon ultra-large scale integrated-circuit (ULSI) production. The process aids in deep-submicron device fabrication. Metallic contaminants remaining on a wafer's surface after wet cleaning can be significantly reduced by photoexcited cleaning. Photoexcited cleaning can also remove contaminants that have penetrated the silicon substrate during reactive-ion processing by etching the contaminated layer without damaging the uncontaminated layer. Thus, dry cleaning improves thin gate oxide integrity, SiO_2-Si interface quality, carrier lifetime, junction leakage characteristics, and epitaxial film quality.

UDC 621.383.5:621.391.6
FUJITSU Sci. Tech. J., **27**, 4, pp. 329-337(1991)

Semiconductor Laser Light Sources and Receivers for Next Generation Optical Communication Systems.

• Hiroshi Ishikawa

Laser light sources and receivers for the next generation of optical communication systems currently being developed in Fujitsu Laboratories Ltd. are reviewed. A modulator integrated DFB laser and APD for high-speed systems, and multielectrode DFB laser and balanced receivers for coherent communication systems are described.

UDC 512.714:681.32
FUJITSU Sci. Tech. J., **27**, 4, pp. 338-359(1991)

Report on Computer Algebra Research

• Taku Takeshima • Masayuki Noro • Kazuhiro Yokoyama

Computer algebra is a newly developing research area that bridges constructive mathematics and scientific information processing technology. Research in this area includes design, analysis, and prototyping of mathematical algorithms for symbolic and algebraic computation.

This paper describes an experimental system for computer algebra, named *risa* — *Research Instrument for Symbolic Algebra*. At present, the system forms the basic kernel of a computer algebra system, and is expected to become an essential engine for advanced future systems. As a general-purpose computer algebra system, risa's operating speed is competitive and sometimes outstanding. This paper also briefly describes several mathematical results of some algebraic computations related mainly to polynomials.

UDC 620.168:681.327.634
FUJITSU Sci. Tech. J., **27**, 4, pp. 360-368(1991)

Boron/Magnesium Sintered Composites for Computer Peripherals

• Eiji Horikoshi • Takehiko Sato

A magnesium-based sintered composite, reinforced with boron particles, has been developed that has an increased modulus of elasticity and controllable thermal expansion coefficient. A 6vol%boron/magnesium-9wt% aluminum composite has an excellent modulus of elasticity 1.3 times that of the ordinary magnesium alloy and a thermal expansion coefficient close to aluminum alloy. This composite also has improved machinability as the size of the boron particles is controlled. A head-arm component for a disk drive was experimentally produced using this composite, and it was found that the composite causes greatly decreased thermal off-track error in the disk drive.

UDC 621.395.65:621.391.6
FUJITSU Sci. Tech. J., **27**, 4, pp. 369-378(1991)

Moving-Fiber Optical Switch Using $LiNbO_3$ Piezoelectric Actuator

• Noboru Wakatsuki • Hisashi Sawada • Masanori Ueda

The need for a fast, miniaturized, optical switch with low insertion loss has increased with the proliferation of optical communications and optical signal processing. This paper describes a moving-fiber optical switch consisting of a $LiNbO_3$ piezoelectric actuator having an anti-polarized ferroelectric laminar domain (inversion layer). A new construction technique simplifies optical axis alignment and makes fiber end-face polishing unnecessary. A 2 x 2 moving-fiber optical switch constructed using the above techniques has an insertion loss within 0.8 dB and a switching time less than 10 ms.

REVIEW

UDC 621.3.049.771.14.002.2

Photoexcited Processes for Semiconductors I: Low Temperature Epitaxy

● Tatsuya Yamazaki ● Takashi Ito *(Manuscript received August 7, 1991)*

Photoenhanced processing promotes low-temperature growth of Si epitaxial layers. Irradiation of the wafer surface with high power UV light excites both the vapor phase reactions of the disilane source gas and the surface reactions; this reduces the crystal growth temperature to 500 °C and increases the growth rate. Here authors report that heavy boron doping up to 1 x 10^{20} cm^{-3} produced superior crystal quality at 500 °C with an abrupt impurity profile. Photoexcitation allowed also low-temperature selective epitaxy without microfacets or crystal defects.

A photoenhaced low-temperature epitaxial layer-used in high-speed bipolar transistors achieved a cutoff frequency of 43 GHz, and a 1/8-static frequency divider using the transistors operated up to 11.8 GHz.

1. Introduction

High-performance integrated circuits need to be made smaller, both laterally and vertically. To achieve submicron design and ultrashallow junction depth, device fabrication temperatures must be lowered. In particular, the Si epitaxial growth process has the highest process temperature of all the device fabrication processes, and this must be lowered to form abrupt impurity profiles and to eliminate contamination. The Si epitaxial process temperature is usually above 1 000 °C[1], but this causes extensive impurity diffusion, and hence the conventional epitaxial process cannot be used once the device impurity profiles have already been made. This process is therefore only used in the initial stages of making the device. The high temperatures also cause metal and oxygen contamination, and degrade crystal quality.

Low-temperature epitaxial growth can be used in the intermediate and final stages of device processing to form the base and emitter regions of bipolar transistros, the source and drain in MOSFETs, and for metallization. There are many ways to make new device structures, and low-temperature epitaxy has great potential for improving the performance and packing density of LSI chips.

Many methods of lowering the growth temperature have already been investigated. For example, instead of using $SiCl_4$ for the source gas in conventional epitaxy, SiH_2Cl_2 or SiH_4 is used[2),3)]. These source gases reduce the growth temperature to 900 °C. Below 900 °C, however, crystal quality deteriorates and poly-Si begins to grow instead of single Si crystals.

Molecular beam epitaxy (MBE) has also been developed to lower growth temperatures[4)-6)]. Using MBE, an Si epitaxial layer can be grown under ultrahigh vacuum (UHV), thus reducing the growth temperature to about 600 °C. However, the equipment required for low-temperature MBE is very complex and the unit cost is too high for device fabrication. Furthermore, the crystal quality grown using MBE is not yet good enough for device fabrication.

Another method uses ultrahigh vacuum/chemical vapor deposition (UHV/CVD)[7)-9)].

This method successfully lowers the growth temperature to 500 °C while still retaining device-quality crystals, but the growth rate in the low temperature region is very small.

Other low-temperature epitaxial growth methods using enhanced processes have also been developed. Plasma-enhanced CVD epitaxy lowers the growth temperature to about 750 °C[10)-13)], but charged particle remaining at the substrate surface cause serious damage and crystal defects. However, photoenhanced epitaxy does not cause such damage, and there are two types: photosensitized or direct photolysis[14)-17)]. The former method uses mercury sensitized photolysis to reduce the growth temperature to 250 °C, but the epitaxial films grown contain a large concentration of hydrogen atoms, and the crystal quality is very poor. We therefore used the latter type of photoenhanced epitaxy, direct photolysis.

This paper describes photoepitaxial growth characteristics at both atmospheric pressure and at reduced pressure, including photoenhanced low-temperature selective epitaxy under ultrahigh vacuum. The paper also describes the details of heavy boron doping during photoepitaxy and the application of this process to bipolar transistors.

2. Photoepitaxy at atmospheric pressure

This chapter describes photoenhanced epitaxy at atmospheric pressure using conventional epitaxy equipment with few modifications (see Fig. 1)[18)]. An ultrahigh-pressure short-arc mercury lamp was used as the UV source, and the mercury light was attenuated in the visible and infrared wavelengths by using a cold mirror (selective reflection mirror). The mercury light then had a wavelength range between 185 nm and 260 nm (see Fig. 2). The UV light irradiated the wafer surface vertically with a total intensity of 60 mW/cm^2. Disilane (Si_2H_6) was used as the source gas. Dislane absorbs UV light at wavelengths shorter than 200 nm and directly dissociates photochemically to generate radicals according to the following equation (see Fig. 2)[19),20)].

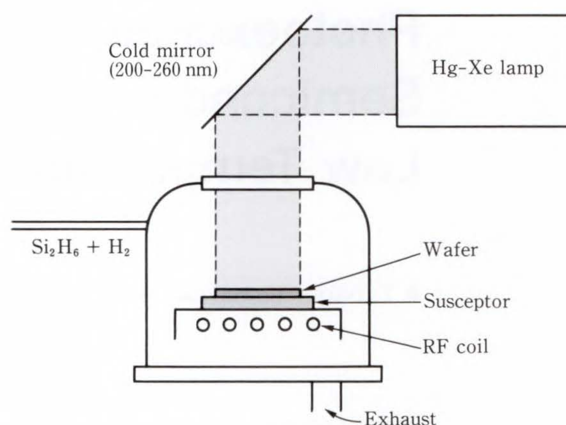

Fig. 1—Experimental set up of atmospheric pressure photoepitaxy.

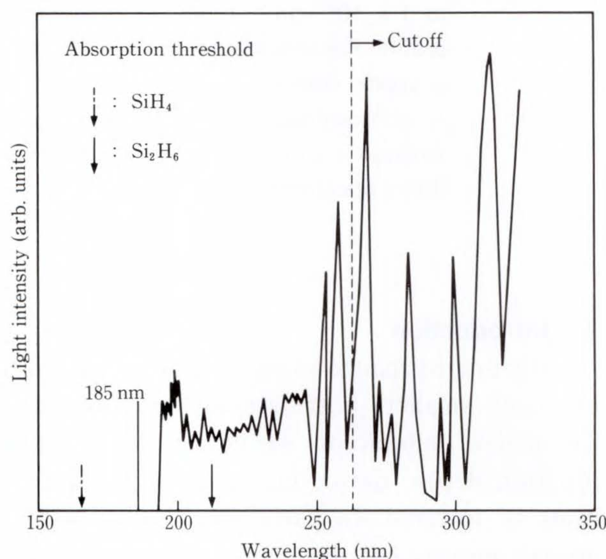

Fig. 2—UV spectrum from a short arc mercury lamp. The absorption threshold of silane and disilane are indicated using arrows.

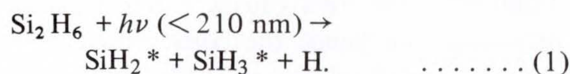

$$Si_2H_6 + h\nu\ (<210\ \text{nm}) \rightarrow SiH_2{}^* + SiH_3{}^* + H. \quad \ldots\ldots.(1)$$

Photodissociated molecules and atoms are supplied to the silicon substrate, which increases the growth rate and improves crystal quality. Conventional source gases such as silane (SiH_4) and diclorosilane (SiH_2Cl_2) do not absorb UV light, and so do not dissociate.

A four-inch Si(100)-oriented wafer was used as the substrate. After wet RCA treatment, the substrate was loaded into a vertical epitaxial reaction chamber equipped with an RF heater and SiC coated carbon susceptor. Before Si dep-

Fig. 3–RHEED pattern from a photoepitaxially grown layer at 630 °C. The photoepitaxial layer thickness is 200 nm.

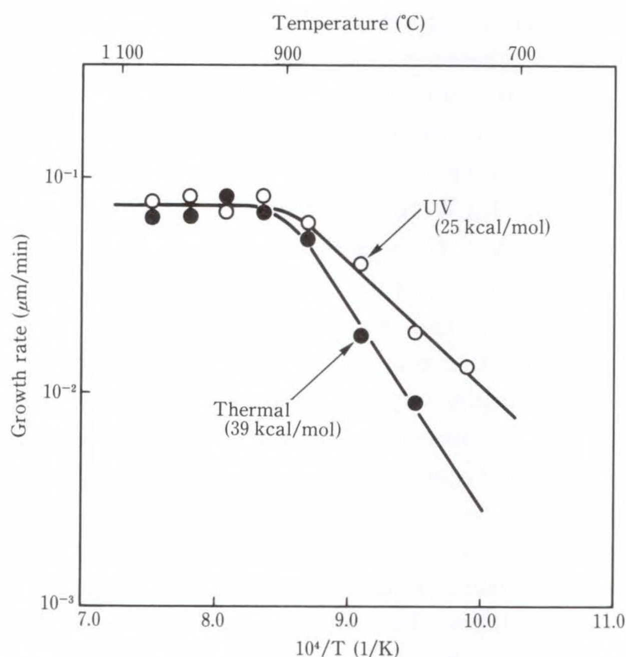

Fig. 4–Growth temperature dependence of growth rate. The UV irradiation reduced the activation energy from 39 kcal/mol to 25 kcal/mol below 900 °C.

osition, the substrate was heated 1 050 °C for 10 min in hydrogen without UV irradiation to remove any resident oxide. After this precleaning, the substrate was then cooled down to the deposition temperature and irradiated by UV light. This did not cause the substrate surface temperature to increase significantly since the infrared wavelength had already been attenuated. The substrate temperature was measured with an optical pyrometer precalibrated for the

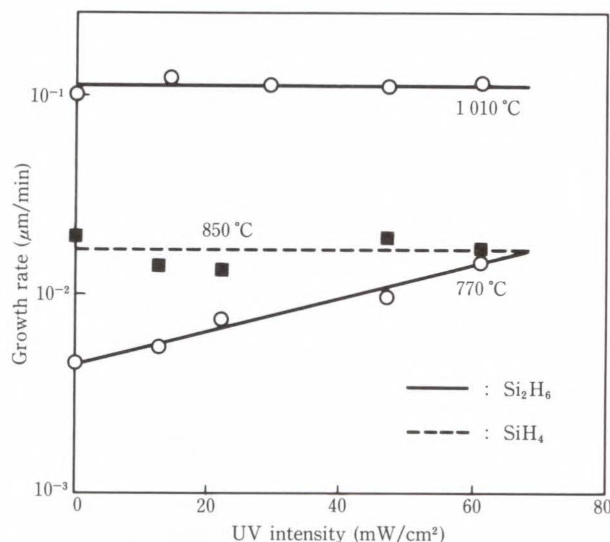

Fig. 5–UV intensity dependence of growth rate. For the growth rate using silane, UV irradiation was not effective.

emissivity of silicon. During Si deposition, hydrogen flow rate was set at 20 l/min and dislane flow rate at 1.5 cc/min.

We investigated the crystal quality of the photoepitaxial layer grown at 630 °C using Reflection High-Energy Electron Diffraction (RHEED). Figure 3 clearly shows a streaked pattern and a fine Kikuchi line, which shows the crystal quality is good. In contrast, without UV irradiation, polycrystalline was deposited at 630 °C. The temperature dependence of the Si growth rate under UV irradiation was investigated (see Fig. 4). As a comparison, the epitaxial growth rate using SiH_4 as the source gas is shown, since its growth is not influenced by light irradiation, SiH_4 gas does not absorb radiation of this wavelength.

For temperatures higher than 900 °C, Si_2H_6 gas dissociated thermally and gas-phase diffusion of the reactive species, which has a small temperature dependence, limited the growth rate. At temperatures lower than 900 °C, surface reactions determined the growth rate. Evidently, UV irradiation greatly reduces the activation energy for the Si_2H_6 source gas. We studied how the UV intensity affected the growth rate (see Fig. 5), and found that while the rate is constant for a substrate temperature of 1 010 °C, the growth rate increases at 770 °C

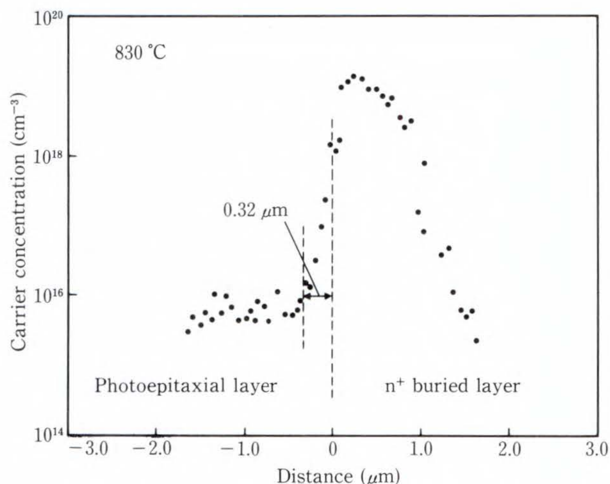

Fig. 6—Impurity profile in photoepitaxial layer grown at 830 °C on n+ buried layer. The traditional region was 0.32 μm.

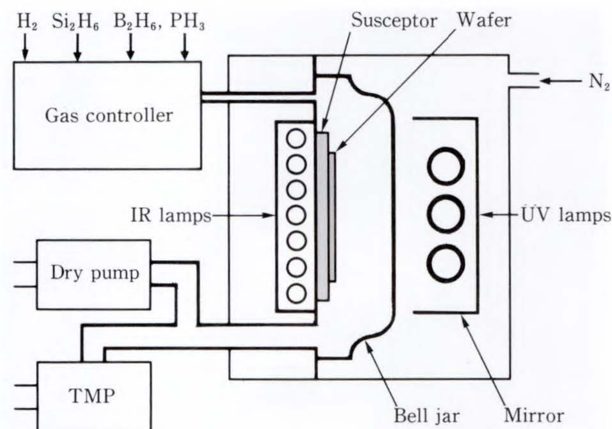

Fig. 7—Experimental set up of reduced pressure photoepitaxy.

and 830 °C as the light intensity increases; UV irradiation has a greater effect at lower substrate temperatures.

A photoepitaxial layer 1.8 μm thick was grown on the n^+ buried layer formed by arsenic-ion implantation. We employed a growth temperature of 830 °C to grow a relatively thick epitaxial layer (see Fig. 6). The transition distance from the substrate interface into the epitaxial layer where carrier concentration was 10^{16} cm^{-3}, was only 0.32 μm. Due to the low temperatures, the autodoping of arsenic was slight.

We have thus developed a low-temperature photoepitaxy process in a hydrogen atmospheric pressure using Si_2H_6 as the source gas. The Si_2H_6 source directly dissociates under UV irradiation thereby increasing the growth rate. The epitaxial growth temperature can be as low as 630 °C and still produce an almost abrupt impurity profile.

3. Photoepitaxy at reduced pressure

At atmospheric pressure and temperatures below 700 °C, single crystals could not be grown fast so it was impractical to make thick epitaxial layers this way. To improve the growth rate of high-quality crystal below 700 °C, we investigated photoepitaxy at reduced pressures[21].

We designed a special epitaxial chamber (see Fig. 7). The Si wafer was mounted on an SiC-coated carbon susceptor in a synthesized quartz chamber and infrared halogen lamps heated the susceptor from behind. The wafer surface was irradiated by UV light from high-pressure long-arc mercury lamps with an intensity of 1.2 W/cm^2 (integrated value of wavelengths less than 300 nm). These caused the surface temperature, measured by a thermocouple, to rise about 30 °C at 600 °C. The base pressure was 1×10^{-4} Pa using an oil-free dry pumping system and a turbo-molecular pump. To prevent absorption of the UV irradiation by oxygen, the area surrounding the quartz chamber was filled with nitrogen. The same wafer and wet cleaning prior to loading specifications were used as for atmospheric-pressure photoepitaxy. To remove any native oxide, the wafer was heated to 900 °C in hydrogen at 67 kPa for 10 min in the quartz chamber, then the temperature was lowered to the depositon temperature.

The same disilane temperature hydrogen gas system was used for Si film deposition as for atmospheric-pressure photoepitaxy. We investigated the growth rate at temperatures below 800 °C. From 650 °C to 800 °C, the rate decreased linearly as the inverse of temperature, either with or without UV irradiation (see Fig. 8). The growth rate with UV irradiation was about five times that without UV irradiation, which also reduced the activation energy. Below 650 °C, no film could be deposited without UV

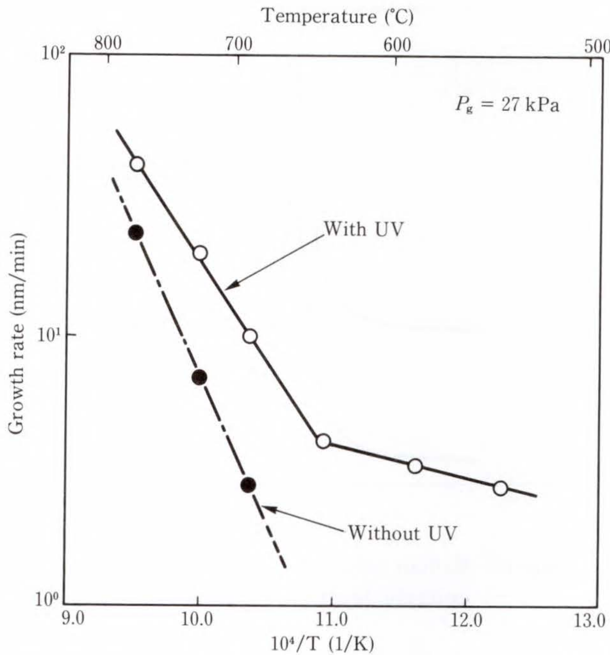

Fig. 8—Temperature dependence of growth rate. The total pressure was constant at 27 kPa.

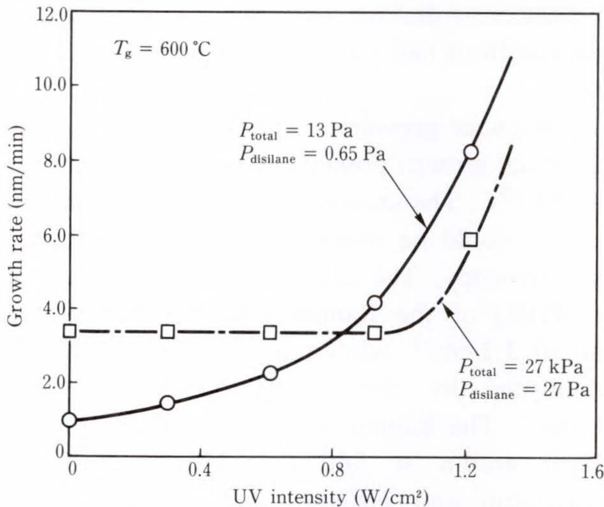

Fig. 9—UV intensity dependence of growth rate. The growth temperature was constant at 600 °C.

irradiation, and yet in the presence of UV irradiation, a single Si crystal could be grown independently of temperature. We studied the dependence of growth rate on UV intensity at total pressures of 27 kPa and 13 Pa, and at a temperature of 600 °C (see Fig. 9). At 13 Pa, growth rate increased with UV intensity whereas at 27 kPa, the growth rate was almost constant for weak UV intensities and increased for strong UV intensities. At weak UV intensities (in the thermal growth region), the growth rate was faster at high total pressure and high disilane partial pressure than for low total pressure and low disilane partial pressure. Conversely, at strong UV intensities, the growth rate of 13-Pa epitaxy almost exceeded that of 27-kPa epitaxy despite the low disilane partial pressure.

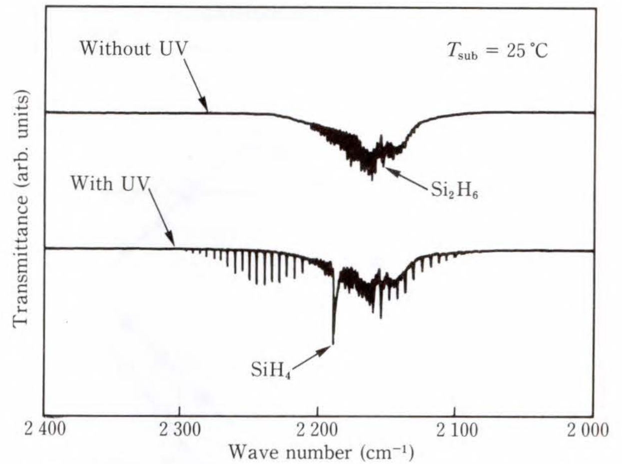

Fig. 10—FT-IR spectra of the vapor phase in the growth chamber with or without UV irradiation.

To investigate the dependence of growth rate on temperature and UV intensity, we analyzed *in-situ* the vapor phase photochemical reaction using Fourier-Transform Infrared Spectroscopy (FT-IR). The post-reaction gas was brought from the photoepitaxial gas system into an FT-IR analysis cell through a quartz capillary positioned 1 mm above the wafer surface. The pressure of the analysis cell was kept constant at 1.3 kPa. The IR absorption spectra was observed for both irradiated and nonirradiated reaction gas at room temperatures (see Fig. 10). Without UV irradiation, the absorption spectra at wavenumber of 2 215 cm^{-1} and around 930 cm^{-1} were missing due to silane stretching and the SiH_3 deformation modes could not be observed. However, after UV irradiation, these absorption spectra could be seen clearly. Thus, in this experimental system, silylene species were generated photochemically from disilane according to Equation (1). The reaction products, singlet silylene species SiH_2 and SiH_3 were absorbed by the Si surface and then by dehydrogenation the solid Si film was deposited.

We studied the temperature dependence of

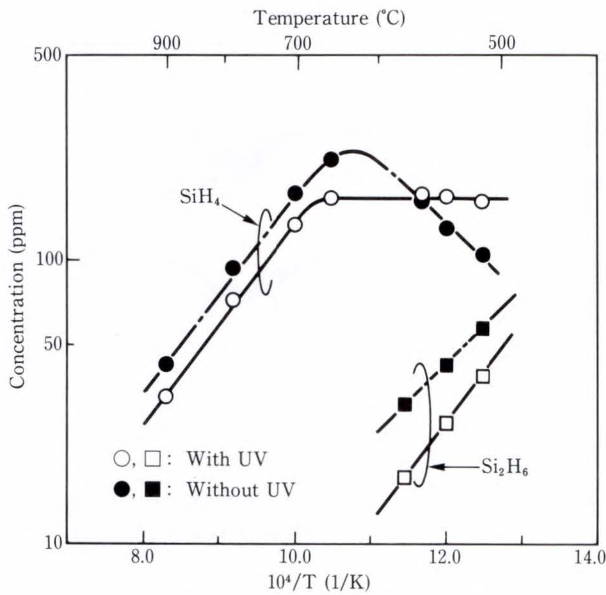

Fig. 11—Disilane and silane concentration in the vapor phase in the growth chamber. The concentrations were calculated from FT-IR data.

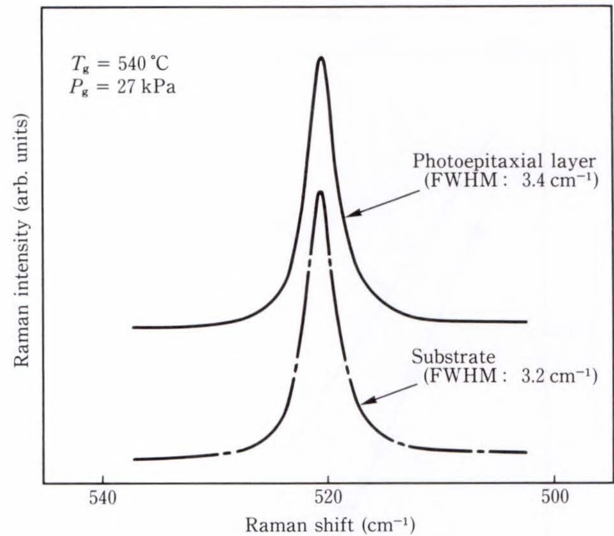

Fig. 12—Raman spectra of Si substrate and photoepitaxial layer grown at 540 °C.

the concentration of disilane and silane, using FT-IR (see Fig. 11). Above 700 °C, most of the disilane dissociated thermally and disilane could not be recognized in the FT-IR spectra even after UV irradiation. The silane concentration decreased as the growth rate increased, since the Si deposition used up the silylenes as they were produced. Below 650 °C and without UV irradiation, the concentration of silylene species decreased as the temperature dropped. However, after UV irradiation, the concentration almost became constant due to the photochemical dissociation of disilane. The temperature dependence of the concentration of the silylene species matched that of the growth rate, as shown in Fig. 8. We conclude that the growth rate is determined by the concentration of the silylene species, which are generated by thermal reactions in high temperature regions and photochemical reactions in low temperature regions.

We also studied the dependence of this photochemical reaction of disilane in the vapor phase on UV intensity. At high total and disilane partial pressures and low UV intensity, the effective wavelength of the photochemical reaction of disilane apparently no longer reached the crystal surface because the disilane was absorbed near the window through which the light came. In this case, the silylene species were mostly generated thermally. When the total and partial pressures of disilane were low, the photochemical reactions had a greater effect on the growth rate.

Reduced-pressure photoepitaxy made epitaxial growth possible at temperatures as low as 540 °C. The crystal quality of the layer thus grown could be observed by Raman scattering spectroscopy. The full width at half maximum (FWHM) of the Raman peak for bulk Si was about 3.2 cm^{-1}, while that for polycrystalline Si deposited by conventional LPCVD is about 8 cm^{-1}. The Raman spectra for a photoepitaxial layer grown at 540 °C exhibited the same waveform and FWHM value as bulk Si (see Fig. 12). This shows that the crystal quality of a photoepitaxial layer grown at 540 °C is high. Using high resolution TEM (HR-TEM), it was possible to study crystal defects and the interface structure between the photoepitaxial layer and substrate (see Fig. 13). No defects could be seen in the photoepitaxial layer of single crystals grown at 540 °C and there was no discontinuity at the interface.

UV irradiation effectively enhanced the vapor-phase reaction at reduced pressure compared with atmospheric pressure, and therefore the growth rate below 700 °C dramatically

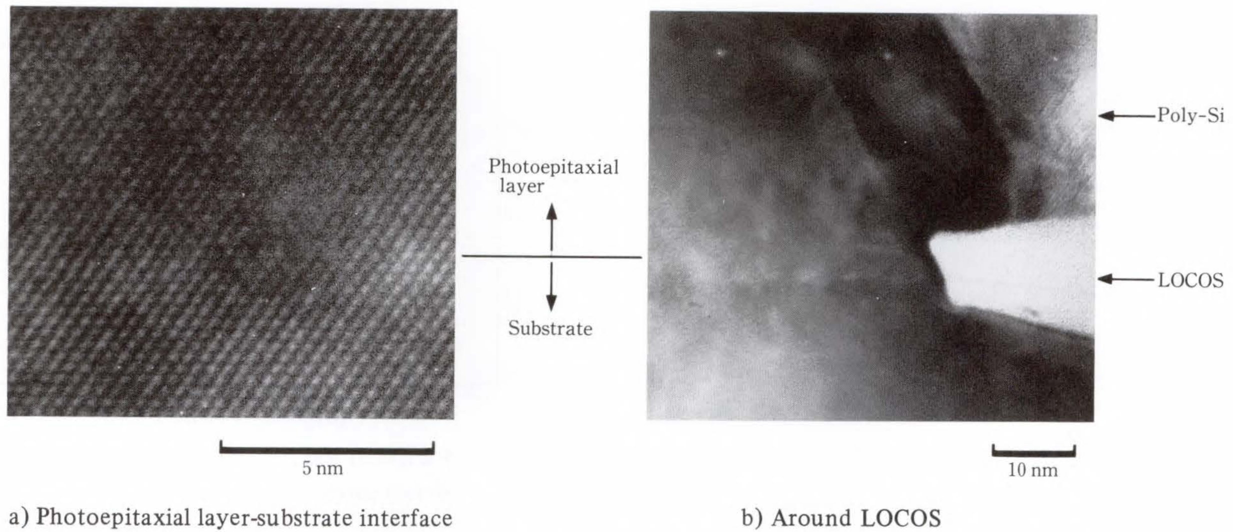

a) Photoepitaxial layer-substrate interface b) Around LOCOS

Fig. 13—High resolution TEM photograph of potoepitaxial layer grown at 540 °C. The photo-epitaxial layer was grown on a LOCOS structure, and poly-Si grown on the field oxide.

increased. Furthermore, the lowest epitaxial growth temperature was reduced from 630 °C to 540 °C.

4. Impurity doping

Impurity doping during epitaxial growth is an important technique for device fabrication. We investigated heavy boron doping during reduced pressure photoepitaxy[22], and used diborane (B_2H_6) as the *in-situ* doping source. The UV absorption threshold of diborane is about 190 nm, so it absorbs only a small percentage of the UV radiation used in this experiment. At this threshold wavelength, the absorption cross section of diborane is two orders of magnitude lower than disilane; diborane cannot therefore be directly dissociated photochemically[23)-26)].

For low diborane flow rates corresponding to doping carrier concentrations below 1×10^{19} cm^{-3}, carrier concentration increased linearly regardless of UV irradiation (see Fig. 14). The presence of UV irradiation slightly reduced doped carrier concentrations. The concentration of silylene species in the vapor phase at 600 °C was smaller without UV irradiation because disilane dissociated photochemically. The ratio of the contribution of boron species to doping and disilane species to film deposition became large without UV irradiation. Therefore, for low diborane flow rates, the

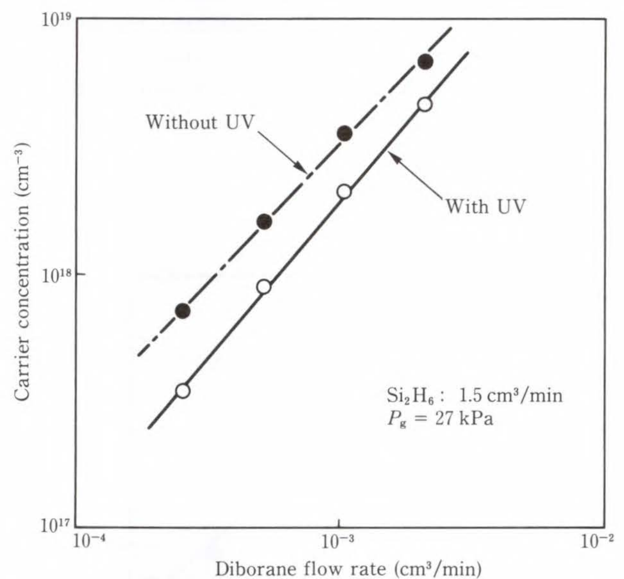

Fig. 14—Boron doping characteristics in low concentration range with or without UV irradiation.

doped carrier concentration became slightly smaller with UV irradiation. For high diborane flow rates with UV irradiation, the doped carrier concentration was almost constant at 1.5×10^{20} cm^{-1} (see Fig. 15). This exceeds the solid solubility limits for boron in Si at the deposition temperature of 600 °C. However, at these concentrations, thermal epitaxial growth was not possible and the boron atom activation deteriorated.

The boron atom activation ratio is related to the carrier concentration. The boron atom con-

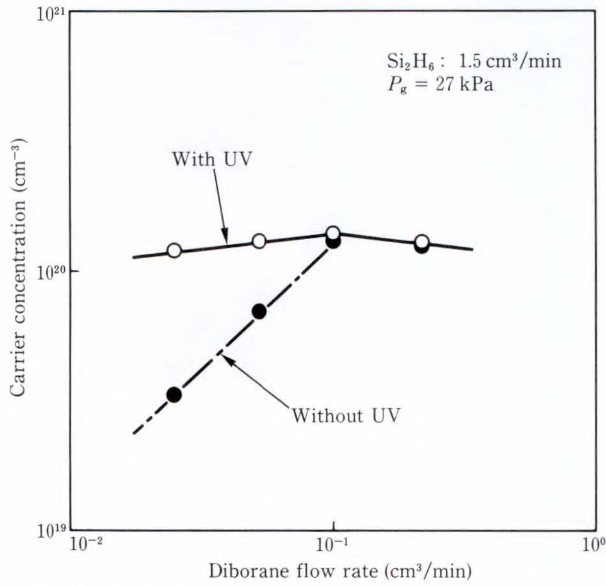

Fig. 15—Doping characteristics in high diborane flow rate region. With UV irradiation, the deposited film was a single crystal. Without UV irradiation, poly-Si or boron-silicon compounds were deposited.

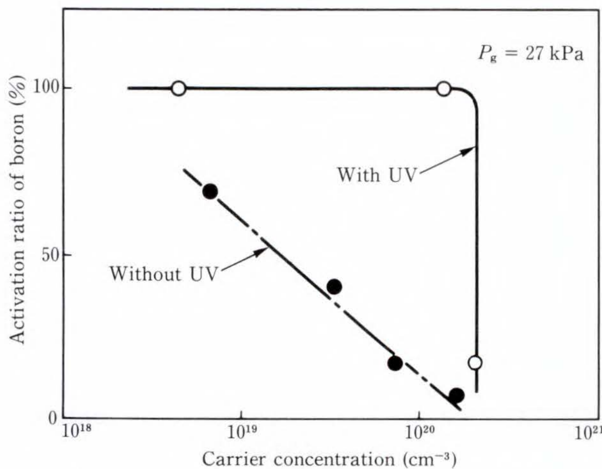

Fig. 16—Activation ratio of doped boron atoms vs. carrier concentration. The activation ratio was the same as the ratio of the carrier concentration to the concentration of doped boron atoms.

centration in deposited films can be determined using Hall measurement and SIMS analysis (see Fig. 16). Above a carrier concentration of 1×10^{18} cm^{-1}, the activation ratio without UV irradiation deteriorated, finally dropping to only a few percent. After UV irradiation, however, doped boron atoms were fully activated up to a concentration of 1.5×10^{20} cm^{-1}, then the ratio

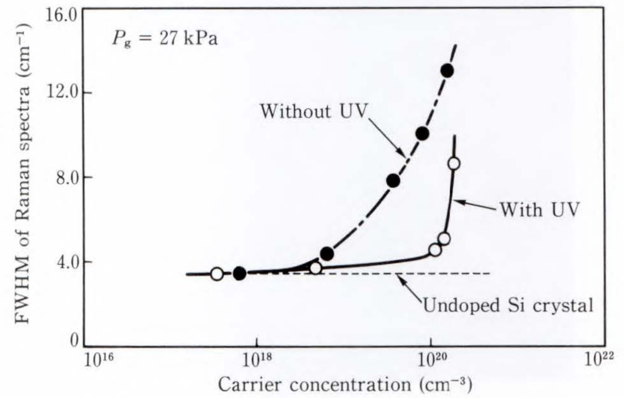

Fig. 17—FWHM of Raman scattering spectroscopy vs. doped carrier concentration.

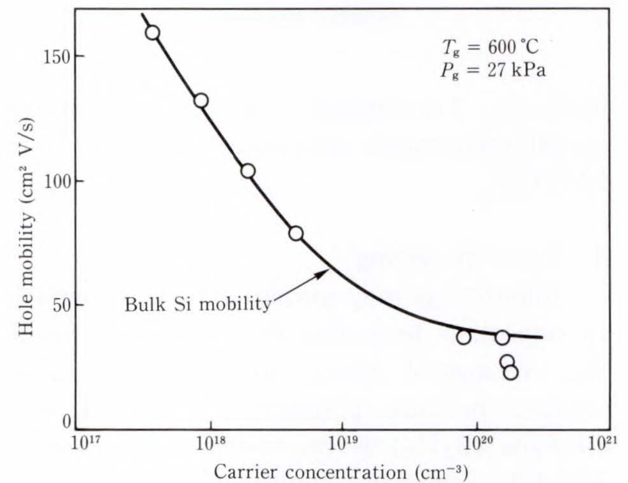

Fig. 18—Hole mobility vs. carrier concentration. Experimental data was plotted. The Irvin curve was estimated as a plane line.

dropped sharply to a few percent when the doped boron atom concentration exceeded this value.

This phenomenon was strongly related to crystal quality. Using Raman scattering, the crystal quality of the heavily boron doped photoepitaxial layer was observed, testing the FWHM's dependence on the doped carrier concentration at 600 °C (see Fig. 17). Without UV irradiation, the FWHM increased with carrier concentration showing that the crystal quality deteriorated. As the doped carrier concentration increased up to 1×10^{19} cm^{-3} poly-Si was produced, and finally boron-silicon compounds were deposited. But when UV irradiation was used, the FWHM remained almost constant at

3.5 cm^{-1}, as single crystals grew up to a carrier concentration of 1.5 x 10^{20} cm^{-3}. This dependence of crystal quality on the doped carrier concentration agrees well with the boron activation ratio shown in Fig. 16. The Hall mobilities of photoepitaxial layers grown at 600 °C were determined by Hall measurement as a function of the doped carrier concentration (see Fig. 18). The results fit well with an Irvin curve throughout the doping range, which shows that a photoepitaxial layer grown at 600 °C with heavy boron doping has good crystallinity.

The dependence of carrier doping efficiency on diborane flow rate is shown in Fig. 19. The efficiency is defined as the ratio of the total number of carriers in the deposited film to the total diborane volume introduced in the vapor phase (total number of boron atoms) (see Fig. 19). Without UV irradiation, this efficiency became saturated at a very low level, even lower than with UV irradiation. With UV irradiation, the efficiency increased sharply up to a flow rate of 2 x 10^{-2} cm^3/min, which corresponds to a 1.5 x 10^{20} cm^{-3} carrier concentration. Above this flow rate, the carrier doping efficiency decreased, eventually dropping to the same level as without UV irradiation. These results show that UV irradiation enhances carrier doping efficiency and suggest that an enhanced diborane vapor-phase reaction occurs, increasing the probability of boron species adsorption.

Diborane photolysis in the vapor phase was studied using FT-IR. The IR absorption spectra due to the B-H_3 bending mode was found to be a function of the disilane flow rate (see Fig. 20).

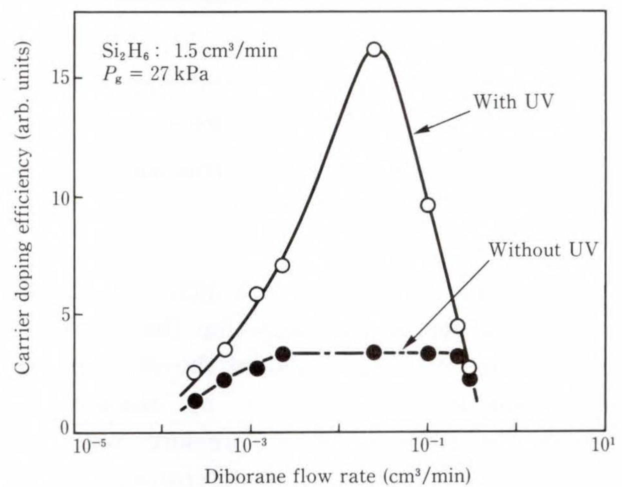

Fig. 19—Carrier doping efficiency vs. diborane flow rate.

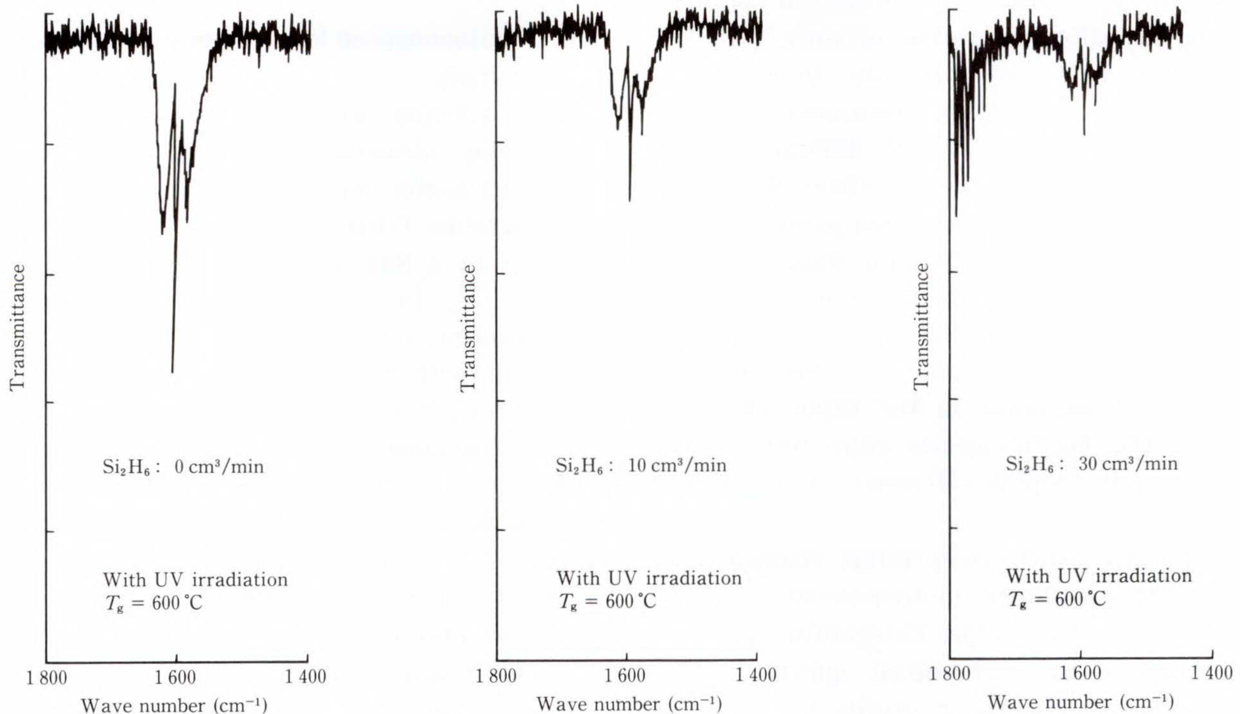

Fig. 20—IR absorption spectra due to the B-H_3 bending mode as a function of the flow rate of added disilane.

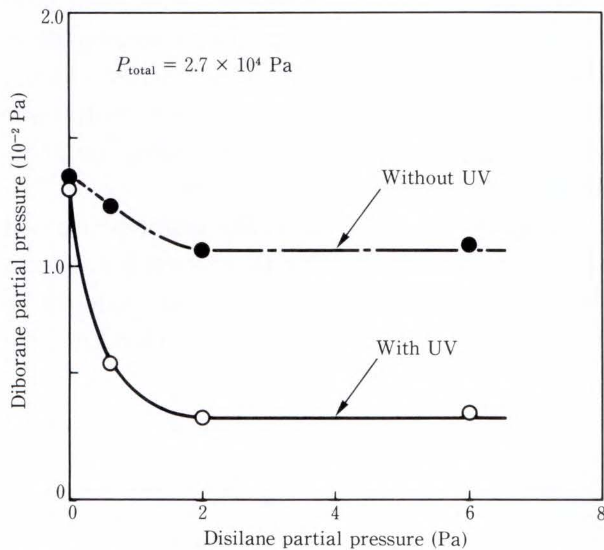

Fig. 21—Diborane partial pressure in the vapor phase vs. flow rate of added disilane.

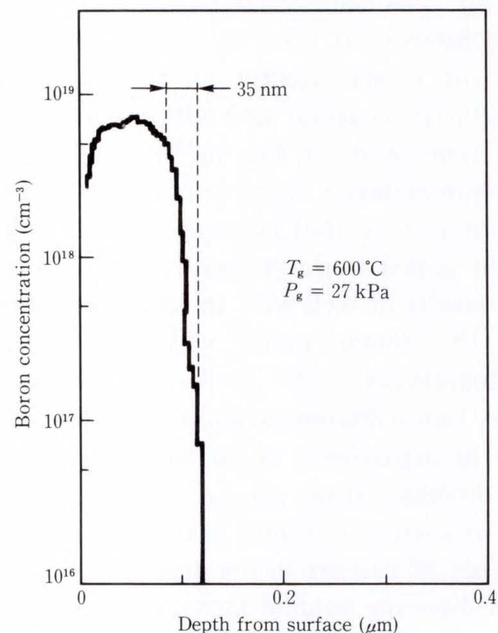

Fig. 22—Boron profile of photoepitaxial layer with heavy boron doping grown at 600 °C. The epitaxial layer was 100 nm thick and the transition width was 35 nm.

As the disilane flow rate was increased, the IR absorption decreased, suggesting that diborane photodissociation increased in the vapor phase, as shown in Fig. 21. When no disilane was added, the diborane partial pressures with and without UV irradiation, as determined by the IR absorption spectra, were identical, and thus the diborane did not dissociate photochemically. However, when disilane was present in the vapor phase, the diborane partial pressure with UV irradiation decreased markedly, showing that diborane photochemically dissociated, but without UV irradiation, very little diborane dissociated, even in the presence of disilane. We believe that diborane may be dissociated photochemically by disilane photosensitization. Photochemically dissociated silylene species eventually collide with diborane molecules, dissociating them through energy relaxation. Thus, photochemical diborane dissociation in the vapor phase increases the boron species concentration and increases the doping efficiency at heavy concentrations.

The low growth temperature enabled us to grow a heavily doped photoepitaxial layer with an abrupt boron profile. This profile could not be produced by conventional epitaxy and ion implantation. The boron profile for a heavily doped photoepitaxial layer with a carrier concentration of 8×10^{19} cm^{-3} grown at 600 °C was measured using SIMS (see Fig. 22). The transition width between the p^+ epitaxial layer and p^- substrate was about 35 nm.

5. Photoenhanced low-temperature selective epitaxy

Si selective epitaxy has a good potential for achieving advanced device structures. Conventional selective epitaxy is performed using high-temperature CVD, which uses SiH_2Cl_2 or HCl added to a SiH_4/H_2 gas system as the source gas[27)-30)]. For user gas added, the growth temperature must be above 900 °C for selective growth with good crystallinity. However, this high temperature makes it difficult to achieve abrupt impurity profiles due to impurity diffusion, and it also generates a large facet and stacking faults at the Si-SiO_2 sidewall interface. Thus, for a high selective growth rate below 700 °C, while still retaining good crystal quality we used photoenhanced CVD.

Low-temperature selective epitaxy needs a very low pressure, usually below 10 Pa. Therefore, selectivity and crystal growth can be

greatly degraded by moisture and oxygen contamination[31),32)]. For low-temperature selective epitaxy, an ultra clean deposition environment is necessary; we used a specially designed CVD system to suppress moisture and oxygen contamination. This system had a cold-walled quartz CVD chamber that was evacuated to a base pressure of 10^{-6} Pa at high temperatures using an oil-free pumping system, a turbomolecular pump, a loadlock chamber, and a transport chamber (see Fig. 23). The wafer was transported into the UHV without being exposed to air using magnetic-coupled linear transport devices. Using this UHV/CVD chamber, we tested the pressure dependence of selective growth over a wide range of pressures, from 10^{-4} Pa to 10^{4} Pa. To reduce contamination due to carbon and outgassing from the SiC coated carbon susceptor, we directly heated the Si substrate from the back using a newly developed Xe long-arc lamp without the SiC-coated carbon susceptor. Ths Si substrate absorbed the light from the Xe lamps very efficiently, causing the substrate temperature to rise rapidly. The wafer surface was vertically irradiated by UV light from high-pressure mercury lamps with a UV intensity of 1.2 W/cm^2 at

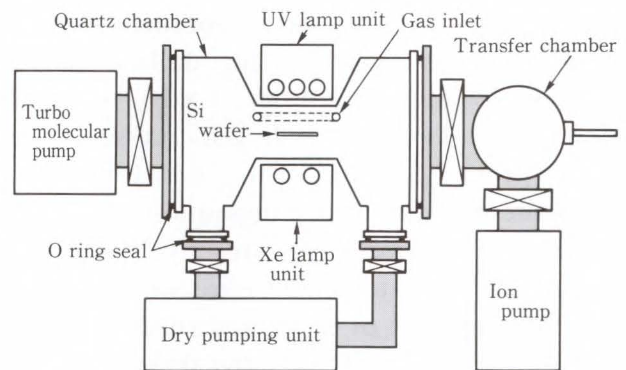

Fig. 23—Experimental set up of UHV-photoepitaxy.

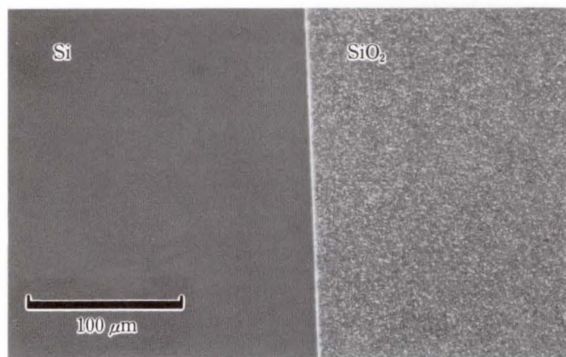

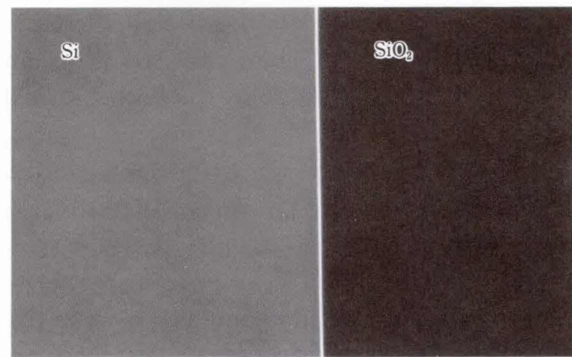

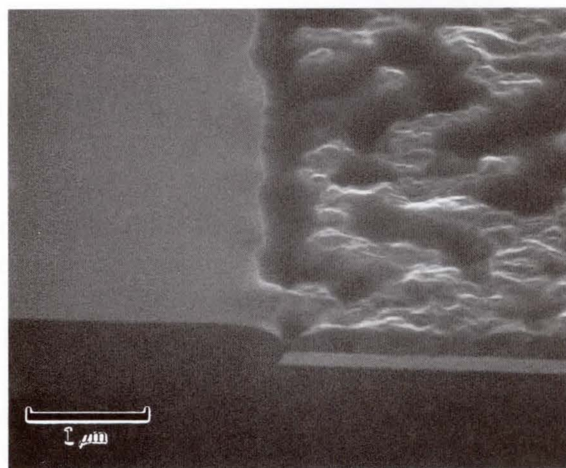

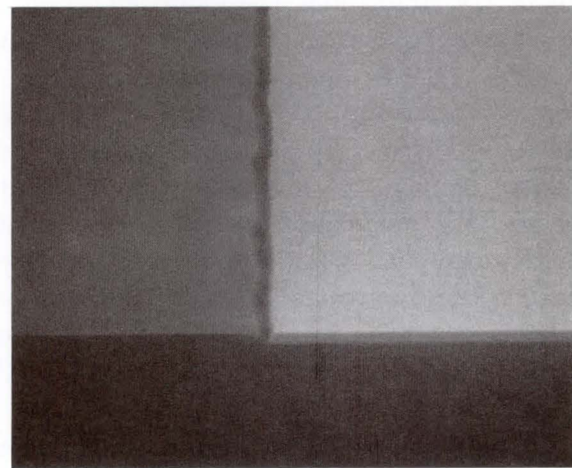

a) Thermal growth b) Photoepitaxy

Fig. 24—The surface morphgologies of deposited Si films at a substrate temperature of 750 °C. The top photographs were taken through a Nomarski microscope, and the bottom photographs were taken through an SEM.

the surface of the wafer. The substrate temperature was measured using a pyrometer which was calibrated by a thermocouple buried in the Si wafer, and the temperature rose 50 °C due to UV irradiation. To compensate for this increase, we decreased the Xe lamp output during UV irradiation. To remove the native oxide, the substrate was heated in hydrogen ambient at 800 °C and 67 Pa for 10 min without UV irradiation. Si films were deposited using a Si_2H_6/H_2 gas system. The disilane partial pressure was varied from 1×10^{-3} Pa to 1.7×10^{-2} Pa and hydrogen pressure was varied from 1.3×10^{-1} Pa to 2.6×10^{2} Pa. The total pressure during film deposition was almost equal to the hydrogen pressure.

At a substrate temperature of 750 °C, a hydrogen pressure of 67 Pa, and a disilane partial pressure of 3.6×10^{-3} Pa, the thermal growth (without UV irradiation) was nonselective {see Fig. 24a)}. In contrast, photoepitaxy clearly produced selective growth at 750 °C (substrate temperature: 700 °C + UV irradiation increase: 50 °C) {see Fig. 24b)}. The deposited films on Si showed mirror-like surfaces for both thermal and photoepitaxy growth as shown in Fig. 24. However, on SiO_2, the thermally grown polycrystalline film had a rough surface due to large grains resulting from the high deposition temperature.

We investigated the dependence of selectivity on deposition temperature both with and without UV irradiation. The hydrogen pressure was set at 67 Pa, the disilane partial pressure was set at 3.6×10^{-3} Pa, and the deposition temperature was varied from 610 °C to 890 °C. With UV irradiation, there was still selectivity until the substrate temperature dropped to 700 °C, but without UV irradiation, selective epitaxial growth required a temperature of 850 °C (see Fig. 25). The photoepitaxial growth rates on Si and SiO_2 depended very little on the substrate temperature throughout the range from 610 °C to 890 °C.

We also studied the dependence of Si film thickness on Si and SiO_2 on the deposition time. At a substrate surface temperatuere of 750 °C, a hydrogen pressure of 67 Pa, and a disilane partial pressure of 3.6×10^{-3} Pa, Si film could not be deposited on SiO_2 photoepitaxially, but could be deposited by thermal growth, and there was an incubation period for Si nucleation on SiO_2 (see Fig. 26)[33]. The growth rates on Si by photoepitaxy and by thermal growth were almost equal, because in this temperature range of 610 °C to 890 °C, disilane mainly dissociates thermally. However, at a substrate surface temperature of 600 °C, Si film was deposited on

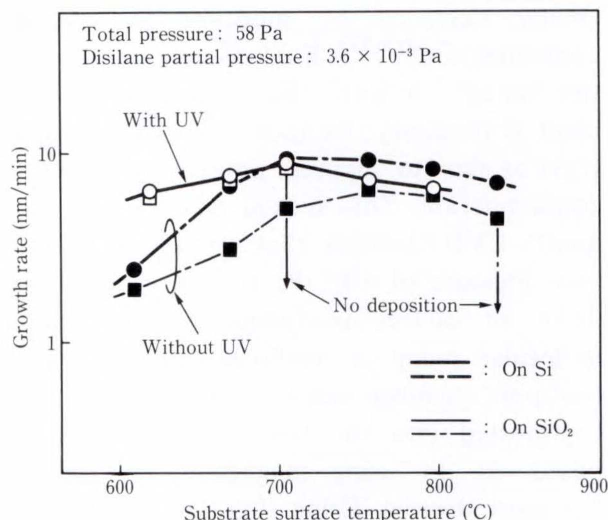

Fig. 25—Deposition temperature dependence of deposition rate on Si and SiO_2 with or without UV irradiation.

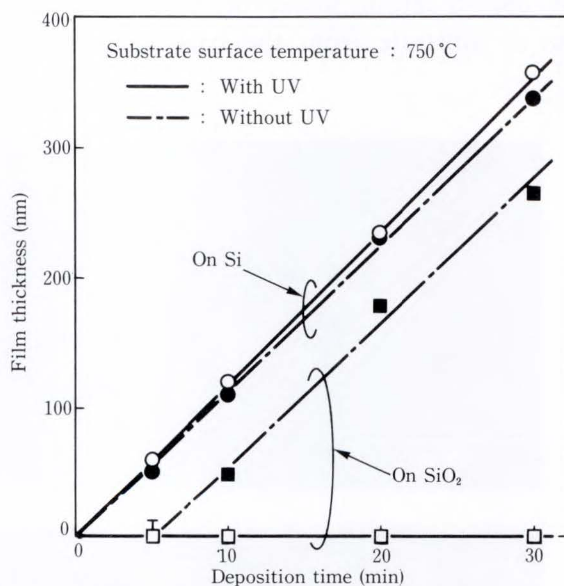

Fig. 26—Deposition time dependence of deposited Si film thickness at 750 °C.

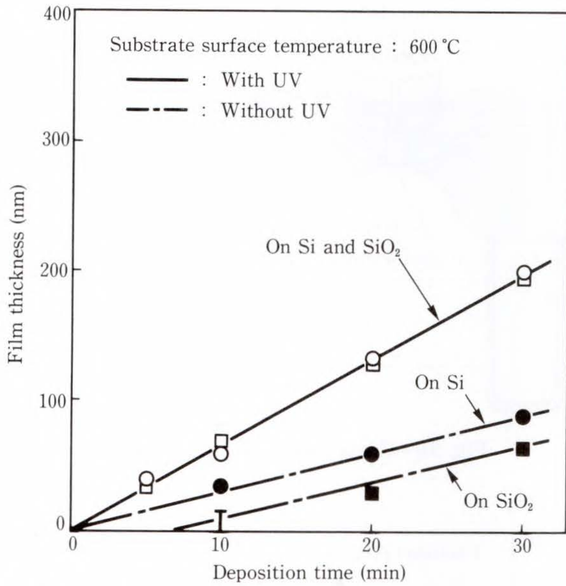

Fig. 27—Deposition time dependence of deposited Si film thickness at 600 °C.

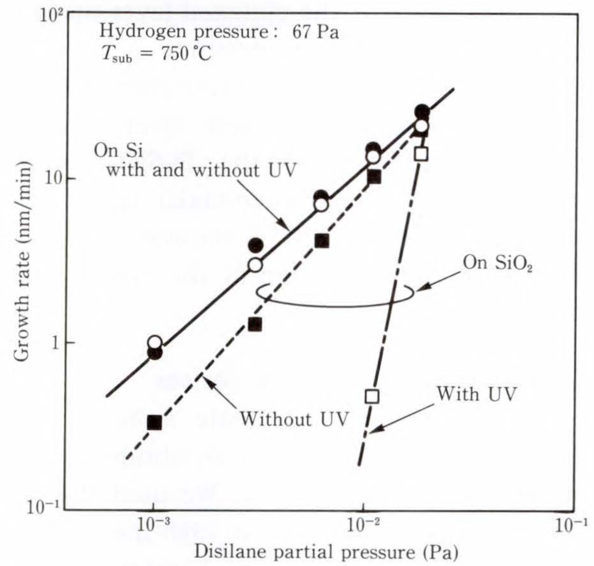

Fig. 28—Disilane partial pressure dependence of growth rate on Si and SiO_2 with or without UV irradiation.

Si and SiO_2 by both photoepitaxy and thermal growth (see Fig. 27). The thermal growth was much lower than the photoepitaxy rate for both Si and SiO_2 because at this temperature, disilane mainly dissociates photochemically. For thermal growth, there was an incubation period for Si nucleation on SiO_2, but this incubation period disappeared with UV irradiation.

From these results, we conclude that UV irradiation below 600 °C enhances disilane decomposition in the vapor phase, increasing the concentrations of the reactive species. For UV irradiation at 600 °C, the growth rate increases and the incubation period of Si nucleation on SiO_2 decreases. Above 600 °C, disilane mainly decomposed thermally. UV irradiation enhances the desorption of adsorbed silylene species on SiO_2, lowering the selective growth temperature.

Selectivity also depends on the growth rate, which in turn depends on the disilane partial pressure (see Fig. 28). At a substrate surface temperature of 750 °C and a hydrogen pressure of 67 Pa with UV irradiation, selective growth was achieved at a disilane partial pressures below 1×10^{-2} Pa. This corresponds to a growth rate of 15 nm/min. But under these conditions, thermal growth could not produce selective growth. The epitaxial layer grows on Si by photoepitaxy and by thermal growth at almost

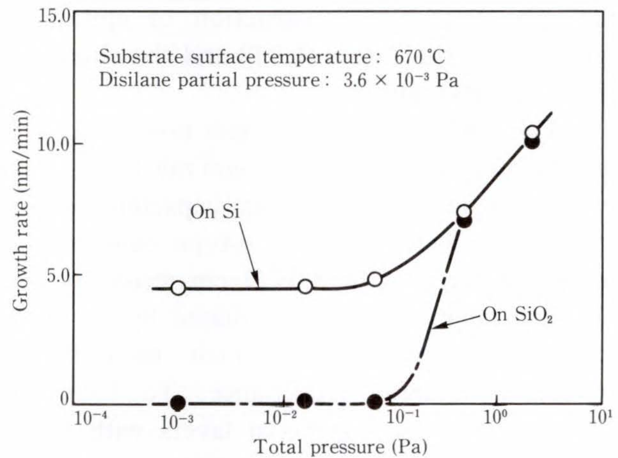

Fig. 29—Relationship of hydrogen pressure and selectivity. Substrate temperature was 670 °C.

the same rate because disilane mainly decomposes thermally.

Selectivity depends on yet another factor, hydrogen pressure, which is almost equal to the total deposition pressure (see Fig. 29). The substrate surface temperature was 670 °C and the disilane partial pressure was 3.6×10^{-3} Pa. At hydrogen pressures above 10 Pa, selective growth did not occur. The growth rate of the Si film on Si and SiO_2 increased as the hydrogen pressure increased, but at hydrogen pressures below 10 Pa, selective growth was observed;

the growth rate of the epitaxial layer on Si did not depend on hydrogen pressure.

The selective epitaxial layer grew thermally at 850 °C, and showed large facets and high density microfacets at the Si-SiO_2 sidewall interface. The selective epitaxial layer grown photoepitaxially at 720 °C showed small facets and microfacet formation at the Si-SiO_2 interface.

6. Application for bipolar devices

It was possible to create a heavy boron doped epitaxial layer with an abrupt impurity profile using photoepitaxy. We used this layer for the base region of a high-speed bipolar transistor[34),35)]. Scaling of bipolar transistors requires a very thin base with a high doping concentration to achieve high-speed operation while suppressing base punchthrough. Epitaxially grown bases are most suitable for this, and we describe here the construction of epitaxially grown base transistors (EBT) and the characteristics of EBTs and ICs.

The EBT was made using a non-selfaligned, double poly-Si process. A 0.5-μm rule lithography was used to reduce parasitic capacitances, and transistors were built on n-type conventional epitaxial layers with 0.09 $\Omega\cdot$cm resistivity and 1.0-μm thick. They were isolated by a poly-Si filled U-shaped groove which reduced the collector-substrate capacitance. To form the base region, photoepitaxial layers with boron concentrations of 3×10^{18} cm^{-3} were grown at 600 °C using photoenhanced low-temperature epitaxy. The emitter region was covered with an oxide/nitride/oxide pad and 250 nm poly-Si was deposited as the extrinsic base electrode. Boron ions were implanted into the poly-Si base electrode until its sheet resistance reached 100 $\Omega/\square$. From the mask size of 0.5 μm, the completed emitter was decreased to only 0.25-μm wide using the sidewall oxide and reactive ion etching (see Fig. 30). To form a very shallow emitter junction, we used rapid thermal annealing (RTA) to diffuse arsenic from the emitter poly-Si to the epitaxial base layer. By using the epitaxial base technique and RTA emitter driving, we were able to specify the intrinsic

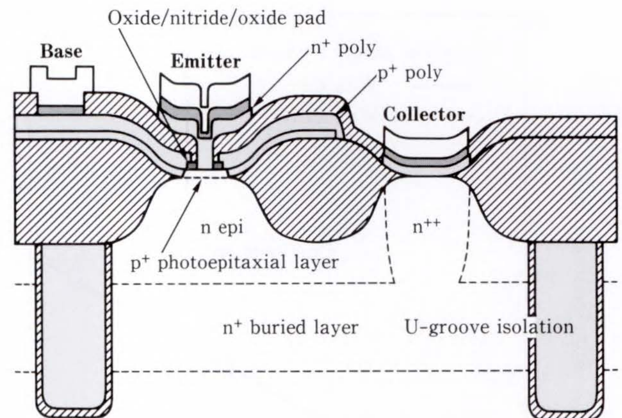

Fig. 30–Cross section diagram of EBT.

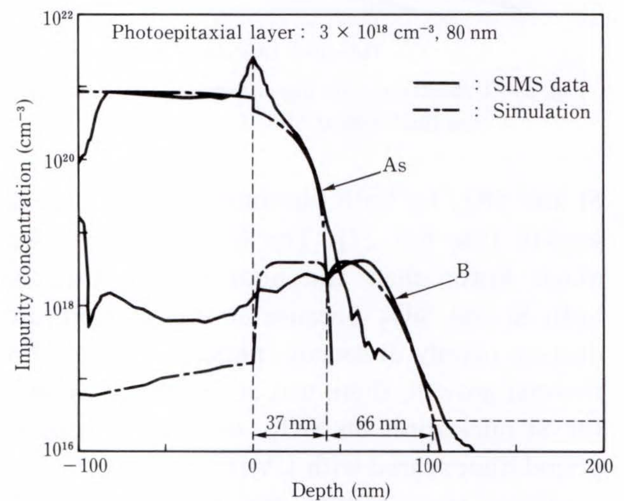

Fig. 31–Intrinsic transistor profile (SIMS and simulation) for 80 nm photoepitaxially grown base thickness.

base impurity profile with great flexibility and accuracy because the base width and base peak concentrations can be controlled independently. To produce both a low emitter resistance and shallow emitter junction depth, we used RTA at 1 100 °C for 2 s. The measurements of the impurity profiles of the EBT agreed well with results calculated using a modified SUPREM 3 simulation (see Fig. 31). These results clearly show that a shallow emitter junction just 35-nm deep was achieved. We could reduce the base width only by decreasing the deposited epitaxial base layer thickness, we succeeded in reducing the base width to 32 nm for a 45 nm epitaxial base layer thickness.

All the transistors we fabricated had base

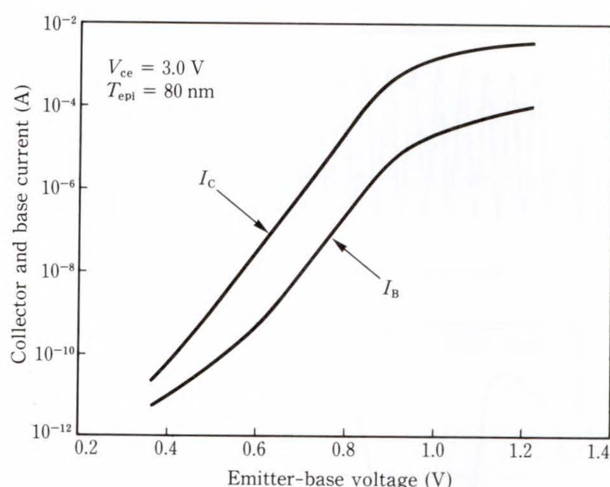

Fig. 32—Gummel plot of 80 nm photoepitaxially grown base thickness EBT.

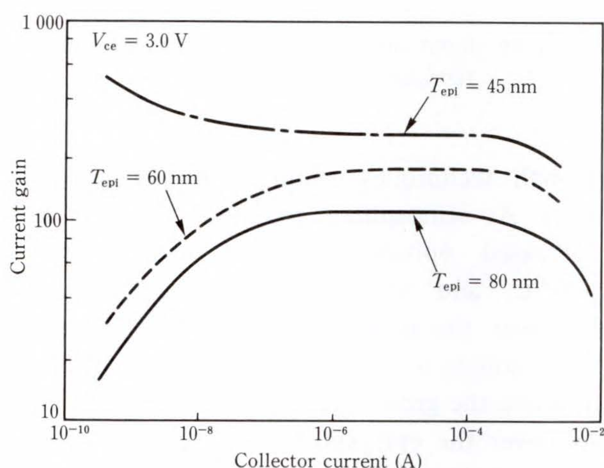

Fig. 33—Current gain vs. collector current characteristics.

widths of 31, 46, or 66 nm and all maintained BV_{ceo} above 3.0 volts, despite the thin base and high collector concentration of 1×10^{17} cm^{-3}. The base region was not susceptible to base punchthrough since the epitaxial base layer was doped to 3×10^{18} cm^{-3}. However, BV_{ebo} increased as the epitaxial base layer thickness decreased because the base peak concentration was reduced due to emitter driving. At the limit therefore, an EBT with 45 nm epitaxial layer thickness and 32 nm base width showed slight base punchthrough. The base current in a Gummel plot shows ideal characteristics through a current range over more than 4 decades (see Fig. 32). This proves that the photoepitaxially grown base layer has good crystallinity with

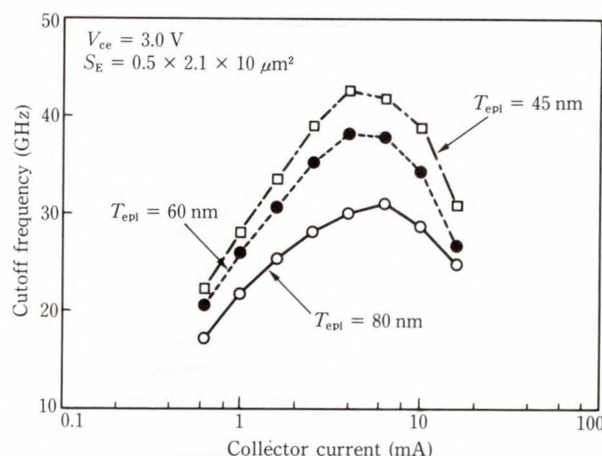

Fig. 34—Cutoff frequency as a function of collector current.

no defects to generate recombination centers. The current gain was 100 and 150 for base widths of 66 nm and 46 nm, respectively, and increased to 250 as the base width decreased to 31 nm. Current gain was independent of collector current over a wide range (see Fig. 33).

The frequency response of the EBT is primarily limited by the base transit time. The cutoff frequency improved from 32 GHz to 43 GHz as the base width was reduced from 66 nm to 32 nm (see Fig. 34). At higher frequencies, however, the base transit time no longer dominates. A 32 nm base is thin enough to make the base transit time relatively small compared with other components. To improve the frequency response further, the parasitical capacitances and resistances must be reduced and the collector impurity profile should be optimized.

Conventional ECL ring oscillators were built using the EBT. The minimum gate delay times for the 66 nm base width EBT was 67 ps for a low power gate (1.4 mW/gate) and 58 ps for a high power gate (7.5 mW/gate). However, the gate delay time deteriorated as the base width decreased (see Fig. 35). The cutoff frequency and the gate delay time appeared to have opposite effects depending on the base width, due to the base resistance. A 66 nm base EBT had an intrinsic base resistance (R_{bi}) of 26kΩ and an AC base resistance (r_{bb}) of 180 Ω. Both base resistances increased as the base width decreased.

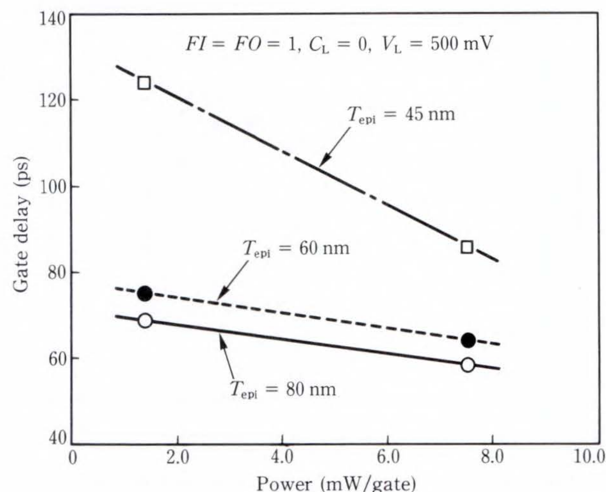

Fig. 35–Power-delay characteristics of ECL gates.

Table 1. Intrinsic base sheet resistance and AC base resistance of EBT

	Photoepitaxial layer thickness		
	45 nm	60 nm	80 nm
As grown sheet resistance (kΩ/□)	4.3	3.2	2.4
Intrinsic base resistance (kΩ/□)	–	48	26
AC base resistance (Ω)	350	240	180

The R_{bi} of the 32 nm base EBT became so large that measurement using pinch resistance patterns was impossible (see Table 1), and such a high base resistance limited the performance of the ECL. These high resistances were caused by a thin rink base (under the oxide/nitride/oxide pad) and relatively low boron doping concentrations of 3×10^{18} cm^{-3}. This resistance could be lowered further only by increasing the base boron doping concentration up to 6×10^{18} cm^{-3}. Simulation predicts that gate delay times below 30 ps are possible for a base boron doping concentration of 6×10^{18} cm^{-3}. We successfully integrated the EBT into a small-scale integrated circuit, and made a 1/8-divider using T-F/F circuits. We operated the circuit up to 11.7 GHz input frequency with a total power dissipation of 440 mW (see Fig. 36).

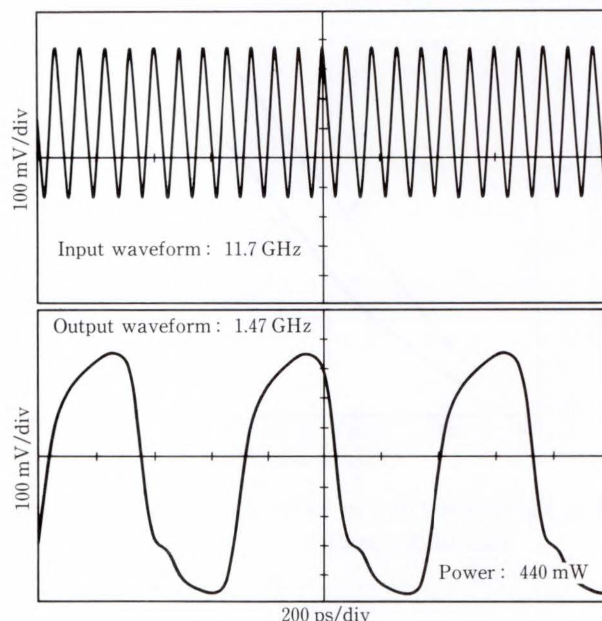

Fig. 36–Input and output waveform of 1/8-divider fabricated using EBT.

7. Conclusion

We have described low temperature epitaxial growth techniques using photoenhanced processes. At atmospheric pressure, UV irradiation decreased epitaxial growth temperature to 630 °C, and reduced the activation energy. However, the growth rate below 700 °C was not fast enough to grow thick epitaxial films. To improve the growth rate at low temperature and to lower the epitaxial growth temperature, we tried photoepitaxy at reduced pressure. The photochemical effect on the disilane vapor-phase reaction was greatly improved by reducing deposition pressure. Consequently, a reduction in epitaxial growth temperature of about 90 °C, was achieved, pushing the temperature down to 540 °C, and the growth rate below 700 °C was much higher for photoepitaxy at reduced pressure.

Photoepitaxy also enhanced boron doping at low growth temperatures. With UV irradiation at 600 °C, heavy boron doping of 1.5×10^{20} cm^{-3} produced superior crystal quality and very abrupt boron profiles. To control precisely the photoepitaxial surface reactions, we constructed a special photoepitaxial chamber evacuated to a UHV base pressure to suppress moisture and oxygen contamination. Using this chamber, we were able to achieve selective photoepitxy at

low temperatures with small facets and few defects at the $Si\text{-}SiO_2$ interface. We applied a heavily boron doped photoepitxial layer to the base region of a high-speed bipolar transistor, and produced a cutoff frequency of 43 GHz using a very thin base width of 31 nm. A frequency divider with an operating frequency of 11.8 GHz was made using a photoepitaxially grown base transistor. We have thus demonstrated the suitability of photoenhanced low-temperature epitaxy for LSI wafer processes of the future.

8. Acknowledgments

The authors would like to thank Drs. H. Ishikawa and T. Sugii for their helpful discussions and Messrs. H. Minakata, T. Aoyama, and N. Miyata for the results of their photoepitaxy experiments. We also thank Messrs. T. Fukano, T. Deguchi, A. Tahara, and I. Namura for device fabrication, Mr. Y. Kataoka for SIMS analysis, and Dr. S. Watanabe for FT-IR measurement.

References

1) Srinivasan, G.R., and Meyerson, B.S.: Current Status of Reduced Temperature Silicon Epitaxy by Chemical Vapor Deposition. *J. Electrochem. Soc.*, **134**, 6, pp. 1518-1524 (1987).
2) Atkinson, C. J., Wright, G. L., White, S. J., and Greenwood, J. D.: Submicron Silicon Epitaxial Films Deposited at Low Temperatures. *J. Electrochem. Soc.*, **132**, 4, pp. 936-938 (1985).
3) Cullen, G. W., and Carboy, J. F.: REDUCED PRESSURE SILICON EPITAXY; A REVIEW. *J. Cryst. Growth*, **70**, pp. 230-252 (1984).
4) Becker, G. E., and Bean, J. C.: Acceptor dopants in silicon molecular-beam epitaxy. *J. Appl. Phys.*, **48**, 8, pp. 3395-3399 (1977).
5) Shiraki, Y., Katayama, Y., Kobayashi, K. L. I., and Komatsubara, K. F.: MOLECULAR BEAM AND SOLID-PHASE EPITAXIES OF SILICON UNDER ULTRA-HIGH VACUUM. *J. Cryst. Growth*, **45**, pp. 287-291 (1978).
6) Ota Y.: Silicon molecular beam epitaxy with simultanous ion implant doping. *J. Appl. Phys.*, **51**, 2, pp. 1102-1110 (1980).
7) Meyerson, B.S.: Low-temperature silicon epitaxy by ultrahigh vacuum/chemical vapor deposition. *Appl. Phys. Lett.*, **48**, 12, pp. 797-799 (1986).
8) Meyerson, B. S., Ganin, E., Smith, D. A., and Nguen, T. N.: Low Temperature Silicon Epitaxy by Hot Wall Ultrahigh Vacuum/Low Pressure Chemical Vapor Deposition Techniques: Surface Optimization. *J. Electrochem. Soc.*, **133**, 6, pp. 1232-1235 (1986).
9) Nguen, T. N., Harame, D. L., Stork, J. M. C., Legoues, F. K., and Meyerson, B. S.: Characterization of IC Devices Fabricated in Low-Temperature (550 °C) Epitaxy by UHV/CVD Low-Temperature Epi. Tech. Dig. IEDM86, Washington D. C., 1986, pp. 304-307.
10) Donahue, T. J., and Reif, R.: Silicon epitaxy at 650-800 °C using low-pressure chemical vapor deposition both with and without plasma enhancement. *J. Appl. Phys.*, **57**, 8, pp. 2757-2765 (1985).
11) Donahue, T. J., and Reif, R.: Low Temperature Silicon Epitaxy Deposited by Very Low Pressure Chemical Vapor Deposition; I. Kinetics. *J. Electrochem. Soc.*, **133**, 8, pp. 1691-1697 (1986).
12) Breaux, L., Anthony, B., Hsu, T., Banerjee, S., and Tasch, A. : Homoepitaxial films grown on Si(100) at 150°C by remote plasma-enhanced chemical vapor deposition. *Appl. Phys. Lett.*, **55**, 18, pp. 1885-1887 (1989).
13) Suzuki, S., and Itoh, T.: Effect of Si-Ge buffer layer for low-temeprature Si epitaxial growth on Si substrate by rf plasma chemical vapor deposition. *J. Appl Phys.*, **54**, 3, pp. 1466-1470 (1983).
14) Frieser, R. G.: Low-Temperature Silicon Epitaxy. *J. Electrochem. Soc.*, **115**, 4, pp. 401-405 (1968).
15) Kumagawa, M., Sunami, H., Terasaki, T., and Nishizawa, J.: Epitaxial Growth with Light Irradiation. *Jpn. J. Appl. Phys.*, **7**, 11, pp. 1332-1341 (1968).
16) Ishitani, A., Ohshita, Y., Tanigaki, K., Takada, K., and Itoh, S.: Prebaking and silicon epitaxial growth enhanced by UV radiation. *J. Appl. Phys.*, **61**, 6, pp. 2224-2229 (1987).
17) Nishida, S., Shiimoto, T., Yamada, A., Karasawa, S., Konagai, M., and Takahashi, K.: Epitaxial growth of silicon by photochemical vapor deposition at a very low temperature of 200 °C. *Appl. Phys. Lett.*, **49**, 2, pp. 79-81 (1986).
18) Yamazaki, T., Ito, T., and Ishikawa, H.: Disilane Photoepitaxy for VLSI. Dig. Tech. Papers 1984 Sympo. VLSI Technol., San Diego, 1984, pp. 56-57.
19) Perkins, G. G. A., and Lampe, F. W.: The 147-nm Photolysis of Disilane. *J. Am. Chem. Soc.*, **102**, 11, pp. 3764-3769 (1980).
20) Itoh, U., Toyoshima, T., Onuki, H., Washida, N., and Ibuki, T.: Vacuum ultraviolet absorption cross

selections of SiH_4, GeH_4, Si_2H_6, and Si_3H_8. *J. Chem. Phys.*, **85**, 9, pp. 4867-4877 (1986).

21) Yamazaki, T., Sugino, R., Ito, T., and Ishikawa, H.: Photochemical Effects for Low-Temperature Si Epitaxy. Ext. Abs. 18th Conf. Solid-State Devices and Materials, Tokyo, Electrochem. Soc., Jpn., 1986, pp. 213-216.
22) Yamazaki, T., Watanabe, S., and Ito, T.: Heavy Boron Doping Low-Temperature Si Photoepitaxy. *J. Electrochem. Soc.*, **137**, 1, pp. 313-318 (1990).
23) Robin, M. B.: Higher Exited States of Polyatomic Molecules 1. 1st. ed., Academic Press, Inc., N. Y., 1974.
24) Biweekly List of Paper on Radiation Chemistry and Photochemistry. (Radiation Chemistry Data Center Radiation laboratory, University of Nortre Dame, Indiana).
25) Clark, J. H., and Anderson, R. G.: Silane purification via laser-induced chemistry. *Appl. Phys. Lett.*, **32**, 1, pp. 46-49 (1978).
26) Rai-Choudhury, P., and Salkovitz, E. I.: DOPING OF EPITAXIAL SILICON: EFFECT OF DOPANT PARTIAL PRESSURE. *J. Cryst. Growth*, **7**, 3, pp. 361-367 (1970).
27) Tanno, K., Endo, N., Kitajima, H., Kurogi, Y., and Tsuya, H.: Selective Silicon Epitaxy Using Reduced Pressure Technique. *Jpn. J. Appl Phys.* **21**, 9, pp. L564-L566 (1982).
28) Borland, J. O., and Drowley, C. I.: Advanced dielectric Isolation Through Selective Epitaxial Growth Techniques. *Solid State Technol.*, **28**, 8. pp. 141-148 (1985).
29) Pagliaro, Jr. R., Corboy, J, F., Jastrzebski, L., and Soydan, R.: Uniformly Thick Selective Epitaxial Silicon. *J. Electrochem. Soc.*, **134**, 5, pp. 1235-1238 (1987).
30) Ishitani, A., Kitajima, H., Endo, N., and Kasai, N.: Facet Formation in Selective Silicon Epitaxial Growth. *Jpn. J. Appl. Phys.*, **24**, 10, pp. 1267-1269 (1985).
31) Sedgwick, T. O., Berkenbit, M., and Kuan, T. S.: Low-temperature selective epitaxial growth of silicon at atmospheric pressure. *Appl. Phys. Lett.*, **54**, 26, pp. 2689-2691 (1989).
32) Murota, J., Nakayama. N., Kato, M., Mikoshiba, N., and Ohmi, T.: Low-temperature silicon selective deposition and epitaxy on silicon using the thermal decomposition of silane under ultraclean environment. *Appl. Phys. Lett.*, **54**, 11, pp. 1007-1009 (1989).
33) Classen, W. A. P., and Bloem, J.: The Nucleation of CVD Silicon on SiO_2 and Si_3N_4 Substrates III. The SiH_4-HC1-H_2 System at low Temperatures. *J. Electrochem. Soc.*, **128**, 6, pp. 1353-1359 (1981).
34) Sugii, T., Yamazaki, T., and Ito, T.: Si Hetero-Bipolar Transistor with a Fluorine-Doped SiC Emitter and a Thin, Highly Doped Epitaxial Base. *IEEE Trans. Electron Devices*, **ED-37**, 11, pp. 2331-2335 (1990).
35) Yamazaki, T., Namura, I., Goto, H., Tahara, A., and Ito, T.: A 11.7 GHz 1/8-Divider Using 43 GHz S; High Speed Bipolar Transistor with Photoepitaxial by Grown Ultra-Thin Base. Tech. Dig. Proc. IEDM90, San Francisco, 1990, pp. 309-312.

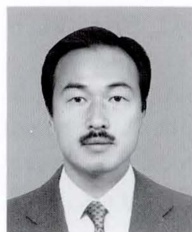

Tatsuya Yamazaki

Semiconductor Devices Laboratory
FUJITSU LABORATORIES, ATSUGI
Bachelor of Instrument and measurement Eng.
Keio University 1981
Master of Instrument and measurement Eng.
Keio University 1983
Specializing in Low Temperature Epitaxy and High Speed Bipolar Devices

Takashi Ito

Semiconductor Devices Laboratory
FUJITSU LABORATORIES, ATSUGI
Bachelor of Electronic Eng.
Tokyo Institute of Technology 1969
Dr. of Electronic Eng.
Tokyo Institute of Technology 1974
Specializing in Semiconductor Devices and Processes

REVIEW

UDC 621.3.049.771.14.002.2

Photoexcited Processes for Semiconductors II: Dry Cleaning and Dry Etching

• Yasuhisa Sato • Rinshi Sugino • Takashi Ito

(Manuscript received July 8, 1991)

A photoexcited dry cleaning process using highly purified chlorine gas was developed as an ultraclean process for silicon ultra-large scale integrated-circuit (ULSI) production. The process aids in deep-submicron device fabrication. Metallic contaminants remaining on a wafer's surface after wet cleaning can be significantly reduced by photoexcited cleaning. Photoexcited cleaning can also remove contaminants that have penetrated the silicon substrate during reactive-ion processing by etching the contaminated layer without damaging the uncontaminated layer. Thus, dry cleaning improves thin gate oxide integrity, SiO_2-Si interface quality, carrier lifetime, junction leakage characteristics, and epitaxial film quality.

1. Introduction

Contaminants such as alkali metals, heavy metals, and hydrocarbons introduced onto silicon surfaces during device manufacture can degrade both device performance and reliability[1),2)]. Although the use of highly pure wet chemicals, resists, and gases can alleviate the problem, processes causing surface, contamination and damage such as ion implantation, dry etching, and resist ashing are frequently used when manufacturing ULSI devices. Thus, cleaning the wafer surface has become an important part of ULSI processing. Wafers are cleaned prior to thermal oxidation, impurity diffusion, epitaxial growth of silicon films, chemical vapor deposition, and other thermal processes.

Currently, wet cleaning processes are primarily used; these are useful for removing large particles and other contaminants remaining on wafer surfaces after such processes as dry etching and ion implantation.

ULSI processing requires very clean wafer surfaces. For example, for a dynamic random access memory (DRAM), surface cleanliness determines the refresh time, which should increase as the degree of integration increases.

Photoexcited dry cleaning using reactive gases improves upon wet cleaning and other dry cleaning techniques such as reactive-plasma or reactive-ion cleaning, both of which can damage and contaminate a wafer's surface. Some of the advantages of photoexcited dry cleaning over conventional wet cleaning are as follows:

1) As devices become smaller, it becomes harder for wet chemicals to clean surface anomalies such as contact holes and deep trenches. Photoexcited radicals can clean these anomalies.
2) Gases can be cleared from a chamber faster and easier than wet chemicals. Less recontamination occurs on clean surfaces.
3) The process chambers are similar to those used in CVD or dry etching, making the equipment compatible with already-established automated ULSI production lines.
4) The exposure atmosphere is controlled, and film deposition can be conducted without exposing the wafer to air by connecting the process chambers to each other. Thus, high-quality gate oxide and epitaxial films

become easier to fabricate.

5) The amount of chemicals required is usually much smaller for gas cleaning, making the system and process more economical.
6) Dry cleaning, of course, does not require a drying process, which often causes such problems as watermarks.

Photoexicted dry cleaning using ozone is useful for removing organic particles. For inorganic materials such as metals, photoexcited halogen radicals are effective. Combining photo-excited and wet cleaning significantly improves cleanliness[3),4)].

This paper discusses the procedure and electrical properties of photoexcited dry cleaning using halogen, and discusses the advantages of this method over wet chemical cleaning for ULSI processing.

2. Cleaning mechanisms

The reaction mechanisms in photoexcited dry cleaning using halogen radicals are shown in Fig. 1. The halogen gas is dissociated to atomic radicals by ultraviolet irradiation. Chlorine gas was initially used as the reactive halogen gas because it is dissociated by the ultraviolet light of both high and low pressure mercury lamps.

Figure 2 shows the absorption spectrum of chlorine[5)] and the emission spectrum of a microwave-excited high-pressure mercury lamp. Any radiation having a wavelength between 250 nm and 400 nm contributes to the dissociation of chlorine molecules. The chlorine molecules dissociate into highly reactive atomic radicals which bond with the silicon and metal contaminants on the wafer surface.

The metal contaminants are removed from the surface as chlorides. There are two desorption mechanisms in photoexicted dry cleaning (see Fig. 1). The first mechanism is the evaporation of chloride compounds (MCl_x). In this mechanism, chlorine radicals react with contaminative metal atoms to provide volatile chlorine compounds. The second is the lift-off mechanism, in which electron-hole pairs are generated[6)] during irradiation by ultraviolet light. Chlorine radicals adsorbed on silicon surfaces receive electrons and change to negatively charged chlorine ions. The positively-charged silicon substrate attracts the chlorine ions producing silicon-chloride compounds, while the high vapor pressure causes spontaneous etching. Metal contaminants are lifted off at the same time as the silicon is etched. While the vapor pressure of such metallic chlorides of Ti, Al, and Fe is relatively high, the vapor pressure of K, Na, Mg, and Ni is low[7)]. The former can be removed by direct vaporization, while the latter must be removed by lift-off.

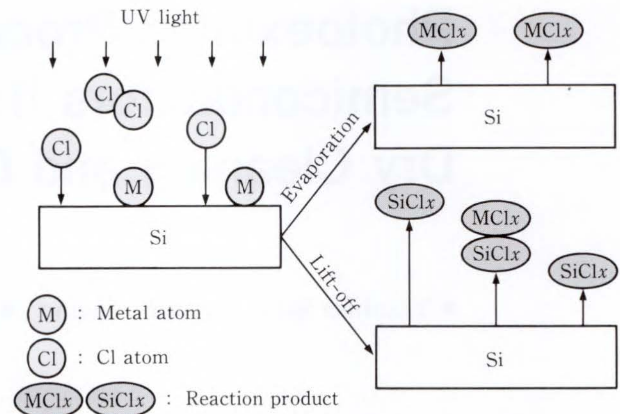

Fig. 1—The two desorption mechanisms in photoexcited dry cleaning: direct vaporization of chloride compounds, and lift-off.

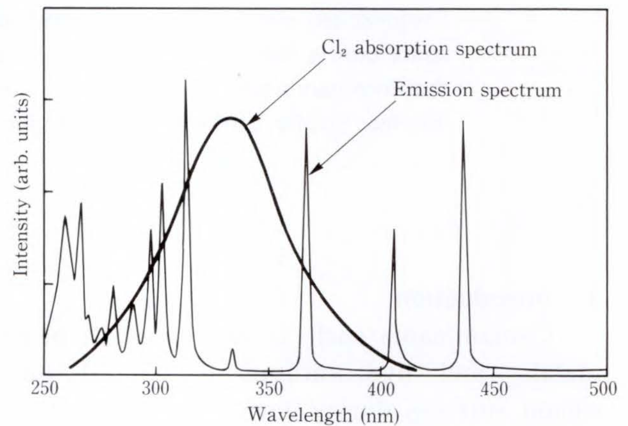

Fig. 2—Absorption spectrum of chlorine[5)] and emission spectrum of a microwave-excited high-pressure mercury lamp. Light between 250 nm and 400 nm contributes to the dissociation of chlorine molecules.

3. Cleaning procedure

The wafer is placed in a quartz chamber, and heated from the back by an infrared lamp in a

high-purity chlorine atmosphere. A microwave-excited mercury lamp irradiates the wafer from directly above. Figure 3 shows the dependence of the etch depth on the ulraviolet light irradiation time at a substrate temperature of 150°C[3]. The ultraviolet intensity was 22 mW/cm^2 over the wavelength range from 200 nm to 350 nm. The figure shows that etching occurs only when the wafer is irradiated[8].

However, native oxides are not removed by

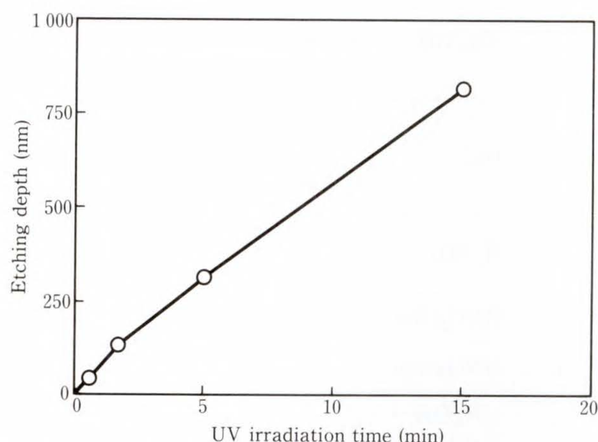

Fig.3–Dependence of etching depth on ultraviolet light irradiation time. Etching depth is proportional to irradiation time[3]. There is no delay at the beginning of etching.

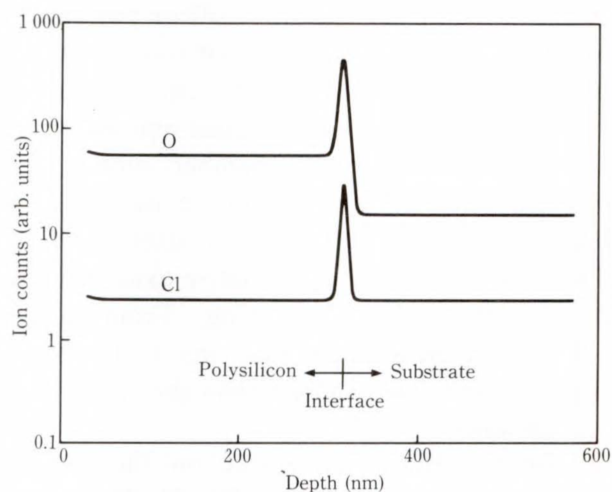

Fig. 4–Depth profiles of wafer after photoexcited dry cleaning and deposition of 300 nm polysilicon layer.

Treatment	HF	NH_4OH	HCL
Surface morphology 1 μm			

H_2SO_4	HNO_3hot	HNO_3boiL	$NH_4OH \rightarrow HNO_3$hot

Fig. 5–Surface morphology after various types of wet cleaning followed by photoexcited dry cleaning as observed by transmission electron microscope (TEM)[3].

photoexcited dry cleaning using chlorine. Figure 4 shows the secondary ion mass spectrometry (SIMS) depth profiles of oxygen and chlorine in cleaned samples onto which a polysilicon layer was deposited[9]. The figure shows that large numbers of oxygen and chlorine atoms accumulate at the silicon-polysilicon interface. The concentration of oxygen at the interface is estimated to be 10^{22} cm^{-3}. Since the partial pressures of both oxygen and water are less than 10^{-5} Pa in the chamber, such a high oxygen concentration cannot be caused by a mechanism such as oxidation after cleaning. Thus, we conclude that the native oxide remains during photoexcited cleaning. From Auger analysis, it was found that the hydrocarbon residue's signal was smaller than the signal after wet cleaning[3].

Despite the native oxide on the surface, etching is not delayed (see Fig. 3). The photoexcited chlorine radicals probably diffuse through the thin native oxide and react with silicon atoms to produce volatile species like $SiCl_2$ and $SiCl_4$. Most likely, the chlorine radicals react with contaminants in the native oxide and with contaminants near the silicon surface. Reaction products diffuse out through the native oxide and are discharged.

The process by which a silicon wafer is etched by photoexcited dry cleaning greatly depends on the surface conditions. Differences were observed between surfaces after various wet treatments followed by photoexicted dry cleaning that were not observed just after wet treatments. Figure 5 shows the surface morphology after seven types of wet treatment followed by photoexcited dry cleaning as observed by transmission electron microscope (TEM)[3]. The process parameters of the wet treatments are shown in Table 1. All wafers were treated with diluted HF and rinsed in deionized water before wet treatment, and were rinsed in deionized water after wet treatment. Treatments using NH_4OH, HCl, or H_2SO_4 produce very uniform silicon surfaces after photoexcited dry cleaning. This contrasts with the surface after HNO_3 treatment. While treatment with HNO_3 roughens the surface, the surfaces after

Table 1. Process parameters of wet cleaning shown in Fig. 6

No.	Test Solution	Composition	Temp. (°C)	Time (min)
1	HF	3 HF 100 H_2O	25	1
2	NH_4OH	1 NH_4OH 1.4 H_2O_2 4 H_2O	63-80	10
3	HCl	1 HCl 1 H_2O_2 4 H_2O	37-65	10
4	H_2SO_4	4 H_2SO_4 1 H_2O_2	90-85	10
5	HNO_3 hot	HNO_3	45-60	5
6	HNO_3 boil	HNO_3	115-125	5
7	$NH_4OH \rightarrow$ HNO_3 hot	No. 2 → No. 5		

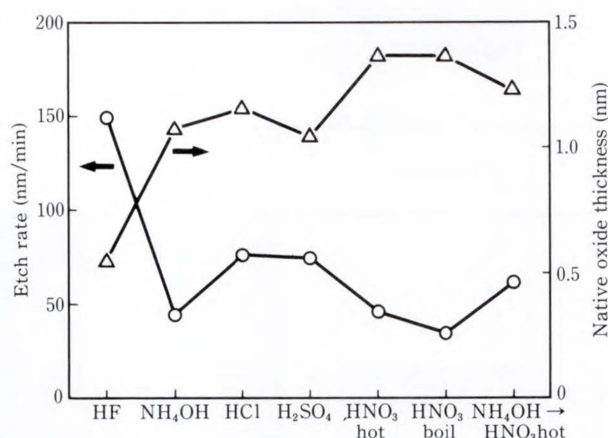

Fig. 6—Native oxide thicknesses and photoexcited etching rates of various types of wet cleaning[3].

treatment with NH_4OH and HNO_3 are smooth. Treatment using HF solution causes long periods of roughening.

Figure 6 shows the native oxide thicknesses and photoexcited etching rates of various types of wet cleaning. The thicknesses were measured using an ellipsometer[3]. The surface morphology after photoexcited dry cleaning reflects not only the thickness of the native oxides after wet cleaning but also the film quality. While the native oxide after HNO_3 cleaning is only slightly thicker than after NH_4OH, HCl, or H_2SO_4 cleaning, surfaces treated with HNO_3 differ

from surfaces treated with other solutions. After HNO_3 treatment, very thin native oxides disturb the chlorine radical's diffusion into the surface, causing etch pits to form on the wafer's surface.

The chemical structures of the native oxides formed during the wet chemical treatments described above were investigated by non-destructive measurements of the Si 2p photoelectron spectra. We could not determine the native oxide structures, only the amounts of suboxides in the native oxides. There was a clear difference in the distribution of Si^{3+}, while the amounts of suboxides were almost the same for all the treatments investigated. Treatment with HNO_3 resulted in localization of Si^{3+} at the silicon-oxide interface[10]. Si^{3+} is correlated with surface roughness produced by photoexcited dry cleaning.

4. Estimation of cleanliness

The residual concentrations of various elements on the silicon surface were examined by atomic absorption spectrophotometry (AAS). The native oxide on the cleaned surface was vapor etched by HF, and the contaminated HF solution was analyzed. Photoexcited dry cleaning by chlorine was carried out using a clean quartz chamber at 150 °C and 2.7 kPA. Special chlorine gas, 99.999 percent pure, was required. Figure 7 compares the surface cleanliness after wet cleaning alone (i.e. diluted HF, $NH_4OH/H_2O_2/H_2O$, hot HNO_3 cleaning, and deionized water rinsing) with the cleanliness after wet cleaning followed by etching to a depth of 60 nm by photoexcited dry cleaning[11]. The figure shows that the etching reduced the concentrations of Fe, Mg, Ca, and Na. Both wet and photoexcited dry cleaning left no detectable traces of other elements such as Ni, Cr, Al, Cu.

SIMS was used to observe metal contaminants on the surfaces of these wafers after silicon epitaxy. Parts of the wafers were etched to a depth of 20 nm by photoexcited dry cleaning. Then, hydrogen gas annealing was carried out at 980 °C for 15 min, followed by epitaxial silicon deposition at 800 °C in the chamber used for photoexcited dry cleaning. Only K, Na, and Al atoms were detected in a search for K, Na, Al, Fe, Ni, Co, and Cu at the interface (see Fig. 8)[9]. The K atoms were removed by photoexcited dry cleaning. In addition, Na also fell below the limit of detection after photoexcited dry cleaning.

Since the chlorides of K, Na, Mg, and Ca are less volatile, and since these metals and Fe were removed, we postulated the lift-off cleaning model described in the previous chapter.

Intentionally contaminated wafers were used to clarify the effect of cleaning on particular elements. The cleaning characteristics for Fe, the most populous element contaminating ULSI

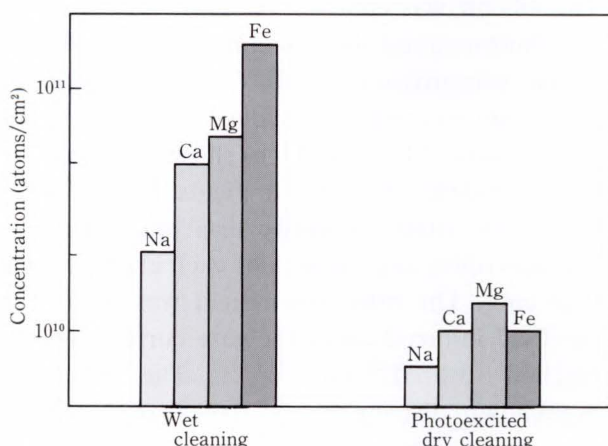

Fig. 7—Surface cleanliness after wet cleaning and after wet cleaning followed be etching to 60 nm by photoexcited dry cleaning[11]. The silicon was not intentionally contaminated.

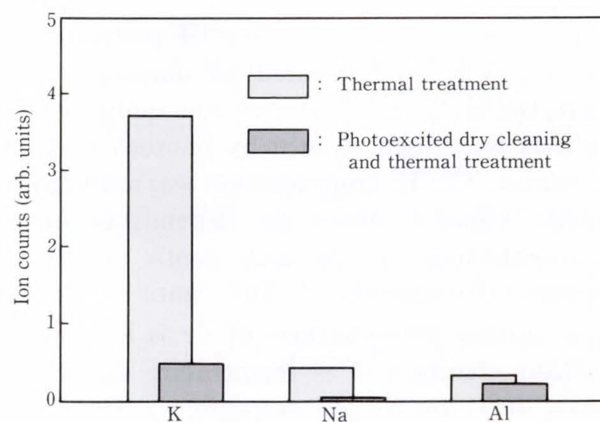

Fig. 8—Effects of thermal treatment at 980 °C with and without prior photoexcited cleaning. Following the thermal treatment, a 1 μm epitaxial layer was grown at 800 °C in Si_2H_6[9].

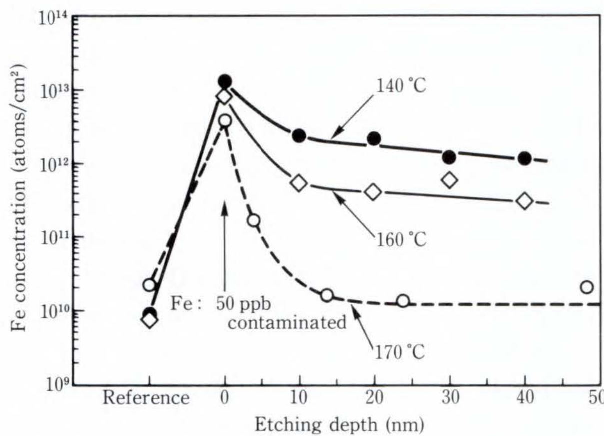

Fig. 9—Fe concentration on silicon surfaces before and after photoexcited dry cleaning[12].
Surfaces were contaminated by immersion in a $NH_4OH/H_2O_2/H_2O$ solution containing 50-ppb Fe and then etched by photoexcited dry cleaning.

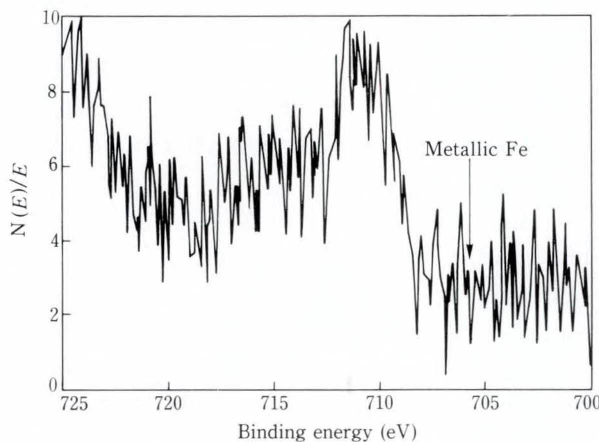

Fig. 10—XPS spectrum of Fe $2p_{3/2}$ region for silicon surface with Fe contaminants[12].

processes, was examined. After HF pretreatment, wafers were contaminated by immersion in a $NH_4OH/H_2O_2/H_2O$ solution containing Fe. The wafers were then cleaned by photoexcited dry cleaning. The Fe concentration was analyzed by AAS. Figure 9 shows the dependence of Fe concentration on the etch depth for photoexcited dry cleaning[12]. The figure shows that the surface concentration of Fe is lowered by silicon etching and is temperature dependent. At 170 °C, the Fe concentration was lowered to about one percent of its initial value, and was below the detection limit. At 140 °C, the Fe concentration was only lowered to about 10 percent of its initial value.

The Fe $2p_{3/2}$ spectrum for a contaminated silicon surface as measured by X-ray photoelectron spectroscopy (XPS) is shown in Fig. 10[12]. The ordinary Fe peak at 706 eV has been shifted up by 5 eV to 711 eV. Contaminating iron atoms bond with oxygen atoms in the native oxide. Since the iron is removed by photoexcited dry cleaning, as shown in Fig. 9, the iron in the native oxide is easily unbound.

5. Electrical Properties

Metal contaminants remaining on the silicon surface degrade the electrical characteristics of fabricated devices, and decrease carrier lifetimes in the silicon. These contaminants can be attributed to resist contamination and process environment contamination.

5.1 Dielectric characteristics of oxides

Dielectric breakdown fields are greatly influenced by metal contaminants[13),14]. Time zero breakdown fields and the time dependent dielectric breakdown (TDDB) characteristics of oxides were investigated after photoexcited cleaning.

MOS capacitors were fabricated on (100)-oriented p-silicon wafers having a resistivity of 10 Ω·cm. The wafers were wet-cleaned using diluted HF treatment, $NH_4OH/H_2O_2/H_2O$ and hot HNO_3 cleaning, and deionized water rinsing. The wafers were then dry-cleaned by photoexcitation. Some wafers were only wet-cleaned. The silicon was etched to a depth of 30 nm by the photoexcited dry cleaning. A gate oxide of 16 nm was grown at 1 000 °C in dry oxygen and aluminum electrodes were deposited by evaporation. Figures 11 a) and 11 b) show histograms of the dielectric breakdown fields of the MOS structures when a negative bias was applied to the electrodes and the area of each electrode was 0.16 cm^2. The breakdown field was defined as the field induced when the gate current density reached 3×10^{-4} A/cm^2 [11]. The dielectric breakdown distribution of dry-cleaned samples was sharper than that of wet-cleaned samples and the field strength was higher. The increase near the intrinsic breakdown value after wet cleaning is due to metallic contamination. The

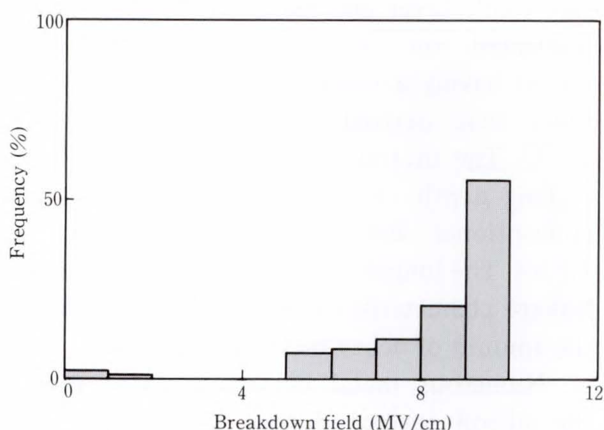

a) After wet cleaning

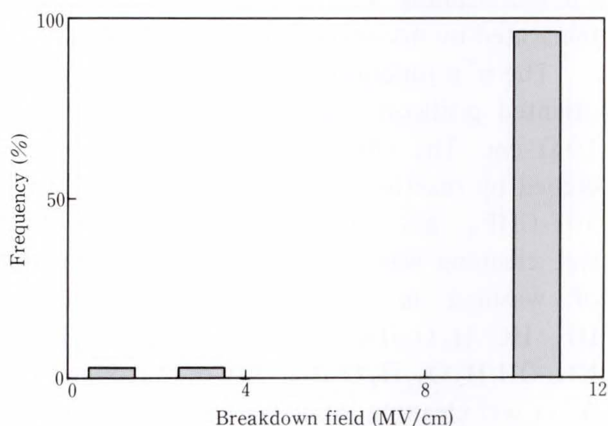

b) After wet cleaning followed by photoexcited etching to 30 nm

Fig. 11–Histograms of dielectric breakdown fields for MOS structures having a 16 nm oxide layer[11].

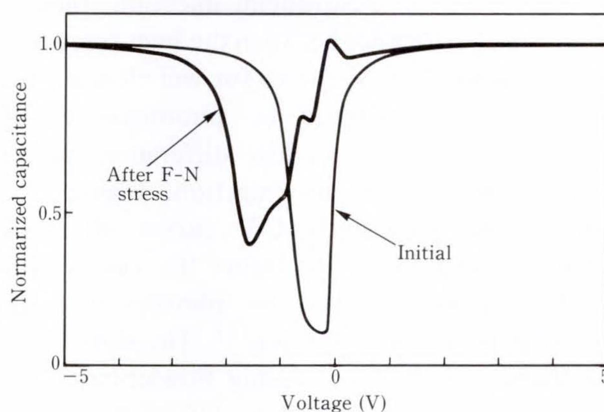

a) After wet cleaning

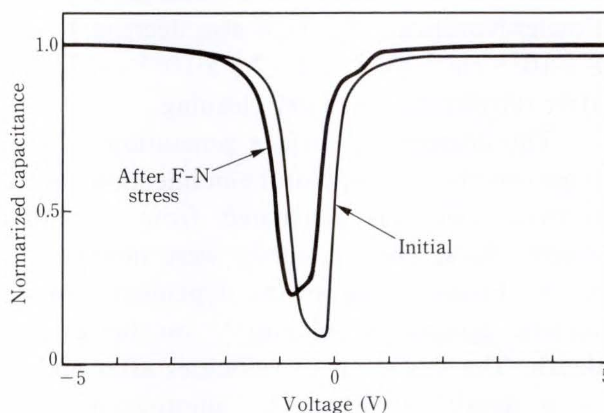

b) After wet cleaning followed by photoexcited dry etching to 6 nm

Fig. 13–Quasi-static C-V curves[15].

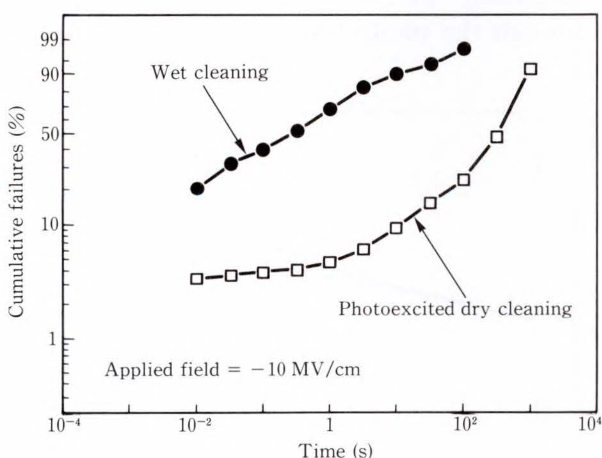

Fig. 12–TDDB characteristics of the oxide layer.

peak value of the breakdown field after photoexcited dry cleaning exceeded 10 MV/cm.

Figure 12 shows the results of TDDB measurements when a constant field of −10 MV/cm was applied to the gate. The figure shows that photoexcited dry cleaning increased the lifetimes of oxide films. Improvements in the oxide TDDB characteristics after photoexcited dry cleaning is also due to the removal of metal contaminants from the surface.

5.2 Silicon-oxide interface characteristics

The flat-band voltage and the interface state density of aluminum-gate MOS capacitors having a 16-nm-thick oxide layer were estimated from high-frequency and quasi-static C-V curves. Fowler-Nordheim carrier injection was performed using a negative bias applied to the gate electrode and a constant current. The current density was 2.6×10^{-5} A/cm^2 and the injection time was 500 s.

Before Fowler-Nordheim injection, there is only small difference between the high-frequency and quasi-static C-V curves for wet cleaning and wet cleaning followed by photoexcited dry cleaning. However, a clear difference appears after Fowler-Nordheim injection. Figure 13 a) shows the quasi-static C-V curves after wet cleaning, and Fig. 13 b) shows the curves after wet cleaning followed by photoexcited dry etching to a depth of 6 nm[15]. The shift in the flatband voltage V_{FB} during Fowler-Nordheim injection stress decreased to 1/5 of its original value after the photoexcited dry cleaning. The interface state density of the mid-gap D_{it} after Fowler-Nordheim injection also decreased from 8×10^{11} cm^{-2} eV^{-1} to 2.5×10^{11} cm^{-2} eV^{-1} after the photoexcited dry cleaning.

The decrease in surface generation velocity improves the Fowler-Nordheim injection characteristics and was calculated from the MOS Zerbst plots. The C-t curves were measured at 50 °C. Figure 14 shows the dependence of the surface generation velocity[11] on the etching depth. The deviation in velocities after etching to a depth of 60 nm by photoexcited dry cleaning was also decreased.

5.3 Carrier lifetime and junction leakage characteristics

The carrier generation lifetimes were evaluated using their dependence on the etching depth of silicon. MOS structures having a 20 nm gate oxide layer and aluminum electrodes were fabricated on (100)-oriented n-type silicon wafers having a resistivity of 1 Ω·cm. The lifetimes were derived from the Zerbst plots at 50 °C. The lifetime increased to 2.5 ms for an etching depth of 50 nm (see Fig. 15)[8]. After conventional wet cleaning the lifetime was 1.6 ms. The longer lifetime improves the junction leakage characteristics and is due to decreases in the amount of heavy metal contaminants.

Numerous metal contaminants adhered to the silicon surface during dry etching[1]. The junction leakage characteristics after photoexcited cleaning were estimated for the samples fabricated by dry etching a field oxide layer.

The n^+p junctions were fabricated on (100)-oriented p-silicon wafers having a resistivity of 10 Ω·cm. The 600-nm field oxide layer was etched by reactive ion etching using a 50%-CF_4/50%-CHF_3 gas mixture. Conventional RCA wet cleaning was done. The cleaning consisted of washing in $NH_4OH/H_2O_2/H_2O$, diluted HF, $HCl/H_2O_2/H_2O$, and then submerging in $NH_4OH/H_2O_2/H_2O$ after RIE of the oxide layer. After wet cleaning, some wafers were cleaned by photoexcited dry cleaning in a 2.7 kPa chlorine atmosphere at 170 °C. The silicon was etched to a depth of 47 nm, then a 5 nm oxide layer was grown at 800 °C in dry oxygen. An arsenic concentration of 4×10^{15}/cm^2 was implanted through the oxide layer at 30 keV. The silicon

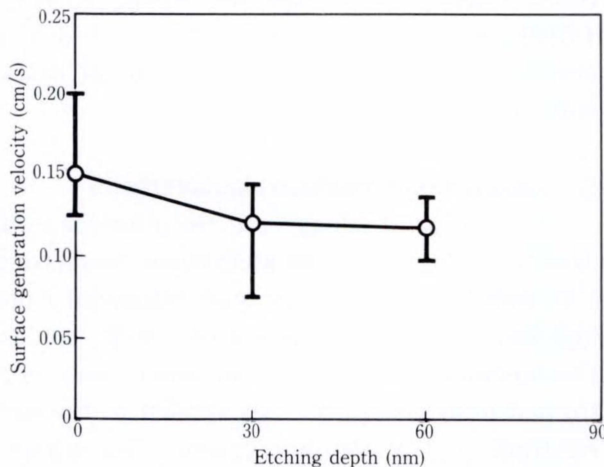

Fig. 14—Dependence of surface generation velocities on photoetching depth[11].

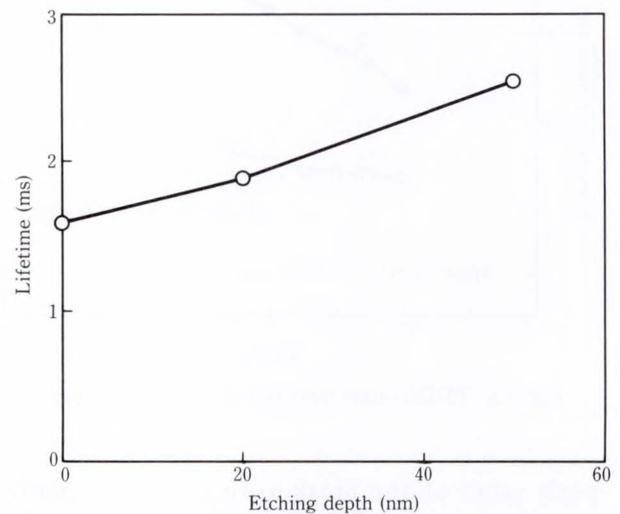

Fig. 15—Dependence of carrier generation lifetime on photoetching depth[8].

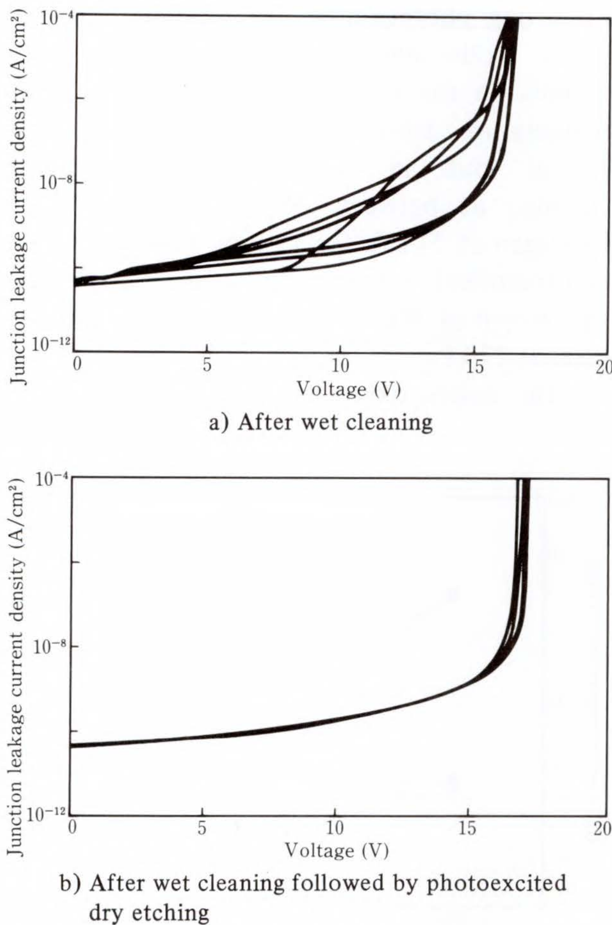

a) After wet cleaning

b) After wet cleaning followed by photoexcited dry etching

Fig. 16—Reverse I-V characteristics of n^+p junction for RIE samples. Cleaning was performed prior to oxidation and arsenic ion implantation[16].

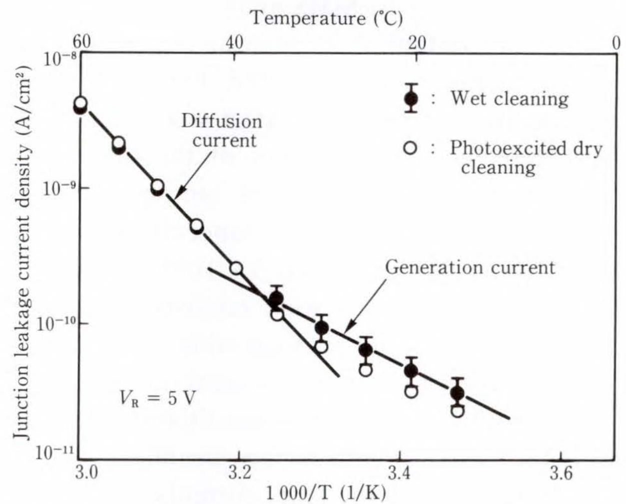

Fig. 17—Temperature dependence of junction leakage currents at reverse bias of 5 V for RIE samples[16].

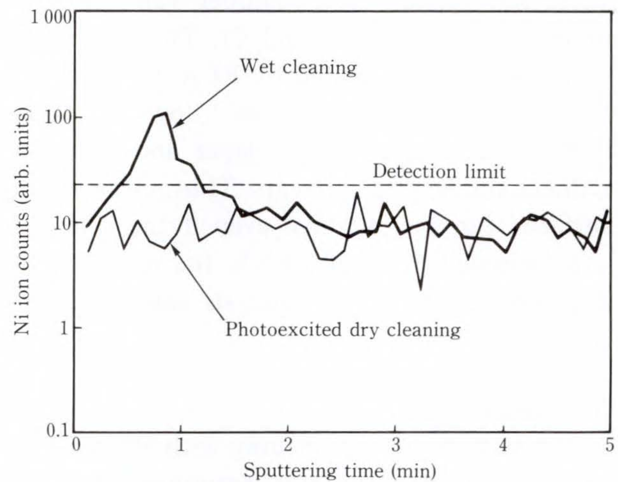

Fig. 18—SIMS depth profiles of Ni in RIE samples[16].

substrates were annealed at 1 000 °C for 20 min in a nitrogen atmosphere to activate the arsenic. Then, the oxide films were removed using a diluted HF solution, and aluminum electrodes containing silicon were sputter-deposited. The wafers were annealed at 450 °C for 30 min in a forming gas (N_2/H_2).

Figure 16 shows the reverse I-V characteristics of the n^+p junctions after wet cleaning and after wet cleaning followed by photoexcited dry etching to a depth of 47 nm for a junction area of 1.13×10^{-2} cm² [16]. Stray currents often appeared after wet cleaning, but did not appear after photoexcited dry etching. The temperature dependence of leakage currents was measured from 10 °C to 100 °C at 5 V reverse bias. Figure 17 shows Arrhenius plots of the temperature dependence of the junction leakage currents for RIE samples after wet cleaning, and after wet cleaning followed by photoexcited dry cleaning. From the slope of the curves, we suspect that the diffusion currents control the leakage current above 40 °C, and that the currents generated by metal contaminants in the depletion layer control the leakage current below 40 °C[17]. The currents generated after wet cleaning were stronger and deviated more than those generated after photoexcited dry cleaning. This suggests that photoexcited dry cleaning removes many of the metal contaminants.

The depth distribution of contaminants was measured by SIMS. There was no clear trace over aluminum, so it must have been removed by the

hot HNO_3 prior to SIMS analysis. A search was made for contaminants such as Fe, Ni, Cr, and Cu, but only Ni was detected. Figure 18 shows the depth profiles of Ni. After wet cleaning, Ni was detected within 30 nm of the silicon surface[16]. By comparing these samples with the control samples, the peak concentration of Ni was found to be about 5×10^{18} atoms/cm^3. The Ni contaminants were removed by photoexcited dry cleaning, suggesting that photoexcited dry cleaning is sufficient to remove all metal contaminants. (High-sensitivity apparatus is required to estimate surface cleanliness.)

It seems that the large currents found after wet cleaning were caused by metal contaminants adsorbed by the silicon substrates during dry etching. During dry etching, F and C ions strike the stainless-steel chamber wall displacing metals such as Fe, Ni, and Cr. These contaminants are not eliminated by RCA wet cleaning. Photoexcited dry cleaning, however, does remove the contaminated layer and therefore reduces the leakage currents. Thus, clean silicon surfaces can be obtained even if the sllicon is contaminated by RIE. Both the temperature dependence and SIMS analysis supported this hypothesis.

5.4 Epitaxy

In silicon epitaxy, etching with HCl and H_2 gas prior to silicon epitaxial growth is often used to remove contaminants and native oxides and to provide a clean silicon surface. However, this method requires a high temperature (about 1 100 °C) to liberate chlorine atoms from HCl molecules. Such a high temperature makes removal of alkali- and heavy-metal contaminants having large diffusion constants nearly impossible. Photoexcited dry cleaning can be used to etch a silicon surface just prior to epitaxy.

Boron-doped p-silicon wafers having a resistivity of 15 Ω·cm and a (100)-oriented surface were cleaned by conventional RCA washing ending in $HCl/H_2O_2/H_2O$ treatment and deionized water rinsing prior to photoexcited dry cleaning. Some of the wafers were etched to a depth of 20 nm during photoexcited dry cleaning at a chlorine pressure of 2.7 kPa at 150 °C. Following photoexcited dry cleaning, the thin native oxide and the volatile chloride compounds on the wafers were removed by high-temperature treatment. This treatment was carried out in the photoexcited-cleaning chamber at between 800 °C and 980 °C in hydrogen at 27 kPa for 15 min. Following thermal treatment, a 1.0 μm epitaxial p-silicon layer was grown at 800 °C in Si_2H_6, B_2H_6, and H_2 gases at 27 kPa.

The native oxide layer containing residual

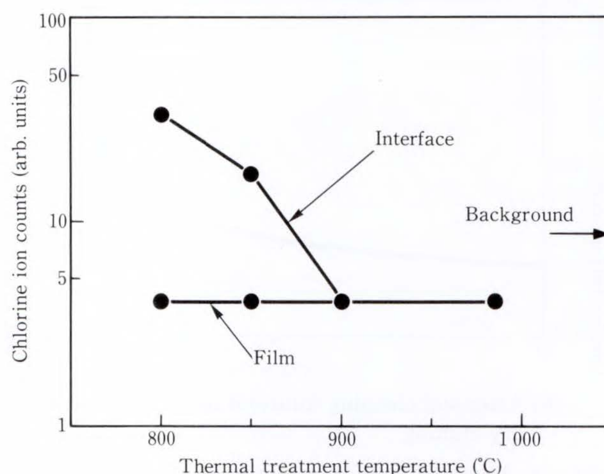

Fig. 19—Chlorine concentrations at the interface and in the deposited film as a function of the thermal treatment temperature[9]. Chlorine remaining after photoexcited dry cleaning is eliminated at 900 °C by treatment in hydrogen at 27 kPa.

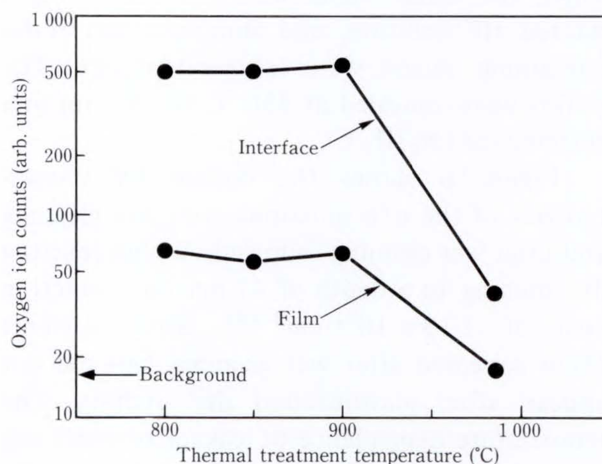

Fig. 20—Oxygen concentrations at the interface and in the deposited film[9]. Oxygen is removed from the surface at 980 °C, a necessity for epitaxial growth.

chlorine remained on the silicon surface after photoexcited dry cleaning (see Fig. 4). This layer must be removed to obtain a clean silicon surface for epitaxy. Figure 19 shows that the chlorine concentration at the interface is minimized at 900 °C. Figure 20 shows that the oxygen concentration at the interface and in the epitaxial film are related and are both minimized at 980 °C[9]. Thus, hydrogen-ambient thermal treatment at 980 °C eliminates volatile chloride compounds and the native oxide layer. The silicon epitaxial layer was only deposited after thermal treatment at 980 °C. An epitaxial wafer was cut along the (110) surface and Secco-etched for 20 s. The cross section was then observed by SEM. We observed no etching pits at the crystal defects of the interface.

Epitaxial wafers were oxidized and an aluminum layer was deposited during the fabrication of MOS capacitors. The breakdown fields of the 20 nm oxide in the accumulation region were measured by ramp I-V analysis. The gate area was 9×10^{-2} cm^2. Figure 21 a) shows the distribution of the dielectric breakdown field after thermal treatment at 980 °C. Figure 21 b) shows the distribution after photoexcited dry cleaning followed by thermal treatment[9]. The figures show that photoexcited dry cleaning improves the breakdown field and eliminates the increase near the intrinsic breakdown value. The average breakdown fields were 10.2 MV/cm after thermal treatment only, and 11.5 MV/cm after the improved process. Because, as was previously mentioned, the contaminants were removed by photoexcited dry cleaning (see Fig. 8), the elimination of the increase near the intrinsic breakdown value must be due to the decreased incorporation of metal contaminants into the oxide. Thus, the new photoexcited dry cleaning procedure is an effective way to produce epitaxial silicon that is free of metal contaminants.

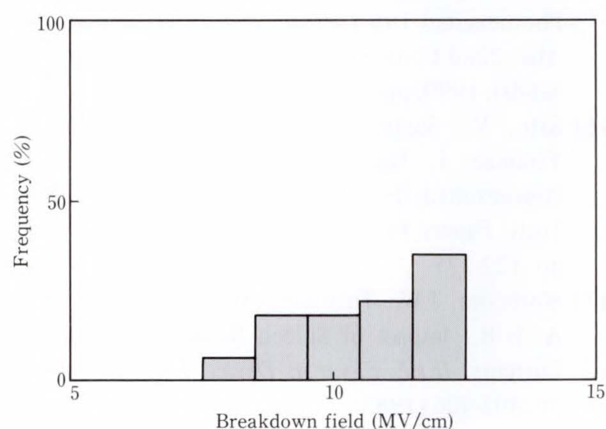

a) After thermal treatment

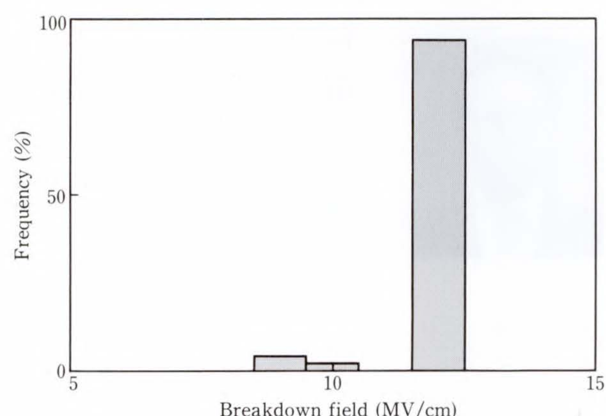

b) After photoexcited dry cleaning followed by thermal treatment

Fig. 21–Distribution of dielectric breakdown field of 20 nm oxide layer on epitaxial silicon surface[9].

6. Conclusion

Photoexcited dry cleaning using chlorine can provide ultraclean silicon surfaces, and can control the surface conditions prior to film deposition. The quality of the oxide layers, silicon substrates, epitaxial films, and their interfaces are improved after photoexcited dry cleaning. The cleaning mechanism, the optimization of the cleaning parameters that affect the surface, the possibility of fully-automated cleaning units, and the methods of evaluating cleanliness should be further investigated.

References

1) Ohsawa, A., Takizawa, R., Honda, K., Matsutani, T., and Imaoka, K.: Improvements of Trench Capacitor Characteristics by Preoxidation Surface Cleaning with a HNO_3-HF-H_2O Solution. Dig. Tech. papers IEEE IEDM '88, 1988, pp. 726-729.

2) Ohsawa, A., Honda, K., Takizawa, R., Nakanishi, T., Aoki, M., and Toyokura, N.: Effects of Impurities on Microelectronic Devices. Proc. 6th Silicon Materials Science and Technology Symp. Semicon-

ductor Silicon/1990 ECS Spring Meet., **PV90-7**, 1990, pp. 601-613.

3) Sugino. R, Nara, Y., Yamazaki, T., Watanabe, S., and Ito, T.: Through-Oxide Cleaning of Silicon Surface by Photoexcited Radicals. Ext. Abs. 19th Conf. Solid State Devices and Materials, Tokyo, 1987, pp. 207-210.
4) Ito, T., Sugino, R., Watanabe, S., Nara, Y., and Sato, Y.: UV-Enhanced Dry Cleaning of Silicon Wafer. Proc. 1st Cleaning Symp. Semiconductor Cleaning Technology/1989 ECS Fall Meet., **PV90-9**, 1990, pp. 114-120.
5) Busch, G. E., Mahoney, R.T., and Morse, K. I.: Translational Spectroscopy, Cl_2 Photodissociation. *J. Chem. Phys.*, **51**, 1, pp. 449-450 (1969).
6) Chuang, T. J.: Laser-Induced Gas-Surface Interactions. *Surface Science Reports*, **3**, 1, pp. 1-105 (1983).
7) Lide, D. R.: Handbook of Chemistry and Physics. 71st ed., 1990, CRC Press, pp. 6.50-6.53.
8) Ito, T, Sugino, R., Yamazaki T., Watanabe, S., and Nara, Y.: Photochemical Cleaning of Silicon Wafers with Halogen Radicals. Ext. Abs. ECS Fall Meet., **87-2**, 1987, pp. 1076-1077.
9) Watanabe, S., Sugino, R., Yamazaki, T., Nara, Y., and Ito, T.: Wafer Cleaning with Photoexcited Chlorine and Thermal Treatment for High-Quality Silicon Epitaxy. *Jpn. J. Appl. Phys.*, **28**, 10, pp. 2167-2171 (1989).
10) Hattori, T., Takase, K., Yamagishi, H., Sugino, R., Nara, Y., and Ito, T.: Chemical Structures of Native Oxides Formed during Wet Chemical Treatments. *Jpn. J. Appl. Phys.*, **28**, 2, pp. L296-L298 (1989).
11) Sugino, R., Takizawa, R., Sato Y., and Ito, T.: Characterization of $Si\text{-}SiO_2$ Interfaces Formed after Photoexcited Cleaning. Ext. Abs. 21st Conf. Solid State Devices and Materials, Tokyo, 1989, pp. 417-420.
12) Sugino, R., Okuno, M., Okui, Y., Shigeno, M., Sato, Y., Ohsawa, A., and Ito, T.: UV-Enhanced Dry Cleaning of Silicon Surfaces Contaminated with Iron and Aluminum. Proc. 2nd Cleaning Symp. Semiconductor Cleaning Technology/1991 ECS Fall Meet., 1992, (to be published).
13) Yamabe, K., Taniguchi, K., and Matsushita, Y.: Thickness Dependence of Dielectric Breakdown Failure of Thermal SiO_2 Films. Proc. Symp. Defects in Silicon ECS Spring Meet., **PV83-9**, 1983, pp. 629-638.
14) Yamabe, K.: Thin Oxides in VLSI. Ext. Abs. 17th Conf. Solid State Devices and Materials, Tokyo, 1985, pp. 261-266.
15) Sato, Y., Sugino, R., Okuno, M., and Ito, T.: Reliability Improvement of MOS Structures Using Photoexcited Dry Cleaning before Oxidation. Ext. Abs. 22nd Conf. Solid State Devices and Materials, Sendai, 1990, pp. 1103-1106.
16) Sato, Y., Sugino, R., Okuno, M., Kikuchi, N., Teramae, J., Ogawa, A., Hijiya, S., and Ito, T.: Photoexcited Dry Cleaning for ULSI Devices. Proc. Tech. Papers Int. Symp. VLSITSA, Taipei, 1991, pp. 122-125.
17) Slotboom, J.W., Theuissen, M. J. J., and de Kock, A. J. R.: Impact of Silicon Substrates on Leakage Currents. *IEEE Electron Device Lett.* **EDL-4**, 11, pp. 403-406 (1983).

Yasuhisa Sato

Semiconductor Devices Laboratory
FUJITSU LABORATORIES, ATSUGI
Bachelor of Metal Eng.
Waseda University 1973
Master of Metal Eng.
Waseda University 1975
Specializing in Semiconductor Processes and Silicon Surface

Takashi Ito

Semiconductor Devices Laboratory
FUJITSU LABORATORIES, ATSUGI
Bachelor of Electronic Eng.
Tokyo Institute of Technology 1969
Dr. of Electronic Eng.
Tokyo Institute of Technology 1974
Specializing in Semiconductor Devices and Processes

Rinshi Sugino

Semiconductor Devices Laboratory
FUJITSU LABORATORIES, ATSUGI
Suzuka College of Technology 1984
Specializing in Semiconductor Processes and Silicon Surface

REVIEW

UDC 621.383.5:621.391.6

Semiconductor Laser Light Sources and Receivers for Next Generation Optical Communication Systems

• Hiroshi Ishikawa *(Manuscript received June 11, 1991)*

Laser light sources and receivers for the next generation of optical communication systems currently being developed in Fujitsu Laboratories Ltd. are reviewed. A modulator integrated DFB laser and APD for high-speed systems, and a multielectrode DFB laser and balanced receivers for coherent communication systems are described.

1. Introduction

In the last decade, much progress has been made in the development of laser light sources and detectors. Highly reliable Fabry-Perot lasers and single longitudinal mode distributed feedback (DFB) lasers with a large modulation bandwidth have been developed. Avalanche photodiodes (APDs) with a gain bandwidth (GB) product of up to 30-40 GHz are now available. These progresses have made it possible to put trunk line systems running at 2 Gbit/s into service. Furthermore, the development of highly reliable lasers has allowed installation of undersea cable systems.

This has prompted discussion on the next generation of systems which will provide a variety of services and will be accessible to subscribers from the home or office. An example of such a system is the Broadband Integrated Service Digital Network (B-ISDN) from NTT. Development will start in 1995 and will eventually extend to a nation-wide fiber to the home system by the year 2015[1]. In such a system, the network of customer premises is likely to run at between 100 Mbit/s and several Gbit/s, while the required capacity for the public access network is estimated to be 100 Gbit/s[2]. The trunk line may even require terabit per second capacity.

One way to realize such high transmission capacities is to increase the modulation bit-rate of intensity modulation and direct detection (IM/DD) to a maximum, then perform wavelength division multiplexing (WDM)[2]. Present electrical multiplexing technology would limit the maximum bit-rate to around 10 Gbit/s. The other attractive possibility is coherent transmission, which allows very long distance transmission and very dense optical frequency division multiplexing; this gives a huge transmission capacity and a multichannel network accessible by customers. Optical frequency division multiplexing (FDM) of 100 channels, each running at 2 Gbit/s with 10 GHz (0.08 nm) spacing, will combine to give a capacity of 200 Gbit/s.

Enormous efforts will have to be made on device development if such systems are to be realized. Much greater performance and new functions are needed from the light sources and receivers. Low cost devices satisfying stringent requirements are also essential for the low bit-rate customer network.

In this review, we focus on the light sources and receivers for very high bit-rate IM/DD systems and coherent transmission

systems. The following describes achievements made so far and touches on problems yet to be resolved. A modulator integrated DFB (MI-DFB) laser[3] and a high-speed APD[4] for high-speed IM/DD systems, and a new multielectrode DFB laser[5),6], balanced detectors[7] and an integrated coherent receiver[8] for coherent systems are discussed.

2. Devices for high-speed intensity modulation systems

2.1 Background

Research and development of semiconductor lasers has been directed to attain high-speed single mode operation. So far, a single mode DFB laser with 3 dB bandwidth of 15 GHz has been achieved[9),10]. However, high-speed direct modulation of the DFB laser causes wavelength chirp, and this limits transmission distance due to dispersion in the fiber. It has been estimated that the dispersion of a fiber we can transmit with penalty less than 0.5 dB is 200 ps/nm under 3 Gbit/s modulation[11]. This corresponds to about 70 km for typical zero dispersion fiber, and to only 10 km for non-dispersion shifted fiber at 1.55 μm. The figures are even more critical at 10 Gbit/s; for 10 Gbit/s modulation, wavelength chirp reaches 1 nm (full width at 15 dB).

To facilitate transmission over 50-100 km at 10 Gbit/s using typical zero dispersion fiber, the wavelength chirp should be below 0.1 nm[11]. One way to reduce the chirp is to introduce a multiple quantum well (MQW) active layer. The MQW active layer reduces the refractive index change under high-speed modulation and results in a smaller wavelength chirp. However, chirp is still about 0.5 nm[10]. We have therefore taken a different approach and introduced external modulation. We developed a monolithic light source by integrating a modulator and a DFB laser into one chip, i.e. a modulator integrated (MI-DFB) laser[3].

On the detector side, an InGaAs/InP APD has been developed to take advantage of its multiplication gain which gives high sensitivity without the thermal noise of an electrical amplifier[12]. It is necessary to have a large GB product with a bandwidth close to 10 GHz. However, in the InGaAs/InP APD, this is difficult as holes pile up at the heterojunction[12]. A large GB could only be obtained at a large multiplication factor, and so the bandwidth was narrow. We solved this problem by introducing a graded layer at the heterointerface. We also optimized the field distribution further to increase the GB product.

2.2 Modulator integrated DFB laser

Figure 1 shows a schematic of the MI-DFB laser, a Franz-Keldysh modulator was used. The DFB laser wavelength is 1.55 μm. For this wavelength the composition of the absorption layer was selected to be 1.43 μm. When a reverse biased voltage is applied to the modulator, the absorption edge shifts to the longer wavelength and the laser light is modulated by absorption. The composition of the absorption layer was

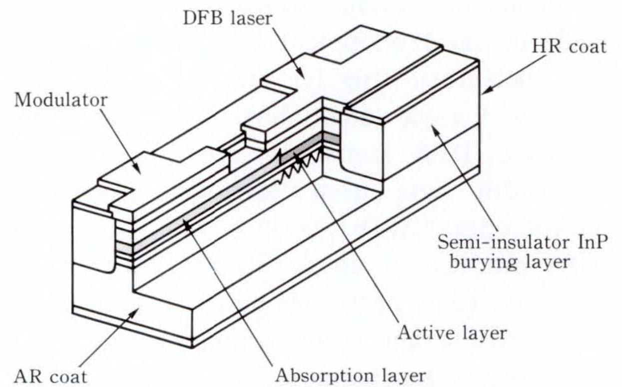

Fig. 1—Modulator integrated DFB laser.

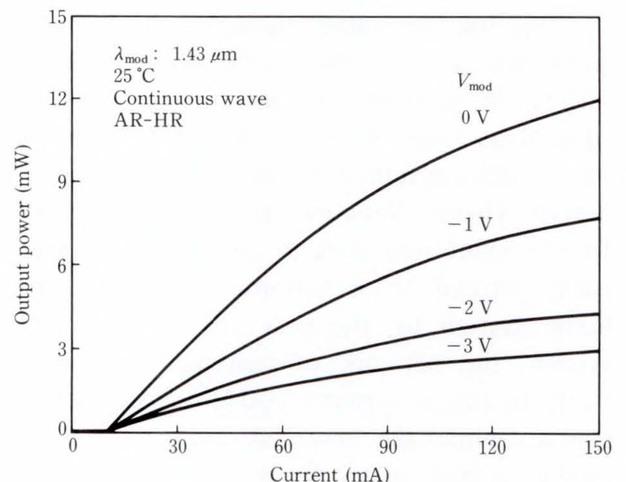

Fig. 2—Current versus light output characteristics.

adjusted to allow a smaller operating voltage with less insertion loss.

There are three key points to note when producing a high-performance integrated device. The first one concerns electrical isolation between the forward biased DFB laser and the reverse biased modulator. The isolation resistance must be high, and to achieve this, a semi-insulator embedded buried heterostructure (BH) was used. This raised the isolation resistance to more than 100 kΩ.

The second point concerns the optical coupling between the DFB laser and the external modulator. To achieve a high coupling efficiency, a new layer structure was used, with a thin InP layer and a guiding layer, common both for the DFB laser and the modulator. The butt-joint was formed by liquid phase epitaxy (LPE) on a thin InP layer. This layer structure gives a high coupling efficiency of about 80 percent.

The third point concerns the anti-reflection (AR) coating on the modulator output facet. Light reflected at this facet causes unstable operation of the DFB laser. Reflectivity was reduced below 0.1 percent by using an AR coating with SiN. At the DFB laser facet, a high reflectivity (HR) coating with reflectivity of about 80 percent was used to increase light output from the modulator.

Figure 2 shows light output power versus current. As voltage applied to the modulator increases, light output decreases, until the reduction saturates at –3 V. There is still some output power at this voltage, due to scattered light at the butt-joint. When the output power was coupled to a single mode fiber, an extinction ratio of –13 dB for an applied voltage of –3 V was attained.

Figure 3a) shows the eye pattern for 10 Gbit/s NRZ modulation, observed by a PIN photodetector; a clear eye opening was produced. Figure 3b) shows the spectrum for the same modulation. The full width at –15 dB of the maximum was 0.032 nm, which is drastically reduced when compared with direct modulation of a DFB laser.

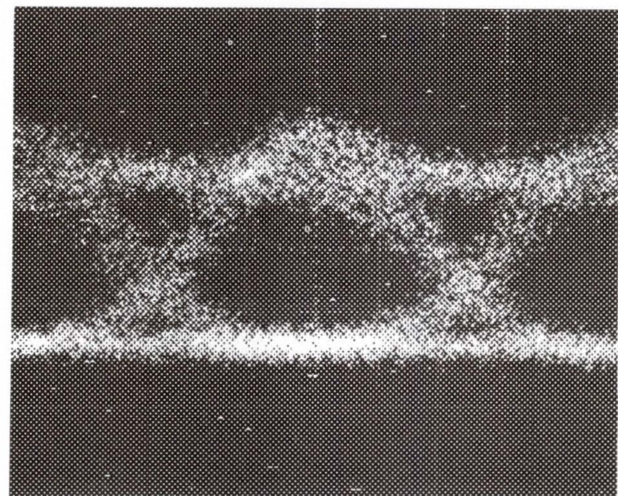

a) Eye pattern

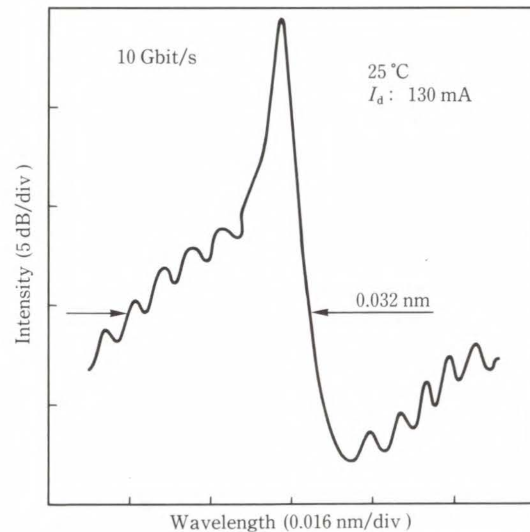

b) Time averaged spectrum

Fig. 3–A 10 Gbit/s NRZ modulation.

2.3 High-speed APD with optimized field profile and graded heterointerface

The insert of Fig. 4 shows the layer structure of the newly developed APD: an InP buffer layer, an InGaAs absorption layer, a compositionally graded undoped layer, an n^+-InP electric field falling layer, and an InP window layer. The thickness of the InP multiplication layer was controlled by the depth of the p^+ layer by Cd diffusion. An ion-implanted Be guardring was used to make the planar junction. The graded layer stops holes piling up, and the n^+ field falling layer prevents impact ionization in the InGaAs absorption layer.

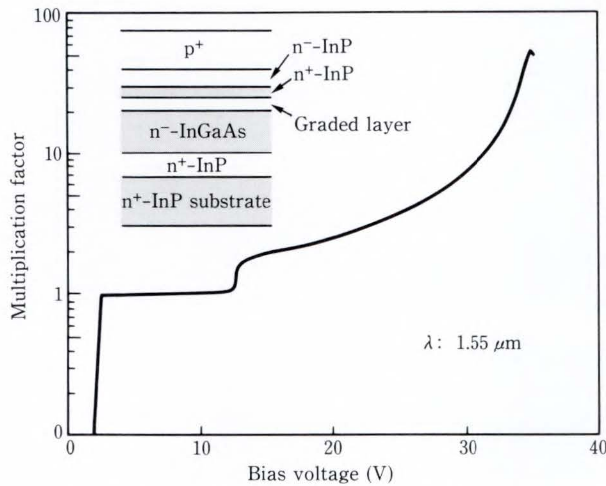

Fig. 4–Multiplication factor versus bias voltage. Inset shows APD layer structure.

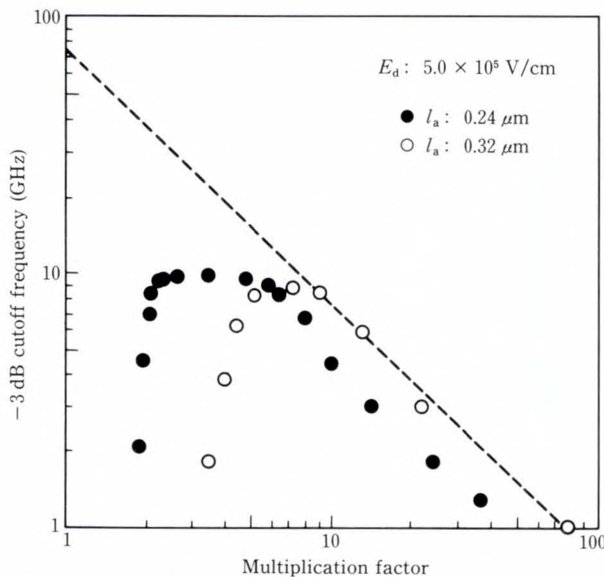

Fig. 5–Cutoff frequency versus multiplication factor.

Figure 4 shows multiplication factor as a function of bias voltage. The breakdown voltage was less than 40 V and at 90 percent of the breakdown voltage, the dark current was less than 50 nA.

Figure 5 shows −3 dB cutoff frequency versus multiplication factor for two samples with multiplication layer thicknesses of 0.24 μm and 0.32 μm. The electric field falling at the n^+-InP layer is 5×10^5 V/cm. For the 0.32 μm multiplication layer, the GB product was 70 GHz and the maximum cutoff frequency was 9 GHz.

Even for a small multiplication factor, the bandwidth was large, and this was due to the graded layer which prevented hole pile up. For a thicker multiplication layer, the GB product is large since the overall electric field of the diode is lower; GB product increases due to avalanche suppression in the InGaAs absorption layer.

2.4 Discussion

The MI-DFB laser exhibited a very low chirp of 0.032 nm and good eye opening at 10 Gbit/s modulation, an output power of 10 mW was achieved. Using this monolithic device, transmission over a dispersion of 230 ps/nm at 10 Gbit/s with a penalty less than 0.5 dB is possible[13]. At the lower bit-rate of 2.4 Gbit/s, the limit exceeds 2 000 ps/nm[11]. However, the operating voltage still remains rather high at −3 V. This operating voltage must be reduced for modulation using an IC driver. It will be possible to reduce it to −2 V by optimizing the composition of the absorption layer further, and by increasing the power of the DFB laser. The APD with a graded layer and an optimized field profile gave a GB product of 70 GHz. The large 9 GHz bandwidth enables this device to be used for 10 Gbit/s systems. Even greater optimization will make possible a GB product of 100 GHz.

The combination of the MI-DFB laser and the APD will enable transmission around 70 km at 10 Gbit/s using a typical zero dispersion fiber. This is a very great improvement over the direct laser modulation and conventional APD system[13]. However, the MI-DFB should be compared with a lithium niobate (LN) Mach-Zehender modulator[14]. The LN modulator can, in principle, reduce wavelength chirp to zero, and transmit over several hundred kilometers using fiber amplifiers. But the MI-DFB laser is very much smaller and easier to use, by virtue of its monolithic integration of the modulator and the DFB laser. The MI-DFB laser can be a very practical high-speed light source.

3. Devices for coherent systems

3.1 Background

Lasers for coherent communication systems must satisfy a variety of requirements. The laser must be tunable so that the wavelength of the transmitter and the local oscillator can be adjusted for heterodyne detection. A very narrow linewidth is also required. For example, for continuous phase frequency shift keying (CPFSK), a linewidth less than 10^{-3} times the modulation bit-rate is necessary[15]. Therefore for a bit-rate of 1 Gbit/s, lasers with linewidth less than 1 MHz must be made. Futhermore these lasers must have flat FM response from 100 kHz to several times the modulation bit-rate to get a clear eye opening. For the local oscillator, a laser with a higher output power is better, to give a larger beat signal for heterodyne detection.

It has been very difficult to satisfy all these requirements, especially the rather contradictory requirements of both narrow linewidth and wavelength tunability. For the first time, we created such a laser by using a new wavelength tuning mechanism: a three-electrode, long cavity λ/4 shifted DFB laser[5),6)].

For coherent detection, the receiver must have new capabilities; a dual-balanced optical receiver, using two photodiodes in a balanced mixer configuration, is an absolute necessity. It cancels excess intensity noise generated by the local oscillator laser, and it uses the available signal power efficiently. We integrated two finely-balanced PIN photodiodes (twin-PIN photodiode) to make a balanced detector, and developed a quad-PIN photodiode by combining two pairs of twin-PIN photodiodes. This quad-PIN photodiode enables polarization diversity coherent detection. The balanced PIN-photodiodes were designed in a flip-chip configuration to reduce parasitic capacitance.

To make a more advanced and convenient receiver, it will be necessary to integrate the optical coupler, balanced detector, local oscillator laser, and electrical preamplifier[16)]. We have taken the first step toward trying this integration.

3.2 Three-electrode, long cavity λ/4 shifted DFB laser

Figure 6 shows a schematic diagram of the laser. Cavity length is 900 μm and an MQW active layer is introduced. The long cavity gives a large Q-factor and the MQW active layer gives a smaller linewidth broadening factor. These result in a narrow spectral linewidth. The quarter wavelength shift in the grating and multiple electrodes provide a means to tune the wavelength. We can tune the wavelength by changing the current to each electrode. Typically, the side electrodes are connected and the center current I_C is changed to tune the wavelength. This is a new tuning mechanism[5),6)]. The quarter wavelength shift causes intense spatial hole-burning; the carrier concentration is de-

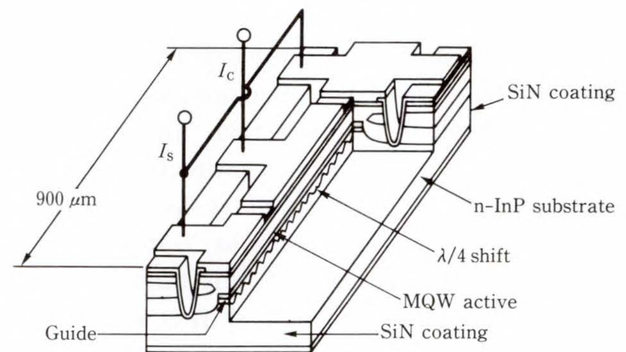

Fig. 6—Three-electrode λ/4-shift MQW DFB laser.

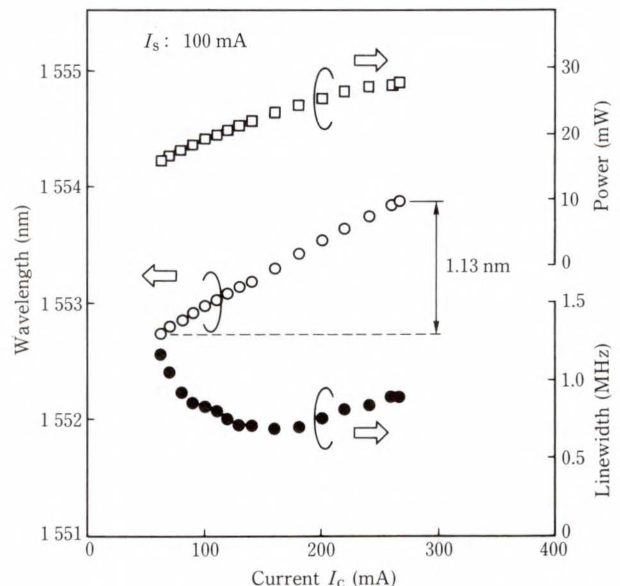

Fig. 7—Wavelength tuning characteristics.

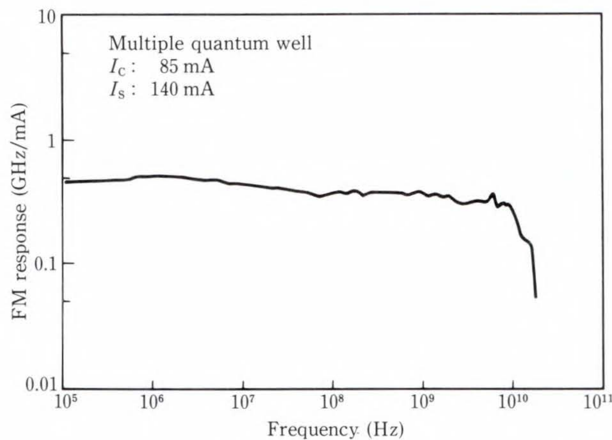

Fig. 8–FM response.

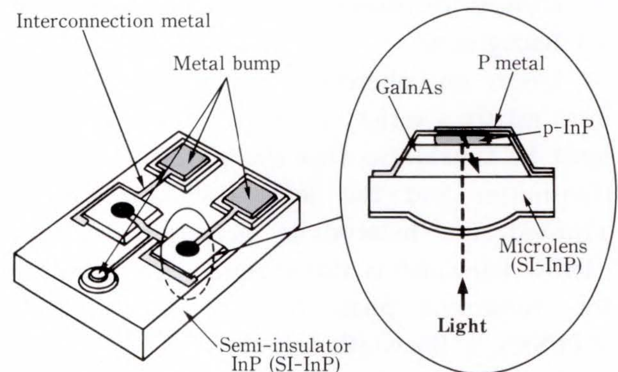

Fig. 9–Twin-PIN photodiode.

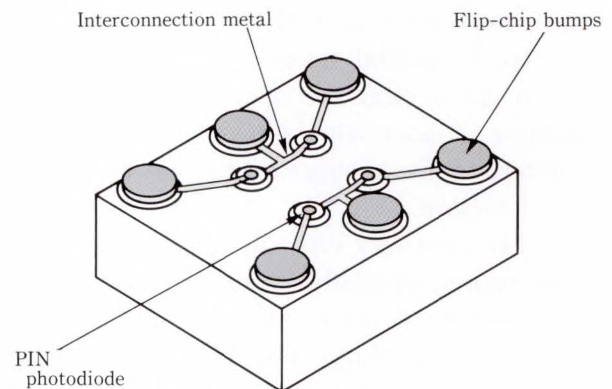

Fig. 10–Quad-PIN photodiode.

pressed at the center of the cavity. This carrier depression is controlled by selectively injecting carriers using the multiple electrodes; this charges the refractive index and hence shifts the wavelength.

Figure 7 shows an example of tuning characteristics. The wavelength becomes longer as the center current I_C is increased. The linewidth was around 1 MHz for the entire tuning range of 1.13 nm, and it reduced as I_C in creased. Output power was high at about 20 mW.

A particular feature of this tuning mechanism is that the wavelength shift is a red shift: the wavelength becomes longer as the center current I_C is increased. In the conventional DFB laser, the tuning mechanism is predominantly a blue shift, which is opposite to the thermal effect, and its FM response dips around 1 MHz due to the compensating effects of the thermal red shift and the carrier effect blue shift. The wavelength tuning of our laser has a red shift, and this gives a flat FM response as shown in Fig. 8. This gives good eye opening.

3.3 Flip-chip twin-PIN and quad-PIN photodiode

Figure 9 illustrates a monolithic twin-PIN photodiode with flip-chip configuration. PIN photodiodes are back-illuminated with a monolithic lens to couple the optical fiber. Metal bumps surround the photodiodes for flip-chip bonding. The photodiode consists of an n-InP top layer, an n-InGaAs absorption layer and an n-InP contact layer. The photodiode junction has a diameter of 20 μm, and was formed by selective Zn diffusion; a mesa structure was used for electrical isolation. The two microlenses were fabricated by Ar ion beam etching. The bandwidth of the twin-PIN photodiode was 13 GHz at 3 dB, helped by the low capacitance of 80 fF owing to the flip-chip bonding. The quantum efficiency was 80 percent and the common mode rejection ration (CMRR) was −30 dB up to 7 GHz.

Figure 10 shows how two twin-PIN photodiodes were combined to produce a quad-PIN photodiode for polarization diversity coherent detection. The two twin-PIN photodiodes were integrated monolithically. Figure 11 is a flip-chip bonded quad-PIN photodiode. Four monolithic lenses are visible, and these monolithic lenses give a uniform and large photosensitive area of 70 μm for each diode. Figure 12 shows the frequency response and the CMRR for the pair of diodes. There is a large bandwidth and

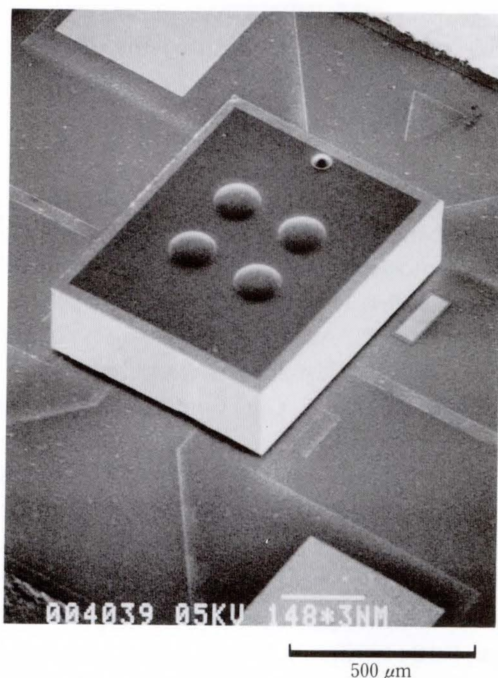

Fig. 11–Flip-chip bonded quad-PIN photodiode.

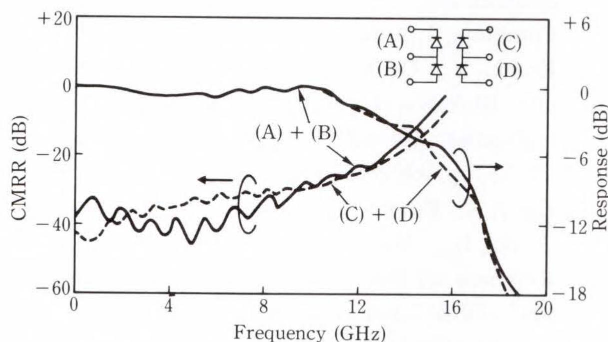

Fig. 12–Frequency response and common-mode suppression ratio for diode pairs.

common-mode rejection ratio of –30 dB up to 10 GHz. The crosstalk between the two twin-PIN photodiodes was below –40 dB, up to 14 GHz.

3.4 Integrated coherent receiver

Figure 13 shows an attempt to make an integrated coherent receiver[8]. There is a waveguide coupler on one side of the chip and balanced PIN photodiodes with interdigitated contacts on the other. The waveguide coupler and the detectors are optically coupled by a monolithic mirror. The waveguide coupler is a diluted MQW layer, which gave a low propagation loss of 0.5 dB/cm and large numerical

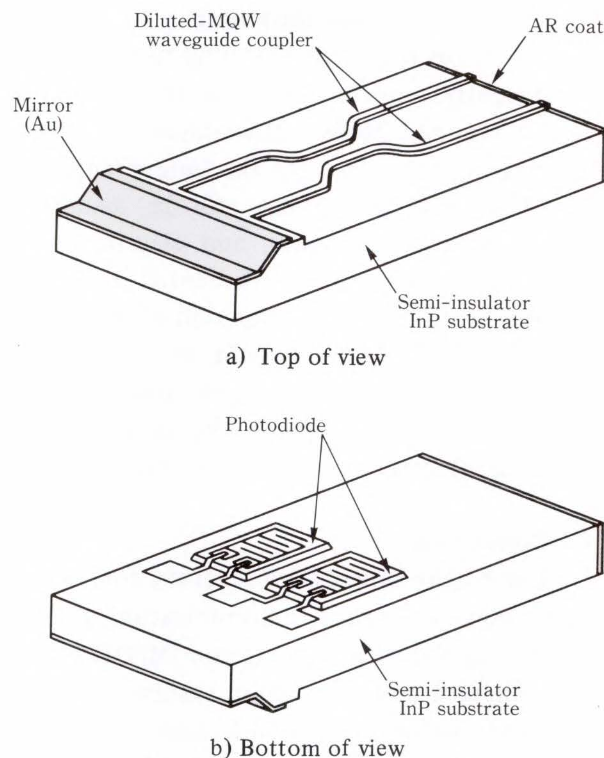

Fig. 13–A monolithic receiver.

aperture (NA). The coupling loss to a single mode fiber was 0.9 dB. Recent improvements in the PIN photodiode have raised quantum efficiency to 85 percent, with a deviation of one percent between the two diodes for an applied voltage of 5 V. This receiver operated as an integrated device, giving a beat signal output.

3.5 Discussion

A transmission experiment using the three-electrode $\lambda/4$ shift DFB laser and the twin-PIN photodiodes was performed for CPFSK modulation[17]. At 4 Gbit/s, sensitivity was high at 100 photons/bit, and transmission over 233 km was achieved. An experiment on polarization diversity transmission was also conducted using two twin-PIN photodiodes at 2.5 Gbits/s[17], and gave a span loss margin of 53.2 dB and transmission over 254 km. The required level of performance to conduct the transmission experiments was achieved for both the laser and the detector.

However, there are some problems to be overcome to make further progress. For one, the tuning range of the laser is rather narrow. For optical frequency division multiplexing of

100 channels, a local laser with a tuning range of 8-10 nm is required. A tuning range of 7 nm was recently reported for a similar laser, which used a strained MQW active layer[18]. This is encouraging for increasing the tuning range. The quad-PIN photodiode has still be assembled, with a polarizer, coupler, and electric preamplifier before it can be implemented in systems. A monolithic device in which all of these components are integrated would be most useful. Trials for such integration have already started, but much work remains to be done before a practical integrated device can be built.

4. Conclusion

Laser light sources and receivers for the next generation of optical communication systems, specifically for very high bit-rate IM/DD systems and coherent communication systems have been reviewed. Using an MI-DFB laser, wavelength chirp has been reduced remarkably and a GB product of 70 GHz with a 9 GHz bandwidth has been attained in an APD. A multielectrode DFB laser with a linewidth below 1 MHz, 1.13 nm tuning range and good FM response has been also been achieved. The balanced detectors, twin-PIN and quad-PIN photodiodes gave a good common mode rejection ratio. Trials on an integrated coherent receiver were also conducted. The achievements made it possible to perform IM/DD transmission at 10 Gbit/s over 65 km[13], and coherent transmission at 4 Gbit/s over 233 km[17].

These achievements are the first step toward the next generation of systems. There remains much work to be done to make these devices perform satisfactorily. The key to further progress is better growth and processing technology. For example, the wavelength variance of DFB lasers with conventional technology is around ±5 nm. This is quite insufficient for wavelength division or optical frequency division multiplexing for large capacities. Growth and processing technology must be developed to give precise control over layer thickness, composition and stripe width to reduce wavelength variance. This is also true for other integrated devices which require precise control of dimensions. To develop the next generation of devices, efforts should concentrate on improving growth and processing technology, and exploiting the structure of these devices.

References

1) Kuwabara, M.: 21st Century Telecommunication and Optoelectronics. Tech. Dig. 3rd Optoelectron. Conf., Chiba, 1990, pp. 4-5.
2) Kurokawa, K.: Advanced Technologies for Business and Private Customer Access Networks. Proc. 16th Europ. Conf. Opt. Commun., 2, Amsterdam, 1990, pp. 679-686.
3) Soda, H., Furutsu, M., Sato, K., Okazaki, N., Yamazaki, S., Nishimoto, H., and Ishikawa, H.: High-power and High-speed Semi-insulating BH structure Monolithic Electroabsorption Modulator/ DFB Laser Light Source. *Electron. Lett.*, **26**, 1, pp. 9-10 (1990).
4) Kuwatsuka, H., Kito, Y., Ito, M., and Mikawa, T.: Design of Ultra-high-speed InP/InGaAs Avalanche photodiodes. Proc. 16th Europ. Conf. Opt. Commun., 1, Amsterdam, 1990, pp. 385-388.
5) Kotaki, Y., Ogita, S., Matsuda, M., Kuwahara, Y., and Ishikawa, H.: Tunable narrow-linewidth and high-power λ/4-shifted DFB Laser. *Electron. Lett.*, **25**, 15, pp. 990-992 (1989).
6) Ogita, S., Kotaki, Y., Matsuda, M., Kuwahara, Y., Onaka, H., Miyata, H., and Ishikawa, H.: FM Response of Narrow-linewidth, Multielectrode λ/4 Shift DFB Laser. *Photonic Technol. Lett.*, **2**, 3, pp. 165-166 (1990).
7) Makiuchi, M., Hamaguchi, H., Kumai, T., Kuramata, A., and Wada, O.: High-speed Monolithic GaInAs TWIN-*pin* Photodiode for Balanced Optical Coherent Receivers. *Electron. Lett.*, **25**, 17, pp. 1144-1145 (1989).
8) Deri, R.J., Sanada, T., Yasuoka, N., Makiuchi, M., Kuramata, A., Hamaguchi, H., Wada, O., and Yamakoshi, S.: Low-loss Monolithic Integration of Balanced Twin-Photodetectors with a 3 dB Waveguide Coupler for Coherent Lightwave Receivers. *Photonic Technol. Lett.*, **2**, 8, pp. 581-584 (1990).
9) Sugano, M., Sudo, H., Soda, H., Kusunoki, T., and Ishikawa, H.: Effects of Zinc Doping in DFB Lasers Emitting at 1.3 and 1.55 μm *Electron. Lett.*, **26**, 2, pp. 95-96 (1990).
10) Uomi, K., Sasaki, S., Tsuchiya, T., Aoki, M., Nakano, H., and Chinone, N.: High speed 1.55 μm MQW-DFB Lasers. Tech. Dig. 3rd Optoelectron.

Conf., IECE, Chiba, 1990, pp. 26-27.
11) Nishimoto, H., Shirasaki, M., Okiyama, T., Yokota, I., Soda, H., Seino, M., and Touge, T.: Modulation Schemes for Multi-gigabit Optical Transmission Systems. Proc. IEEE Global Telecommun. Conf., Hollywood, 1988, pp. 487-491.
12) Imai, H., and Kaneda, T.: High-speed Distributed Feedback Lasers and InGaAs Avalanche Photodiodes. *J. Lightwave Technol.*, **LT-6**, 11, pp. 1634-1642 (1988)
13) Okiyama, T., Yokota, I., Nishimoto, H., Hironishi, K., Horimatsu, H., and Touge, T.: A 10-Gb/s, 65-km Optical Fiber Transmission Experiment Using a Monolithic Electroabsorption Modulator/DFB Laser Light Source. Proc. 15th Europ. Conf. Opt. Commun., **1**, Gothenburg, 1989, pp. 1-4.
14) Seino, M., Shiina, T., Mekada, N., and Nakajima, H.: Low-loss Mach-zehender modulator using mode coupling Y-branch waveguide. Proc. 13rd Europ. Conf. Opt. Commun., **1**, Helsinki, 1987, pp. 113-116.
15) Iwashita, K., and Matsumoto, T.: Modulation and Detection Characteristics of Optical Continuous Phase FSK Transmission System. *J. Lightwave Technol.*, **LT-5**, 4, pp. 452-460 (1987).
16) Takeuchi, H., Kaseya, K., Kondo, Y., Yasaka, H., Oe, K., Imamura, Y.: Monolithic Integrated Optical Circuit for Coherent Detection. Tech. Dig., 7th Int. Conf. Integ. Opt. Optic. Fiber Commun., **5**, Kobe, 1989, pp. 48-49.
17) Chikama, T., Naito, T., Kiyonaga, T., Isahikawa, G., and Kuwahara, H.: Optical Heterodyne Continuous Phase FSK Transmission Experiment up to 4 Gb/s. Proc. 16th Europ. Conf. Opt. Commun., **1**, Amsterdam, 1990, pp. 65-68.
18) Kuindersma, P.I., Scheepers, W., Cnoops, J.M.H., Thijs, P.J.A., Hofstad, G.L.A.v.D., Dongen, T.V., and Binsma, J.J.: Tunable Three-section, Strained MQW PA-DFB's with Large Single Mode Tuning Range (72 Å) and Narrow Linewidth (around 1 MHz). Conf. Dig., 12th IEEE Int. Semicond. Laser Conf., Davos, 1990, pp. 248-249.

Hiroshi Ishikawa

Optical Semiconductor Devices Laboratory
FUJITSU LABORATORIES, ATSUGI
Bachelor of Electronics Eng.
Tokyo Institute of Technology 1970
Dr. of Electronic Eng.
Tokyo Institute of Technology 1984
Specializing in Optical Semiconductor Devices

UDC 512.714:681.32

Report on Computer Algebra Research

● Taku Takeshima ● Masayuki Noro ● Kazuhiro Yokoyama

(Manuscript received June 3, 1991)

Computer algebra is a newly developing research area that bridges constructive mathematics and scientific information processing technology. Research in this area includes design, analysis, and prototyping of mathematical algorithms for symbolic and algebraic computation.

This paper describes an experimental system for computer algebra, named *risa – Research Instrument for Symbolic Algebra*. At present, the system forms the basic kernel of a computer algebra system, and is expected to become an essential engine for advanced future systems. As a general-purpose computer algebra system, risa's operating speed is competitive and sometimes outstanding. This paper also briefly describes several mathematical results of some algebraic computations related mainly to polynomials.

1. Introduction

Computer algebra systems are powerful tools of science and technology. By using a computer algebra system, scientists and engineers can fully exploit the available computer power to carry out the long and tedious processes involved in computing large expressions.

At the beginning of the computer algebra era, the 1950's and 1960's, the key technologies of computer algebra systems were *symbolic manipulation* and *artificial intelligence.* In these decades, it was realized that a purely symbolic (i.e. non-algebraic) approach to many *simple* problems tended to explode in terms of time and storage. As far as computer algebra is concerned, advanced artificial intelligence technology based on the simulation of human heuristic processes can solve only small sized problems that are solvable even by human calculation.

As a consequence, the simple strategy of using symbolic manipulation and artificial intelligence had to be reconsidered. Modern computer algebra systems deeply depend on efficient *algebraic algorithms* (e.g. factorization of polynomials) that were developed through investigating algebraic structures of mathematical objects. This relationship is similar to the way modern numerical computing technology depends on the various numerical algorithms designed through numerical analysis. The research on these algebraic algorithms is called *computer algebra.* Although symbolic technology is still a useful way to improve system performance, its importance has decreased. The application of artificial intelligence (AI) to practical problems is a long way off. AI may help improve the user interface, for example, by helping the user to choose the best algorithm from several alternatives, but there is no known definite choice criterion.

In the following chapters, we describe our experimental system for computer algebra, *risa.* Also, we show several mathematical results for efficient computations that are mainly related to polynomials.

2. Risa – an experimental computer algebra system

Risa (Research Instrument for Symbolic Algebra) is a computer algebra system that, although currently limited, has great potential. It was developed and will continue to be developed as a practical tool for professional

computation in mathematical sciences and engineering. At present, risa forms the basic kernel of a computer algebra system that realizes arbitrary precision integer arithmetic and polynomial arithmetic together with a simple programming language called *asir*. By taking advantage of its *independent open module structure*, risa will be improved step by step in terms of its variety of service functions and performance. Risa mostly uses the theoretically and/or empirically best algorithms (algebraic and symbolic) that are available.

Computing data and timing data are shown in the following sections. All timing data shown in this paper was measured on an S4/370 (Sparc Station 370) with 32 Mbytes of real memory and 64 Mbytes of virtual memory.

2.1 Design principle of the risa scientific computation system

Risa was designed to be an indispensable component of future *scientific computation systems.* The technology that is now being evaluated is the *independent open module* structure. Risa is a collection of independent open modules. Basically, risa is a collection of UNIX[note)] libraries. Each UNIX library (i.e. each module) is a set of mutually related functions that performs a significant task. For example, basic algebraic computation, complex algebraic computation, basic numerical computation, graph plotting, and programming language interpretation and evaluation. Editors, two-dimensional formatters, numerical software, and high-quality graphic software are not of prime interest in our current computer algebra research. Therefore, they are not included in the current risa system. Regarding the programming environments, for example, editors, we recommend that the user should use the most convenient and familiar environment. Regarding numerical and graphical facilities, risa will be connected to libraries that will be widely available in the future. Libraries which are connected to risa system must be open to external software just as risa itself is open to external software.

The kind of service a program module should provide and the number of functions in a program module depend on the following:

1) Software efficiency
2) Compactness and completeness of resultant software
3) Ease of software development by research groups with limited programming resources
4) Ease of combining and connecting modules developed at independent sites
5) Portability from small computers to supercomputers.

We believe that the independent open module structure concept proposed here is a good way to integrate large-scale software by collecting and combining software developed by independent contributors.

Risa itself does not have a programming environment, or graphic or numerical software; therefore, these services must be provided by other sources. Risa can serve as an algebraic computation engine if requested by other software. The use of existing, well designed software seems to be a more reasonable solution than the development of a special global software package.

The designers of most computer algebra systems have been eager to incorporate additional features. For example, numerical and graphical features, editors, two-dimensional formatters, and various kinds of input and display facilities. Because of this strategy, computer algebra systems have become enormous and prone to inflexibility when handling access requests from outside the system.

Macsyma is a computer algebra system that has a large set of symbolic, algebraic, and numerical operations. Mathematica has the 'note book', which is a kind of editor front end special to the Macintosh and NeXT computers. The note book can display high-quality three-dimensional graphics with many numerical functions.

A typical problem with these systems is that the entire *computer algebra* system must be used even when only a part of it is required. Also, the

Note: The UNIX operating system was developed and is licensed by UNIX System Laboratories, Inc.

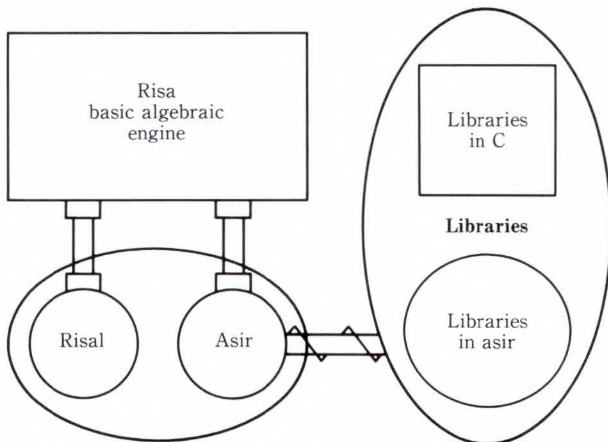

Fig. 1—Current structure of risa system.

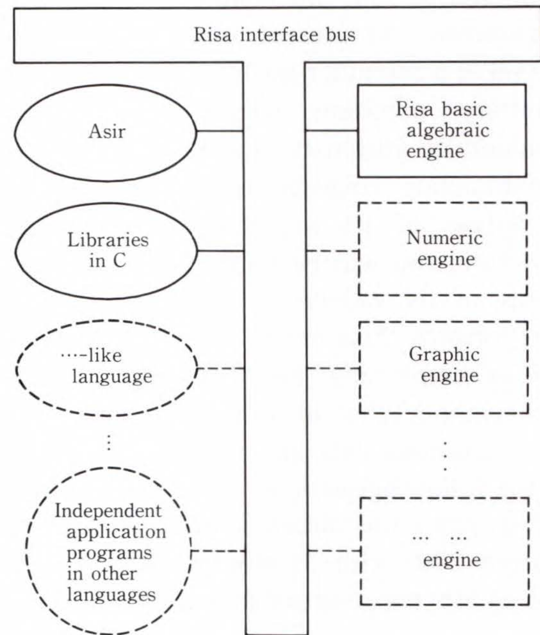

Fig. 2—Future risa system.

user may need to use the best organized existing simulation system with accuracy guaranteed, or the user may prefer an editor to that provided by the system.

2.2 Structure of the risa system

The current risa system consists of three parts (see Fig. 1):

1) Risa basic algebraic engine,
2) Risal and asir – small programming language interpreter-evaluators,
3) Libraries written in C or asir.

Basic functions whose operating speeds have a direct and significant effect on the system performance are written in C language. These C program codes (basic and general-purpose) are aggregated to an engine. Functions that are not basic but nevertheless sensitive to operating speed are also written in C language. These C program codes constitute a special purpose library in C language. Functions that are neither basic nor sensitive to operating speed are written in other programming languages, especially risal and asir.

Our independent open module structure strategy enables the use of several different engines that can be served for different objectives. Moreover, risa can be connected to more than one copy of the same engine. For such a multi-engine environment, an extension of risa that supports control protocols is now being planned.

The risa basic algebraic engine performs mainly polynomial arithmetic with rational number coefficients, and numerical and graphic engines will be incorporated in the future. The so-called parallel Risch algorithm for indefinite integration of a certain class of elementary functions is implemented as one example of a C-coded library. A library for factorization over algebraic extension fields is written in asir.

The future structure of risa will be open to many other program modules (see Fig. 2).

2.3 Running environments

Risa is being developed on the UNIX operating system, and in principle also runs on any UNIX system. The common types of machines on which risa can run include Sun3, Sun4 (Sparc), VAX with the Ultrix operating system, News, RISC News, NeXT, DecStation, and Apollo Domain.

As mentioned in Sec. 2.1, risa has neither an editing facility nor a two-dimensional printing facility. However, any popular editor (e.g. emacs or vi) can be used to code programs in asir, and any front-end input editor (e.g. fep or emacs) can be used to input asir commands. The

$\TeX$ note) style output of expressions on a screen or on paper become available if a $\TeX$ style output module is connected to the risa system.

The object size of the current risa system is about 300 Kbytes, including the risa basic algebraic engine and asir. The working memory can be expanded as required to meet the computational needs.

Risa's memory management is done using UNIX system calls for memory allocation. Risa does the following when it requires storage bytes for data:

1) Searches the free-list in the heap space for available memory.
2) If sufficient free memory is not found, invokes the garbage collection subroutine.
3) If sufficient memory bytes for the request cannot be reclaimed, issues a system call to increase the heap area.

Risa's garbage collection method follows the 'Garbage Collection in an Uncooperative Environment' by Boehm and Weiser[2]. This method is very simple and is easily incorporated into software without 'significant co-operation' from the caller. Such independence of program codes perfectly meets risa's requirements.

2.4 Portability

Most of risa is written in C language, but a very small fragment of code for long integer multiplication and division is written in assembler. This fragment is so small that its affect on the system portability is negligible. Another system dependent part is 'garbage collection codes'. This part contains several assembler codes for different hardware and, of course, depends upon standard system calls of UNIX C for memory allocation. This part also depends upon the way in which the compiler manages memory for data objects. Machine dependent codes are provided for those machines mentioned in the first paragraph of Sec. 2.3. For small computers with limited address spaces and for mainframes without linear address spaces, machine dependent codes for garbage collection are not currently available.

Note: A computer typesetting system created by Knuth[1].

However, it is not so difficult to implement garbage collectors for respective machines if their operating systems provide an environment for memory management that is similar to UNIX.

The system (hardware, operating system, and compiler) dependent property of garbage collection is the only limitation on risa's portability.

2.5 Implementation language: C vs. Lisp

General-purpose computer algebra systems used to be implemented in Lisp (e.g. Macsyma and Reduce). But recent commercially prevailing computer algebra systems (e.g. Maple and Mathematica) are written in C language or one of its relatives.

The reason for the current trend may be as follows:

1) Computer algebra systems include symbol manipulation. Initially, Lisp was the only solution for symbol manipulations that included problems such as handling variable sized structured data for symbolic expressions and dynamic memory allocation with garbage collection.
2) Because of the rapid progress in computer algebra technology, the main problems with computer algebra systems have shifted from symbol manipulation to algebraic computation.
3) Also, research and development has established a methodology for grabage collection.

Therefore, Lisp is no longer the only solution for computer algebra systems. Moreover, the following points have to be taken into accout:

1) System size

A Lisp system is usually very large; therefore, a computer algebra system constructed in Lisp is also large unless a small sized Lisp system specially designed for the computer algebra system is used. Conversely, a C implementation of a computer algebra system generates a relatively small (sometimes very small) computer algebra system.

2) Linking other systems

Because a Lisp system usually has a special

storage structure and usage, Lisp-based systems are usually subject to restrictions when linked to other software. Although most Lisp systems can be linked to other language based systems, the link is usually biased in one direction (i.e. calling from Lisp is usually well organized but calling to Lisp is often awkward and sometimes impossible). On the other hand, there are very few restrictions on accesses between C based systems and other language based systems.

3) Portability

C language is the standard system/application programming language in the UNIX environment. All UNIX systems have a C compiler. Recently, even small computers and mainframes have started to support C language. Compared to C language, Lisp has split into many dialects and cannot be a standard implementation language.

4) Accessibility to internal data structures

Some advanced users often want to know about internal data structures. In principle, this presents a problem to designers in terms of the kind of access methods that are available to users, and how convenient and efficient they are. This is not a problem of which language the system is written in. Reduce (in Lisp) opens its internal structures in detail, but Macsyma (also in Lisp) does not. Risa (in C language) opens its internal structure using primitives to access basic data structures, but Mathmatica (also in C) does not.

Risa is mainly implemented in C language to enable *independent cooperation* with other systems.

3. The risa basic algebraic engine

In the following discussion, data objects of risa are described using *tuple representation*, for example, (α, β, γ) for structures of fixed size in C language. For variable sized data, the *list representation,* denoted by $\{\alpha, \beta, ..., \gamma\}$, is used. In implementation, the latter is not necessarily stored in a usual list structure with pointer fields, but may be stored in a variable sized array.

We will use the following convention. Let α be a data object to be stored in risa, and let $\bar{\alpha}$ be the internal representation of data object α in risa.

Although these conventions give only an informal concept of data objects, this approach is sufficient to illustrate the data representation of the system.

3.1 Basic data types

3.1.1 Integers and rational numbers

In risa, the most basic mathematical data objects are rational numbers. Integers are a special kind of rational number. Integer 0 (zero) has a special form, namely, four null bytes.

Let a and b be relatively prime positive integers. Also, let σ be +1 or −1. A rational number $\sigma a/b$ is stored in the risa system as a structure of four members: ('rational', $\sigma, \tilde{a}, \tilde{b}$).

Here, $\tilde{a}$ and $\tilde{b}$ denote the representation of positive integers a and b by arrays in C language.

As in ordinary arithmetic, such potentially large positive integers are represented using a fixed positional number system. In risa, the radix B is 2^{27}. In an array, the B-ary digits of an integer are arranged so that the less significant digits occupy the smaller index positions. That is, a positive integer represented by $a = a_0 + a_1 B + \cdots + a_n B^n$ is stored in the array $\tilde{a} = \{a_0, a_1, \cdots, a_n\}$.

Integer σa is stored in the form ('rational', $\sigma, \tilde{a}, \tilde{0}$).

Do not worry about the inconsistency with the usual meaning of rational numbers as this is only a programming convention. (To be consistent with the rational number representation, the last member of the above representation should be $\tilde{1}$.)

3.1.2 Polynomials

Polynomials play a central role in risa.

There are many ways to represent polynomials in a computer. Each way has its own advantages and disadvantages. The risa basic algebraic engine uses so called *canonical recursive representation.* In this representation, a polynomial in several indeterminates is first considered as uni-variate polynomial with respect to an indeterminate with coefficients (possibly polynomials) in the remaining indeterminates.

Thus, the polynomial

$$P = a_n x^n + a_{n-1} x^{n-1} + \cdots + a_1 x + a_0,$$

in x with degree n and $a_n \neq 0$, is stored in risa using the following data structure:

('polynomial', 'x', ECPS),

where ECPS (exponent-coefficient pairs) is a list

$$\{(\overline{n}, \overline{a_n}), (\overline{n-1}, \overline{a_{n-1}}), \ldots, (\overline{1}, \overline{a_1}), (\overline{0}, \overline{a_0})\}.$$

The indeterminate x is referred to as the *main variable* of polynomial P. The coefficient a_n is referred to as the *leading coefficient* of polynomial P, and is denoted by lc(P).

In risa, if a coefficient, say a_i, is zero valued, the corresponding exponent-coefficient pair, $(\overline{i}, \overline{a_i})$, is not included in the above ECPS representation, thus saving storage space. This type of representation of polynomials is called *sparse representation.* For reasons that are complicated, the majority of computer algebra systems, risa included, use sparse representation.

A multi-variate polynomial is stored recursively so that the coefficients a_i are again polynomials. For a multi-variate polynomial P represented in such a recursive structure with respect to the ordering of indeterminates, we define the *leading number coefficient*, denoted by lnc(P), using the following recursive formula:

lnc(P) = if lc(P) is a number then lc(P) else lnc(lc(P)).

The representation of polynomial in risa is unique provided that the ordering for indeterminates appearing in the polynomial is given. This type of data representation is called *canonical* representation.

3.1.3 Rational expressions

Let A and B be polynomials that are not necessarily relatively prime. A rational expression A/B is stored in the following form:

('rational expression', $\overline{A}, \overline{B}$).

In this representation, we assume that the leading number coefficient of B, lnc(B), is positive.

Unlike the representation of polynomials and rational numbers, the representation of rational expressions in risa is not unique (i.e. not canonical). This is because we do not assume relative primeness between numerator polynomial A and denominator polynomial B. No automatic reduction is done in the risa basic algebraic engine. Reduction of common factors is determined by the user.

3.1.4 Functors and kernels

In risa, a monomial function form, such as $f(x+y)$ (i.e. a functor with one or more arguments) is called a kernel. The risa basic algebraic engine cannot distinguish kernels from ordinary indeterminates (e.g. x, y). Kernels are treated in polynomials and in rational expressions as ordinary indeterminates. That is, the risa basic algebraic engine cannot recognize kernels as objects with structures.

Therefore, the risa basic algebraic engine does not directly support the data structure of kernels or operations on kernels. Instead, such data structures and operations can be supported by programming languages. This task division frees the algebraic engine from complex data handling tasks, and allows it to concentrate on manipulating polynomials. At present, monomial function forms are fully supported by risal and partly by asir. Functors and kernels are further described in Subsec. 4.3.1.

3.2 Basic algebraic operations

3.2.1 Arithmetic of integers and rational numbers

Arithmetic operations on integers and rational numbers (fractions) are the basis of the algebraic system.

For integers represented in the above structure, addition, subtraction, multiplication, and division are rather straightforward because they can be done on the B-ary number system in a similar way as decimal arithmetic is done by hand. In particular, division of two long B-ary integers is carried out following the method shown by Knuth[3] which estimates the next digit of the quotient with at most one

Table 1. Time to compute $n!$ for several values of n

n	10	100	1 000	10 000
Time (ms)	0	10	310	47 000

Table 2. Time to compute exact division of two long integers, $(10^n)!$ and $(10^{n-1})!$

Expression	100!/10!	1 000!/100!	10 000!/1 000!
Time (ms)	0	30	4 680

Times for $(10^n)!$ and (10^{n-1}) are not included.

failure in the division[note].

Table 1 shows the computation time for $n! = 1 \times 2 \times \cdots \times n$ using a built-in function for several values of integer n. For comparison, see Tables A-1 and A-2 in Appendix A.1 which show the computation times for the same function using user-defined functions. The computation times for division of long integers are shown in Table 2.

Arithmetic operations on rational numbers (fractional arithmetic) are also straightforward, but they must be carefully carried out so that the integers in the caluclations are kept as small as possible. For this purpose, greatest common divisor (GCD) operations between two integers must be done. The greatest common divisors are used to remove, in advance, the common integer factors of the final numerator and denominator. This technique also follows the method shown by Knuth[3].

3.2.2 Arithmetic operations on polynomials, and rational expressions

Arithmetic operations on polynomials is of central importance in the risa basic algebraic engine. In some ways, arithmetic operations on univariate polynomials are similar to and sometimes simpler than operations on integers. This is because there is no need to perform *carry-over* or *borrow-from* operations among monomials of different exponents when adding or subtracting two polynomials. The calulation of powers of a polynomial can be speeded up very effectively by using *binomial coefficients* and *binomial expansion:*

Note: The possibility of a failure is extremely small.

$$(\alpha+\beta)^n = \alpha^n + \binom{n}{1}\alpha^{n-1}\beta + \cdots + \binom{n}{i}\alpha^{n-i}\beta^i + \binom{n}{n-1}\alpha\beta^{n-1} + \beta^n.$$

For powers of a multi-nomial, binomial expansion is recursively applied by partitioning the multi-nomial to nested binomials, e.g.:

$$(\alpha + \beta + \cdots + \psi + \omega) = (\alpha + (\beta + \cdots + (\psi + \omega) \cdots)).$$

For multi-variate polynomials, addition, subtraction, and multiplication can be carried out using the same procedure applied recursively with respect to thier coefficient polynomials. Division, however, is more difficult.

Let A and B be uni-variate polynomials in the same indeterminate, (e.g. x) with rational number coefficients. Dividing A by B produces the quotient Q and a remainder R such that

$$A = QB + R,$$

where Q and R are both uni-variate polynomials in x with a rational number of coefficients, and $\mathrm{degree}_x(R) < \mathrm{degree}_x(B)$. If A and/or B contain one or more extra indeterminate, recursive application of division to their coefficient polynomials leads to difficulty. Division usually produces a quotient and a remainder, but in indeterminates other than x we want to get a single polynomial for a coefficient of the quotient polynomial in x. One possible solution is to divide coefficients in rational expressions. Another way is to constrain the polynomials so that only cases in which *exact division* is possible are allowed. By '*exact division* of A by B', we mean that

$$A = QB + R,$$

holds for multi-variate polynomials A, B, Q, and R with rational number coefficients, and $\mathrm{degree}_x(R) < \mathrm{degree}_x(B)$. A third possible solution is to make a formal fraction A/B. This, however, is simply arithmetic over rational expressions.

Thus, in many ways, dividing a multi-variate polynomial by another multi-variate

Table 3. Time to compute several powers of polynomials (Unit: ms)

n	10	20	30	40	50
$(a+1)^n$	1.2	2.1	3.4	4.4	6.5
$(a+b)^n$	1.8	3.4	6.2	9.0	12
$(a+b+c)^n$	11	42	92	180	300
$(a+b+c+d)^n$	45	435	1 600	4 130	8 190
$(a+b+c+d+e)^n$	160	3 860	16 400	58 700	–

–: Running out of 64 Mbytes of virtual memory (32 Mbytes of real memory).

polynomial is not unique. The risa basic algebraic engine uses the second solution, namely exact division is supported. Other variants of divisions can be described in programming languages.

For rational expressions, arithmetic is easy unless a reduction of common factors is counted. This can be done by simply combining addition, subtraction, and multiplication of polynomials and making formal fractions from two of them. Finding the common factor between numerator and denominator completely depends on the GCD operation. This is described in the following section. Since GCD operations are expensive, the risa basic algebraic engine does not perform automatic reduction of common factors.

The computation times for several polynomial powers are shown in Table 3.

3.3 Higher algebraic operations

The risa basic algebraic engine supports GCD computation and factorization of polynomials over the rational number field. GCD computation and factorization over finite fields GF(p), where p is a prime number, are performed only internally and are not currently open for external use. Uni-variate factorization over algebraic extension fields of rational numbers is supported by an asir library.

GCD and factorization operations over different type coefficient domains mutually depend on each other. Figure 3 shows the relationship between algorithms currently used in the risa system.

3.3.1 GCD of uni-variate polynomials over the rational number field

As far as polynomial factors over the rational number field are concerned, it is sufficient to deal with polynomials with integer coefficients. Since a Euclidean algorithm for finding the GCD shows a strong intermediate coefficient swell, several improvements have been devised. Of these, the sub-resultant polynomial remainder sequence algorithm (sub-resultant PRS) family[4), 5)] and the modular GCD algorithm are dominant. Risa uses a modular GCD algorithm. Empirically, there are some cases where the sub-resultant PRS algorithm outperforms the modular algorithm. Overall performance, however, of the modular GCD algorithm is considerably higher than that of the sub-resultant PRS algorithm.

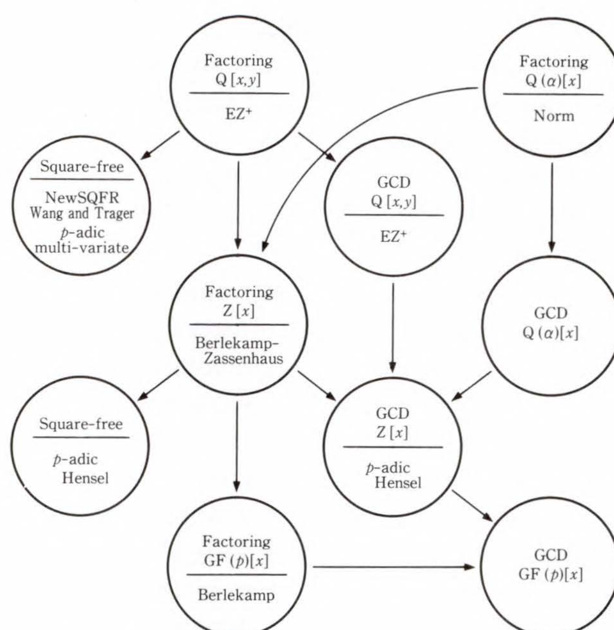

Fig. 3–Relationship between factoring and GCD algorithm in risa system.

Modular algorithms are frequently and commonly used in calculations of polynomials with very large coefficients.

The essence of a modular algorithm is to convert the original problem into its counterpart in a coefficient domain in which computation can be easily performed. For a GCD computation, integer coefficients are projected onto one or more finite fields, particularly onto Galois field GF(p) for several prime integers p. Then, computation of the desired objects (e.g. factors) is performed over such simple domains. Arithmetic operations on polynomials can be performed very quickly in GF(p) without an intermediate coefficient swell. Finally, the

images of the desired objects in the projected domain(s) are projected back into their integer counterparts by using a *Chinese remainder algorithm*[6] or *Hensel lifting*.

Details on the *Chinese remainder algorithm* and *Hensel lifting* can be found in the references of this article[3), 7), 8)].

3.3.2 Factorization of uni-variate polynomials over the integer domain

Factoring uni-variate polynomials over the integer domain is a very attractive problem. It is reported[3] that the astronomer Friedrich von Schubert devised an algorithm to find all factors of a uni-variate polynomial over the integer domain. It is also reported[3] that about 90 years later L. Kronecker rediscovered von Schubert's algorithm. Unfortunately, this algorithm is very inefficient when the degree of a polynomial is greater than five.

Modern algorithms for factoring polynomials have their origin in E.R. Berlekamp's paper[9], which presents a factoring algorithm over finite fields. H. Zassenhaus[10] devised an algorithm which finds factors over the integer domain. Many improved algorithms and subalgorithms based on the above have since been proposed. Risa implements our own improvements of some of these algorithms.

We will now explain the meaning of the term *square-free*. A polynomial $f(x)$ is *square-free* if it has no multiple factors.

Factorization of a uni-variate polynomial in risa is done in three major steps:

1) Square-free

Extract the square-free components of the polynomial and their multiplicities so that the next steps are effective.

2) Factoring over GF(p)

Factor out the given square-free polynomial into its irreducible factors over finite field GF(p) for several small primes p.

3) Lifting up and finding the true factors

Lift the candidate factors, then test each of them for a true factor by trial division over the integer domain.

For the first step, risa uses a p-adic Hensel-type algorithm, which is mentioned but not explicitly described by P.S. Wang and B.M. Trager[11].

The algorithm is based on correct image factors over GF(p) for a large prime p. Then, the images, i.e. square-free factors over GF(p) for prime p, are lifted in parallel using a modified Hensel-type algorithm.

This algorithm makes factorization in the risa basic algebraic engine of uni-variate polynomials over the integer domain very fast.

The second step follows Berlekamp's algorithm. A problem with this step is that there is no assurance of obtaining lucky primes that yield correct images over GF(p). So, in general, we cannot assure that a factor over GF(p) is a correct image of a true factor over the integer domain.

We therefore need a third step to verify the correctness. Several combinations of image factors have to be tried and lifted until a true factor is found. In the worst case, the required number of trials of such a verification procedure is exponentially proportional to the degree of the polynomial to be factored. There are an infinite number of examples where an irreducible polynomial over the integer domain splits into at most quadratic factors over GF(p) for every prime p[12].

A.K. Lenstra, H.W. Lenstra, and L. Lovasz[13] presented an algorithm – Basis reduction algorithm in a lattice – which factors a uni-variate polynomial within polynomial time with respect to the degree of the polynomial. The key idea is that a lattice point with a *small norm* in the lattice generated from the polynomial to be factored corresponds to a true irreducible factor.

Theoretically, the lattice algorithm is currently the best algorithm for the worst case. In practice, however, the trial-and-verify method is faster in most cases. As was shown by Yokoyama and Takeshima[14], an extension of the lattice algorithm can be applied to certain Euclidean rings. Abbott et al.[12] employed the algorithm to factorize uni-variate polynomials over algebraic extension fields, which shows its effectiveness in extremely ill-conditioned cases (see also Sec. 5.1).

The lattice algorithm is not currently

Table 4. Time to factor uni-variate polynomials

Poly-nomial	$(2x)^{20}+1$	$(2x)^{40}+1$	$(2x)^{60}+1$	$(2x)^{80}+1$	$(2x)^{100}+1$
Time (ms)	260	11 580	37 390	38 000	18 010

Table 5. Time to factor uni-variate polynomials (Polynomials are given in Appendix B.1)

Poly-nomial	u_1	u_2	u_3	u_4	u_5	u_6	u_7	u_8
Time (ms)	3 490	450	430	650	210	550	690	2 020

implemented in the risa basic algebraic engine.

Tables 4 and 5 show the time required to factor uni-variate polynomials.

3.3.3 GCD computation and factorization of multi-variate polynomials over the integer domain

For a multi-variate polynomial, the risa basic algebraic engine essentially uses an EZ algorithm by Moses and Yun[15], and by Wang and Rothschild[16] that has been improved by M. Noro et al.[17]. The improved algorithm can be regarded as a simplified version of Wang's EEZ algorithm[18].

PRS algorithms are also applicable for multivariate GCD computation; see Hearn[19], Brown[20], and Suzuki and Sasaki[21]. Modular algorithms of the Chinese remainder type, e.g. Brown[5] and Collins[22], are more suitable than PRS algorithms, especially for dense multi-variate polynomials. On the other hand, Hensel type (EZ and EEZ) algorithms are considered best for sparse multi-variate polynomials. Since, in practice, most multi-variate polynomials dealt with are sparse, Hensel type algorithms are most practical.

The EZ algorithm reduces the multi-variate polynomial problem of GCD and factorization into a uni-variate polynomial problem by substituting indeterminates with integers. This substitution is called evaluation, and the substituted integer value is called an evaluation point. The evaluation can only be done under several constraints. One important constraint is that the evaluation must preserve the square-free property of the given multi-variate polynomial after evaluation. The true multi-variate factors are reconstructed by an extended Zassenhaus algorithm (i.e. an extension of p-adic Hensel lifting).

Using the EZ algorithm for multivariate GCD and factorization has three major problems: the leading coefficient, extraneous image factor, and bad zero substitution.

The enhanced EZ algorithm (EEZ algorithm) offers practical improvements in these areas. The main improvement is predetermination of the leading coefficients of the factors. Also, because the improved p-adic construction procedure (parallel lifting of all factors) conserves the sparsity of multi-variate polynomials, the bad zero substitution problem is solved. This solution considerably reduces the extraneous factor problem by using several different sets of integers to factor a uni-variate polynomial over the integer domain. The existence of an evaluation which meets the constraints of the algorithm has not been proved. However, such an unlucky case is considered to be very rare, and the theoretical drawback does not affect the effectiveness of the EEZ algorithm.

The risa basic algebraic engine does not yet support the EEZ algorithm, partly because the algorithm is extremely complicated and requires very careful coding. Another reason is that we have devised an improved EZ algorithm, that can be regarded as a simplified EEZ algorithm. This improved algorithm is briefly explained below.

When a uni-variate factor and its co-factor are lifted using the EZ algorithm, their leading coefficients have to be tentatively predetermined. The simplest way to do this is to provide the leading coefficient of the given polynomial. However, this method is very inefficient because the number of lifting steps increases if the total degree of the leading coefficient is large. As for GCD, an estimation of the leading coefficients of GCD can be obtained by obtaining the GCD of the two leading coefficients of the polynomials. Obviously, this method cannot be applied to factorization. The EEZ method completely predetermines the leading coefficients from the factors of the leading coefficient. Our

Table 6. Time to factor multi-variate polynomials (Polynomials are given in Appendix B.2)

Poly-nomial	m_1	m_2	m_3	m_4	m_5	m_6	m_7	m_8
Time (ms)	170	130	190	2 260	1 400	3 550	110	16 700

Poly-nomial	m_9	m_{10}	m_{11}	m_{12}	m_{13}	m_{14}	m_{15}
Time (ms)	7 700	4 020	7 380	20	1 350	480	450

Table 7. Time to factor multi-variate polynomials (Polynomials are given in Appendix B.2)

Polyno-mial	d_2	d_3	d_4	d_5	d_6	d_7	d_8	d_9	d_{10}
Time (ms)	10	20	30	250	290	370	1 140	2 310	14 840

Table 8. Time to factor multi-variate polynomials (Polynomials are given in Appendix B.2)

Polynomial	s_1	s_2	s_3	s_4	s_5	s_6
Time (ms)	40	310	180	2 000	4 240	6 690

technique is to evaluate the factors of the leading coefficient in order to estimate the leading coefficients of factors. In more detail, evaluation points are chosen so that the factors of the leading coefficient at the evaluation points do not divide each other. The leading coefficients of factors can be estimated by counting the mutual divisibilities of the integers obtained by the evaluation.

The existence of such an evaluation that meets the above condition and also preserves the square-free property of the given square-free polynomial has not been proved. Therefore, our technique is as heuristic as the EEZ algorithm.

Examples of times required to factorize multi-variate polynomials over the integer domain are shown in Tables 6 to 8.

4. Asir — a programming language

The separation of programming languages from computation engines is a consequence of our independent open module strategy. We have already implemented two language prototypes: *asir* and *risal*. Risal has more data types than asir and is implemented without counting efficiency. Asir allows limited data types and its interpreter/evaluator is more efficient. Asir's syntax is essentially the syntax of C language.

Our experiences in developing two language prototypes have shown the advantages of separating engines and languages. It will not be difficult to implement programming languages having a syntax similar to such languages as FORTRAN, Algol, Pascal, and BASIC according to the users' preference.

In the following section we describe the asir language, which we regard as a standard language prototype. (We will enhance and improve asir in the future.)

4.1 Overview of asir

Asir was developed as a simple but efficient user programming language to interface between users and the risa basic algebraic engine. Higher level programming features are studied by developing risal, asir's elder brother. Asir was carefully designed so that it will not be subject to major changes in its programming features in the future. In many ways, this careful but rather awkward strategy has made asir immature. However, asir is still under development and is growing steadily.

Asir's interpreter/evaluator is written in C language. The use of a C preprocessor in the parsing process of the asir interpreter makes it easier to define macros, aliases, etc. Asir's parser generates a program tree that can be subsequently interpreted and evaluated. Asir's interpreter/evaluator interprets programs and dispatches primitive jobs to the risa basic algebraic engine. A list of indeterminates that sometimes includes kernels is sent to the engine together with the data. This list shows the ordering of indeterminates in the data.

Asir Version 0 supports the following functions:

1) Arithmetic operations on integers, rational numbers, polynomials, and rational expressions
2) Primitive operations for vectors and matrices
3) Minimum list processing features
4) A C-like programming language

5) Several built-in functions/operations
6) A dbx-like debugger.

4.2 Syntax of asir

The asir syntax is based on C language. The major differences between the two are explained below.

Limitations

1) Asir has no types for program variables or indeterminates; therefore, types cannot currently be defined.
2) Program variables declared in a function are local to the function by default. If program variables in a function are declared 'external', they are global at the top level.
3) A program variable begins with a capital letter. Indeterminates and functions begin with a lower-case letter.
4) 'switch statements' and 'goto statements' are not allowed.
5) 'Comma expressions' are allowed for A, B, and C in 'for (A; B; C)' or for A in 'while (A)'.

Extensions

1) Computations on rational expressions and polynomials are supported.
2) Lists can be processed.

4.3 Compound data types and operations

4.3.1 Functors and kernels

Functors are function symbols of kernels (monomial function forms). For example, kernels $\sin(x)$ and $f(xy, x - y)$ have functors sin and f respectively. Syntactically, functors are indistinguishable from ordinary functions, but they remain in the results after evaluation, whereas ordinary functions do not. In usual arithmetic, kernels are treated as unstructured objects; therefore, the risa basic algebraic engine does not recognize their structures. For example, $\sin(x)$ is treated as a single indeterminate independent and distinct from any other indeterminates and kernels. Typical operations that recognize the structural composition of kernels are differentiation and integration. These operations depend upon the actual arguments of a kernel as well as its functor. At present, operations for functors and kernels are only experimental and are insufficient to support computations by rewriting rules.

4.3.2 Lists

Lists are supported in asir. A list having elements $\alpha_1, \alpha_2, \cdots, \alpha_k$ is denoted in asir by $[\alpha_1, \alpha_2, \cdots, \alpha_k]$. A null list (list having no member) is denoted by [ ].

Five primitive operations on lists are supported:

1) $[\alpha_1, \alpha_2, \cdots, \alpha_k]$: generates a list.
2) car(L): gives the first element of non-null list L.
3) cdr(L): gives the list obtained by removing the first element of non-null list L.
4) cons(H, T): gives a new list L such that car(L) = H and cdr(L) = T.
5) '==': equality test for lists.

4.3.3 Vectors and matrices

Vectors and matrices are supported in asir with their primitive operations, i.e. addition, subtraction, multiplication, scalar multiplication, and scalar division. Exponentiation by a positive integer is allowed for rectangular matrices. Subsequently, operator symbols +, –, *, /, and ^ are polymorphic operators. Such polymorphic operators are interpreted according to the data types of their operands at evaluation.

More complicated operations, such as inversion of matrices, are not currently supported. Because these more complicated operations tend to explode unless carefully designed algorithms are used, they will be supplied by libraries.

Asir does not currently support arrays. Elements of a vector or matrix can be of any type. This somewhat alleviates the inconvenience caused by the absence of arrays.

An element designator of a vector or matrix is treated as one programming variable. Therefore, it can appear at the left side of assignment statements.

4.4 Built-in functions

This section explains several built-in functions that are not mentioned elsewhere.

The meanings of arguments in this section are as follows:

obj	: arbitrary
rat, rat_n	: rational expression
$poly, poly_n, defpoly$	: polynomial
var	: indeterminate
list	: list
vect	: vector
mat	: matrix
int, *deg*, *len*	: integer.

1) Manipulation of objects

var(*rat*)	: main-variable of *rat*
vars(*rat*)	: list of indeterminates contained in *rat*
red(*rat*)	: reduced rational expression of *rat*
nm(*rat*)	: numerator of *rat*
dn(*rat*)	: denominator of *rat*
coef(*poly*, *deg*, *var*)	: coefficient of *poly* at degree *deg* with respect to *var*
deg(*poly*, *var*)	: highest exponent of *poly* with respect to *var*
size(*vect*), size(*mat*)	: [length of *vect*], [row size of *mat*, column size of *mat*]
type(*obj*)	: type classifier of *obj*

2) Mathematical operations

fac(*int*)	: factorial of *int*
gcd($poly_1, poly_2$)	: GCD of $poly_1$ and $poly_2$
agcd($defpoly, poly_1, poly_2$)	: GCD of $poly_1$ and $poly_2$ over an algebraic extension field with its defining polynomial *defpoly*
subst(rat_1, [var, rat_2]*)	: substitute rat_2 for *var* in rat_1; left to right if repeated
res($var, poly_1, poly_2$)	: resultant of $poly_1$, and $poly_2$ with respect to *var*
fctr(*poly*)	: factorize *poly*; result is a list of form [[$multiplicity_1, factor_1$], ...]
afctr(*defpoly*, *poly*)	: factorize *poly* over algebraic extension field with defining polynomial *defpoly*
diff(*rat*, *var*)	: differentiate *rat* by *var*
int(*rat*, *var*)	: integrate *rat* by *var*; loading integration library is necessary

3) Special divisions

sdiv($poly_1, poly_2$) : exact division giving quotient

srem($poly_1, poly_2$) : exact division giving remainder

idiv(int_1, int_2) : integer quotient

irem(int_1, int_2) : integer remainder

4) Miscellaneous

newvect(*len*) : generate a new vector with length *len*

newmat(*row*, *col*) : generate a new matrix with row size *row* and column size *col*

print(*obj*) : display *obj* followed by a newline

cputime(0 or 1) : enter displaying mode of CPU-time if argument is 1; exit if argument is 0

debug : enter 'debugging mode'

load("*filename*") : read programs from file *filename*; object files (relocatable object codes generated by C compiler) can also be read

end, quit : close the current reading file; close asir session at the top level

4.5 User defined functions

The user can define functions by using the 'def' statement. Many syntax errors may be detected at parsing. These errors are indicated by their approximate position in the reading file. A function is distinguished by its name regardless of the number of arguments it contains. If the same name functions are defined more than once, only the last one is valid for that name.

Appendices A.1 and A.2 show example programs and the timing data.

4.6 Asir debugger

Asir has its own dbx-like debugger[note]. To enter debugging mode, type-in 'debug'; at the top level. Asir also enters debugging mode when it reaches a break point, or when the 'd' option is selected at interruption.

The debugger has a minimum set of dbx commands. Their functions are mostly similar to those of dbx commands. Execution of asir statements is controlled by several commands, some of which are shown below.

1) 'step' and 'next' execute the next statement.
2) 'stop at' sets a break point on the source line.
3) 'delete' removes a break point.
4) 'print' displays the value of an expression.
5) 'cont' lets asir exit from debugging mode and continue asir evaluation.
6) 'list' displays source lines.
7) 'quit' lets asir exit from debugging mode.

Note: dbx is a standard symbolic debugger of BSD UNIX.

5. Libraries

5.1 Factorization over algebraic extension fields

Factorization using *norm* is experimentally implemented in asir. Factorization was first written in C language as a sub-module of the risa basic algebraic engine. Because of our policy, this type of non-general routine was rewritten in asir language. No reduction in efficiency was found after rewriting.

Some literature states that the norm method is inefficient compared to methods that use

Hensel lifting. Abott et al.[12] reported several exceptionally ill-conditioned cases in which lattice methods seem to be the only practical solution. Our experience shows that norm methods using our improvements are practicable for not only usual cases but also for some ill-conditioned cases.

In the discussion below, we will use the following notation: $\mathbb{Z}$ for the set of integers; $\mathbb{Q}$ for the set of rational numbers.

Let α be algebraic over $\mathbb{Q}$ with its minimal polynomial $g(t)$. Let $\mathbb{Q}(\alpha)$ denote an algebraically extended field of $\mathbb{Q}$ by adjoining α to $\mathbb{Q}$. The problem is to factorize $f(x) \in \mathbb{Q}(\alpha)[x]$ over $\mathbb{Q}(\alpha)$.

The original algorithm does the following:

Step 1: Let $r(x) = \text{resultant}_t(f(x - st),\ g(t))$ for an integer s. Search for a square-free $r(x)$ for s.

Step 2: Factorize a square-free $r(x)$ over $\mathbb{Q}$. Let $h(x)$ be one of the irreducible factors.

Step 3: Let $k(x) = \text{GCD}(h(x + s\alpha),\ f(x))$ over $\mathbb{Q}(\alpha)$, where $k(x)$ is an irreducible factor of $f(x)$ over $\mathbb{Q}(\alpha)$. *Here, we can use any algorithm to compute a uni-variate GCD over* $\mathbb{Q}(\alpha)$.

The polynomial $r(x)$ in Step 1 is identical to what we call the *norm* of $f(x - s\alpha)$ from $\mathbb{Q}(\alpha)[x]$ onto $\mathbb{Q}(x)$.

Our improvements are as followings:

1) Computation of the resultant in the original algorithm, Step 1, takes considerable time. Therefore, let us consider to make use of the non-square-free $r(x)$. $r(x)$ contains all facors of $f(x - s\alpha)$. Therefore, in the original algorithm steps, any factor of such an $r(x)$ produce a non-trivial factor of $f(x)$. Although the obtained factors are not guaranteed to be irreducible over $\mathbb{Q}(\alpha)$, a reduction in the size of the problem can be expected.
2) Further observation tells us that for factors of single multiplicity, GCD in Step 3 is irreducible. Thus, $r(x)$ can be used independently from its square-free property.
3) A candidate factor of uni-variate factorization in Step 2 is determined to be extraneous if its degree is not a multiple of the degree of $g(t)$. This is because an irreducible factor, say $h(x)$, of a square-free part of $r(x)$ over $\mathbb{Z}$ is a product of all conjugates of an irreducible factor of $f(x - s\alpha)$ over $\mathbb{Q}(\alpha)$.

   Therefore, the degree of $h(x)$ must be divided by the degree of $g(t)$.

Table 9. Time to factor uni-variate polinomials $f(x)$ over algebraic extension fields $\mathbb{Q}(\alpha)$, where α is a root of each $f(x)$ to be factored
(Polynomials are given in Appendix B.3)

Polynomial	a_1	a_2	a_3	a_4	a_5	a_6	a_7	a_8
Time (ms)	70	80	470	4 100	22 430	3 040	60	20

These improvements enable the efficient factorization of many problems that are extremely ill-conditioned for the original algorithm. The timing data is shown in Table 9.

5.2 Indefinite integration

An incomplete version of indefinite integration of some limited elementary functions is experimentally implemented in C language. This could be implemented in asir in the same way that the routine for uni-variate factorization over algebraic extension fields was implemented. The rewriting of this implementation in asir, and the improvement of its applicability to a wider range of elementary functions are left for the future.

For rational functions, Rothstein's algorithm[23] (some literature refers to it as Trager-Rothstein's algorithm) is employed. The integration of rational functions involves two steps: computation of the rational part of the integral, and computation of the logarithmic part of the integral.

Rothstein's algorithm[23] and Trager's algorithm[24] find the rational part in the same way. But to compute the logarithmic part, the former only needs to perform GCD computations on several algebraic extension fields, whereas the latter must compute a sufficiently large extension field of the integrand's denominator (in the worst case, the splitting field). Computing the splitting field of a polynomial is very hard if the degree of the polynomial is five or more. Thus, Rothstein's algorithm is much more efficient than Trager's algorithm.

For transcedental extension of rational functions, the so-called *parallel Risch algrithm* is implemented for logarithmic extension and exponential extension. The implemention is incomplete in many ways. This is because only two transcendentals, *log* and *exp*, are supported; and because denominators are factorized only over the rational number and not in algebraic closures. (This is true for almost all computer algebra systems because multi-variate factorization over algebraically closed fields is highly expensive.) Also, no check is made regarding conformity to monomial extensions, which is a necessary condition for the algorithms.

Integration of algebraically extended functions are not currently implemented. Thus, our implementation is only experimental, and in many ways is incomplete. Enhancement of our implementation is left for the future.

6. Other features

6.1 Floating-point number coefficients

Floating-point number coefficients are experimentally implemented in the risa basic algebraic engine. Asir supports the writing of floating-point number constants in asir programs. Many computer algebra systems support arbitrary precision floating-point numbers, the so-called *big float*. In risa, however, only double precision floating-point numbers are available. Arithmetic operations between floating-point and rational numbers result in a floating number. Other operations that involve floating coefficients are not defined in risa. Factorization, of course, cannot be well-defined in a normal sense. GCD and resultant operations can apparently be defined. Doing such algebraic operations using approximate numbers (i.e. floating numbers) can easily produce incorrect results. Recently, approximate algebraic computations' have been proposed by Sasaki and Noda[25], Sasaki and Sasaki[26], and Noda et al.[27] that partly show how to extend algebraic operations and algorithms to numerical computation.

6.2 Graph plotting

By using the X11[note)] interface technology, a small sample program for writing implicit curves in two-dimensional space was recently incorporated into the risa basic algebraic engine. Numeric evaluation of a given polynomial in two indeterminates can be performed by several different CPUs. To specify such a distributed computation, several primitive functions are supported as asir functions. Displaying windows, of course, can be specified, and this will be enhanced into a practical graph plotting module.

7. Theoretical contributions

This chapter briefly describes our theoretical contributions to computer algebra research. The results of these theoretical contributions will form the foundation of future enhanced risa systems.

The first section discusses our studies on polynomial factorization and shows several new methods of factorization for several domains.

7.1 Factoring uni-variate polynomials over finite fields[28)]

This section describes our work on the factorization of uni-variate polynomials over finite fields. To factor a given polynomial $f(x)$ over $GF(q)$, we enhanced the following sub-algorithms of Berlekamp's factorization algorithm for uni-variate polynomials over finite fields: distinct degree decomposition and the finding of non-trivial factors.

We introduced three new sub-algorithms:

1) Determination of distinct degree factors in advance by using the concept of p-factors,
2) test of separability for an arbitrary non-trivial element $g(x)$ in Kernel $(\Pi - I)$, where Π is the Frobenius mapping on $GF(q)[x]/(f(x))$ and I is the identity mapping, and
3) setting an alternative for 'finding root', that is, 'finding non-trivial factors of $G(x)$, i.e. the minimal polynomial of g' instead of 'finding roots of $G(x)$'.

The first sub-algorithm speeds up the GCD

Note: X Window System, Version 11; The X Window System is a network transparent window system developed at MIT. It runs on a wide range of computing and graphics machines.

computation because the degree of the resultant factor is known in advance. The test of separability determines how many irreducible factors are contained in GCD($f, g - s$), where s is a root of $G(x)$. In addition, this test gives non-trivial factors without the need to use the 'finding roots' procedure even if GCD($f, g - s$) fails to produce an irreducible factor.

7.2 Factoring multi-variate polynomials over algebraic extension fields[29),30)]

Kaltofen devised a way to find an extension field over which an absolutely irreducible factor can be obtained[31),32)]. He employed an analytic argument to prove his answer. We developed an alternative algebraic proof of Kaltofen's answer, and used the proof to devise several extensions to his answer and to investigate the properties of absolutely irreducible factors. We also showed how our results can be used to computate absolutely irreducible factors. {Independently, Chistov and Grigor'ev also gave a similar alternative proof of Kaltofen's answer[33)].}

In connection with our work on the factorization of polynomials, we also looked for a way to represent extension fields and to determine the solvability of polynomials.

7.3 Representation of extension fields, primitive elements[34)]

Computer algebra often involves algebraic extension fields, especially in the problems on polynomial factorization that were discussed in the previous two sections. We presented several mathematical results and new computational methods for primitive elements and their minimal polynomials. In more detail, for a field $\mathbb{Q}(\alpha_1, \ldots, \alpha_t)$ obtained by adjoining algebraic numbers $\alpha_1, \ldots, \alpha_t$ to the rational number field $\mathbb{Q}$, we showed that there is at least one vector $\bar{s} = (s_1, \ldots, s_t)$ of integers in distinct tN integers such that

$$s_1\alpha_1 + s_2\alpha_2 + \ldots + s_t\alpha_t$$

is a primitive element, where N is the degree of $\mathbb{Q}(\alpha_1, \ldots, \alpha_t)$ over $\mathbb{Q}$. Moreover we presented a method of directly calculating a vector $\bar{s}$ such that

$$s_1\alpha_1 + s_2\alpha_2 + \ldots + s_t\alpha_t$$

is a primitive element. For a given polynomial f over $\mathbb{Q}$, we presented methods of computing a primitive element of the splitting field of f over $\mathbb{Q}$. We also presented methods of computing a primitive element of the splitting field of f and its minimal polynomial over $\mathbb{Q}$.

7.4 Solvability of polynomials[35)]

Landau and Miller[36)] presented a method of determining the solvability of a monic irreducible polynomial over the integer domain in polynomial time. In their method, a series of polynomials is constructed so that the original problem is reduced to determining the solvability of new polynomials. We presented a more efficient method of finding such a series of polynomials. More precisely, we introduced the new notion of a series of blocks in the set of all roots of the original polynomial under the action of its Galois group. We then presented an efficient method of finding such a series of blocks by modifying Landau and Miller's method of finding minimal non-primitive blocks.

As for higher arithmetics, we studied how to deal with polynomial ideals and their related problems, for example, computing the Gröbner basis and solving polynomial equations using the Gröbner basis.

7.5 Modular Gröbner basis[37)]

First we will describe our work on computing the Gröbner basis. Sasaki and one of the authors proposed a new method of constructing the Gröbner basis of a polynomial ideal over $\mathbb{Q}$ that uses a modular approach. Given a finite set of polynomials in $\mathbb{Z}[x_1, \ldots, x_n]$, this method calculates the Gröbner bases over $\mathbb{Z}/(p_i)$, $i = 1, \ldots, k$, where $p_1, \ldots, p_k$ are distinct primes. Then, it constructs the Gröbner basis over $\mathbb{Q}$ by using the Chinese remainder algorithm and conversion of integers to rationals. We therefore called the method the *modular Gröbner method* or *modular Buchberger algorithm*. By avoiding intermediate coefficient growth, this method enables the efficient calculation of a Gröbner basis with large-sized coefficients. We proposed two algorithms, one is simple but probabilistic in that it may give a wrong basis such that

ideal(*wrong basis*) ⊃ ideal(*true bais*) with an extremely small possibility. The other algorithm is less simple but gives the correct basis. (As a related topic, solving a system of algebraic equations using the modular Gröbner method is also discussed.)

Next, we will mention our work on solving polynomial equations.

7.6 Solving polynomial equations[38),39)]

We presented some new mathematical results and proposed several new algorithms for solving a system of algebraic equations algebraically. In this work, we found that many ideal theoretical arguments for the problem can be translated into their counterparts in the theory of linear maps. This translation provided straightforward descriptions of the *U*-resultant and the forms of solutions of systems. Our new algorithms apply algorithms for linear algebra to avoid repeated computations of Gröbner bases under lexicographic order. In principle, these algorithms require only one computation of a Gröbner base under an arbitrary order.

8. Conclusion

This paper discussed some of the results of research in computer algebra. A small but rigorous computer algebra system, *risa*, was introduced. Risa is envisioned as an indispensable component of *future scientific computation systems*. It is mainly intended for professional use in very large and time consuming computations, but is also usable by non-professionals. Risa is based on the mathematical foundations of computer algebra and the *independent open module structure*. As a general purpose computer algebra system, risa's operating speed is competitive and in some cases outstanding.

The next main target of our research is to connect risa to a numeric package, for example, Fujitsu's SSL II. A Gröbner-basis library is also included in our plans. The numeric/algebraic hybridization of algorithmic levels is a challenging and valuable research theme.

Appendices

A. Sample programs

A.1 Programs for calculating factorials

1) /* A recursive program for factorials. */
```
def recf(X) {return !X ? 1 : X * recf(X-1);}
```
(see Table A-1.)

2) /* A repetitive program for factorials. */
```
def f(X) {
for (I = 1, M = 1; I <= X; I++) M *= I;
return M;
}
```
(see Table A-2.)

Table A-1. Time to compute $n!$ using the above recursive program, recf(n), for several values of n

n	10	100	1 000	100 000
Time (ms)	5	30	1 150	126 520

Table A-2. Time to compute $n!$ using the above repetitive program, f(n), for several values of n

n	10	100	1 000	100 000
Time (ms)	5	25	940	105 820

A.2 A program for calculating π

1)
```
def at1(M, D) {
for (N = 1, SGN = 1, MM = M*M, A = 0,
    XN = idiv(D, M); XN;
    N += 2, XN = idiv(XN, MM), SGN *= -1)
A += (SGN*idiv(XN, N));
return A;
}

def pi(D) {
Y = 10^D; X = 16*at1(5, Y)-4*at1(239, Y);
return X;
}
```
(see Table A-3.)

Table A-3. Time to compute first n digits of π using the above program, pi(n), for several values of n

n	10	100	1 000	100 000
Time (ms)	10	50	2 065	185 835

B. Data for timing table

B.1 Data for uni-variate factorization

$$u_1 = (8192x^{10} + 20480x^9 + 58368x^8 - 161792x^7 + 198656x^6 + 199680x^5 - 414848x^4 - 4160x^3 + 171816x^2 - 48556x + 469)(8192x^{10} + 12288x^9 + 66560x^8 - 22528x^7 - 138240x^6 + 572928x^5 - 90496x^4 - 356032x^3 + 113032x^2 + 23420x - 8179) \times (4096x^{10} + 8192x^9 + 1600x^8 - 20608x^7 + 20032x^6 + 87360x^5 - 105904x^4 + 18544x^3 + 11888x^2 - 3416x + 1)(4096x^{10} + 8192x^9 - 3008x^8 - 30848x^7 + 21056x^6 + 146496x^5 - 221360x^4 + 1232x^3 + 144464x^2 - 78488x + 11993).$$

[u_1 : from SIGSAM Problem 7]

$$u_2 = x^{25} - 25x^{20} - 3500x^{15} - 57500x^{10} + 21875x^5 - 3125.$$

$$u_3 = x^{18} + 9x^{17} + 45x^{16} + 126x^{15} + 189x^{14} + 27x^{13} - 540x^{12} - 1215x^{11} + 1377x^{10} + 15444x^9 + 46899x^8 + 90153x^7 + 133893x^6 + 125388x^5 + 29160x^4 - 32076x^3 + 26244x^2 - 8748x + 2916.$$

$$u_4 = (x^{16} + 4x^{12} - 16x^{11} + 80x^9 + 2x^8 + 160x^7 + 128x^6 - 160x^5 + 28x^4 - 48x^3 + 128x^2 - 16x + 1)(x^{16} + 4x^{12} + 16x^{11} - 80x^9 + 2x^8 - 160x^7 + 128x^6 + 160x^5 + 28x^4 + 48x^3 + 128x^2 + 16x + 1).$$

$$u_5 = (x^4 + 351x^3 + 27x^2 - 31x + 1)^2(6x^5 + 251x^3 - 372x^2 + 15x - 323)^6.$$

$$u_6 = (x^4 + 351x^3 + 27x^2 - 31x + 1)^3(6x^5 + 251x^3 - 372x^2 + 15x - 323)^9.$$

$$u_7 = (x^3 + 75x^2 + 68x + 1)^3(x^2 + 15x + 35)^6(7x^2 + 750x + 137)^9(x + 75)^{12}.$$

$$u_8 = (x^3 + 75x^2 + 68x + 1)^5(x^2 + 15x + 35)^{10}(7x^2 + 750x + 137)^{15}(x + 75)^{20}.$$

[u_2-u_8 : from Wang-Trager[11)]]

B.2 Data for multi-variate factorization

$$m_1 = (xy + z + 10)(xz + y + 30)(x + yz + 20).$$

$$m_2 = (x^3(z + y) + z - 11)(x^2(z^2 + y^2) + y + 90).$$

$$m_3 = (x^3y^2 + xz^4 + x + z)(x^3 + xyz + y^2 + yz^3).$$

$$m_4 = (x^2z + y^4z^2 + 5)(xy^3 + z^2)(-x^3y + z^2 + 3)(x^3y^4 + z^2).$$

$$m_5 = (3u^2x^3y^4z + xz^2 + y^2z^2 + 19y^2)(u^2y^4z^2 + x^2z + 5)(u^2 + x^3y^4 + z^2).$$

$$m_6 = (w^4z^6 - w^3x^3y - w^2x^2y^2z^2 + x^5z - x^4y^2 + y^2z^3)(-x^5z^3 + x^2y^3 + yz) \times (w^4x^5y^6 - w^4z^3 + w^2x^3y + xy^2z^2).$$

$$m_7 = (x + y + z - 2)^2(x + y + z - 3)^3.$$

$$m_8 = (-z^{31} - w^{12}z^{20} + y^{18} - y^{14} + x^2y^2 + x^{21} + w^2)(-15y^2z^{16} + 29w^4x^{12}z^3 + 21x^3z^2 + 3w^{15}y^{20}).$$

$$m_9 = u^4xz^2(18u^2w^3xz^2 + 10u^2wxy^3 + 15uz^2 + 6w^2y^3z^2)(25u^2w^3yz^4 + 32u^2w^4y^4z^3 - 48u^2x^2y^3z^3 - 2u^2wx^2y^2 + 44uwxy^4z^4 - 8uwx^3z^4 + 4w^2x + 11w^2x^3y + 12y^3z^2).$$

$$m_{10} = (31u^2xz + 35w^2y^2 + 40wx^2 + 6xy)(42u^2w^2y^2 + 47u^2w^2z + 22u^2w^2 + 9u^2wx^2 + 21u^2wxyz + 37u^2y^2z + u^2w^2xy^2z^2 + 8u^2w^2z^2 + 24u^2wxy^2z^2 + 24u^2x^2yz^2 + 12u^2xy^2z^2 + 13uw^2x^2y^2 + 27uw^2x^2y + 39uwxz + 43ux^2y + 44uw^2z^2 + 37w^2xy + 29w^2y^2 + 31w^2yz^2 + 12wx^2yz + 43wxyz^2 + 22xy^2 + 23xyz + 24xy + 41y^2z).$$

$$m_{11} = (13u^3w^2xyz^3 - 4uxy^2 - w^3z^3 - 47xy)(-36u^2w^3xyz^3 - 31u^2w^3y^2 + 20u^2w^2x^2y^2z^2 - 36u^2wxy^3z + 46u^2wx + 9u^2y^2 - 36uw^2y^3 + 9uwy^3 - 5uwx^2y^3 + 48uwx^3y^2z + 23uwx^3y^2 - 43ux^3y^3z^3 - 46ux^3y^2 + 29w^3xy^3z^2 - 14w^3x^3y^3z^2 - 45x^3 - 8xy^2).$$

$$m_{12} = (x + y + z - 3)^3.$$

$$m_{13} = (2wz + 45x^3 - 9y^3 - y^2 + 3z^3)(w^2z^3 - w^2 + 47xy).$$

$$m_{14} = (18x^4y^5 + 41x^4y^2 - 37x^4 + 26x^3y^4 + 38x^2y^4 - 29x^2y^3 - 22y^5)(33x^5y^6 - 22x^4 + 35x^3y + 11y^2).$$

$$m_{15} = x^6y^3z^2(12w^2xyz^3 - w^2z^3 + w^2 - 29x - 3xy^2)(14w^2y^2 + 2wz + 18x^3y - 8xy^2 - y^2 + 3z^3).$$

[m_1-m_{15} : from Wang[18)]]

$$d_n = (u^n + v^n)^n - (u^n - v^n)^n.$$

[from Davenport[7)]]

$$s_1 = (3x^2 + x + 1)y^2 + 2xy + x^2 + x.$$

$$s_2 = (y^4 + x^3)(y^3 + x^2)^2(y^2 + x)^3.$$

$$s_3 = (z + y + x + 1)(z - y + x + 4)^2(z - 2y + x + 7)^3.$$

$$s_4 = (y + x^2 + 5)(6y + 2x^3 + 31)^3(xy^3 + 8y - x)^5.$$

$$s_5 = (z^2 + xyz + x^2)^2(3z^2 + (y^2 + x)z - 4)^3(z^3 + z^2 + (x - 1)y)^4.$$

$$s_6 = (3y^4 + x + 5)(6y^2 + 2x + 31)^2((x^2 + x + 1)y^3 - y + x + 8)^4(xy + 8y + x)^{10}.$$

[s_1-s_6 : from Wang-Trager[11)]]

B.3 Data for uni-variate factorization over algebraic extension fields

$$a_1 = x^2 - x + 3.$$

$$a_2 = x^3 + 2.$$

$$a_3 = x^4 - x + 1.$$

$$a_4 = x^6 + 3x^5 + 6x^4 + x^3 - 3x^2 + 12x + 16.$$

$$a_5 = x^9 - 15x^6 - 87x^3 - 125.$$

$a_6 = x^9 - 54.$

$a_7 = x^3 - 19.$

$a_8 = x^2 + x + 7.$

[a_1 - a_8 : from Abbott et al.[12]]

References

1) Knuth, D.E.: The $\mathrm{T_EX}$ book. Reading, Mass., Addison-Wesley, 1984, 483p.
2) Boehm, H-J., and Weiser, M.: Garbage Collection in an Uncooperative Environment. *Soft.-Practice and Experience,* **18**, 9, pp. 807-820 (1988).
3) Knuth, D.E.: Vol. 2, Seminumerical Algorithms. The Art of Computer Programming, 2nd ed., Reading, Mass., Addison-Wesley, 1981, 689p.
4) Collins, G.E.: Subresultants and Reduced Polynomial Remainder Sequences. *J. Assoc. Comput. Mach.*, **14**, 1, pp. 128-142 (1967).
5) Brown, W.S., and Traub, J.F.: On Euclid's Algorithm and the Theory of Subresultants. *J. Assoc. Comput. Mach.,* **18**, 4, pp. 505-514 (1971).
6) Brown, W.S.: On Euclid's Algorithm and the Computation of Polynomial Greatest Common Divisors. *J. Assoc. Comput. Mach.*, **18**, 4, pp. 478-504 (1971).
7) Davenport, J.H., Siret, Y., and Tournier, E.: Computer Algebra. London, Academic Press, 1988, 207p.
8) Kaltofen, E.: "Factorization of Polynomials". *Computer Algebra, Symbolic and Algebraic Computation,* Buchberger, B. et al., ed., New York, Springer, 1982, pp. 95-113.
9) Berlekamp, E.R.: Factoring Polynomials over Finite Fields. *Bell Syst. Tech. J.*, **46**, 8, pp. 1853-1859 (1967); Revised and expanded version is found in Chap. 6 of Berlekamp, E.R.: Algebraic Coding Theory. McGraw-Hill, 1968, 466p.
10) Zassenhaus, H.: On Hensel Factorization. I. *J. Number Theory*, **1**, pp. 291-311 (1969).
11) Wang, P.S., and Trager, B.M.: New Algorithms for Polynomial Square-free Decomposition over the Integers. *SIAM J. Comput.*, **8**, pp. 300-305 (1979).
12) Abbott, J.A., Bradford, R.J., and Davenport, J.H.: Factorisation of Polynomials. Trends in Computer Algebra, Proc. Int. Symp., Janssen, R., ed., Bad Neuenahr, 1987, LNCS 296, Berlin, Springer, 1988, pp. 81-91.
13) Lenstra, A.K., Lenstra, H.W., and Lovasz, L.: Factoring Polynomials with Rational Coefficients. *Math. Ann.*, **144**, pp. 32-39 (1982).
14) Yokoyama, K., and Takeshima, T.: On Factoring and Computation of GCD over Euclidean Rings – an Application of Lattice Algorithms. (in Japanese), *Comput. Soft.*, **5**, pp. 42-61 (1988).
15) Moses, J., and Yun, D.Y.Y.: The EZGCD Algorithm. Proc. ACM Ann. Conf., 1973, ACM, pp. 159-166.
16) Wang, P.S., and Rothschild, L.P.: Factoring Multivariate Polynomials over the Integers. *Math. Comput.*, **29**, pp. 935-950 (1975).
17) Noro, M., Yokoyama, K., Takeshima, T., Sunaga, T., and Tsukamoto, Y.: Second Report on Current State of Risa Computer Algebra System. (in Japanese), Proc. Riken Symp. Symbol. Algebra. Comput. Sci. Comput. Front., held at Riken Inst. Chem. Phys. Res., 1990, pp. 26-31.
18) Wang, P.S.: An Improved Multivariate Polynomial Factoring Algorithm. *Math. Comput.*, **32**. pp. 1215-1231 (1978).
19) Hearn, A.C.: An Improved Non-modular GCD Algorithm. *SIGSAM Bul.*, **6**, pp. 10-15 (1972).
20) Brown, W.S.: The Subresultant PRS Algorithm. *ACM Trans. Math. Soft.*, **4**, 3, pp. 237-249 (1978).
21) Suzuki, M., and Sasaki, T.: Improvements of PC-PRS Algorithm. (in Japanese), Proc. Symp. Comput. Algebra Appr. Math. Res., RIMS KOKYUROKU 722, Niki, N., ed., Kyoto, 1989, Res. Inst. Math. Sci., Kyoto Univ., 1990, pp. 1-16.
22) Collins, G.E.: The Calculation of Mutivariate Polynomial Resultants. *J. Assoc. Comput. Mach.*, **18**, 4, pp. 515-532 (1971).
23) Rothstein, M.: Aspects of Symbolic Integration and Simplification of Exponential and Primitive Functions. Univ. of Wisconsin, 1976, Ph. D. Thesis.
24) Trager, B.M.: Algebraic Factoring and Rational Function Integration. Proc. ACM Symp. Symbol. Algebra. Comput., New York, ACM, 1976, pp. 219-226.
25) Sasaki, T., and Noda, M.: Approximate Square-free Decomposition and Root-finding of Ill-conditioned Algebraic Equations. *J. Info. Proc.*, **12**, pp. 159-168 (1989).
26) Sasaki, T., and Sasaki, M.: Analysis of Accuracy Decreasing in Polynomial Remainder Sequence with Floating-point Number Coefficients. *J. Info. Proc.*, **12**, pp. 394-403 (1989).
27) Noda, M., Sasaki, T., and Suzuki, M.: Validated

Computations by Symbolic/Numeric Hybrid Algorithms. (in Japanese), *JOHO SHORI*, **31**, pp. 1204-1211 (1990).
28) Yokoyama, K., and Takeshima, T.: On Factorization of Uni-variate Polynomials over Finite Fields. *Int. Inst. Adv. St. Soc. Infor. Sci. (IIAS-SIS), Res. Rep.*, **69**, 1986, 20p.
29) Yokoyama, K., Noro, M., and Takeshima, T.: "On Factoring Multi-variate Polynomials over Algebraically Closed Fields". Proc. Int. Symp. Symbol. Algebra. Comput., New York, ACM, 1990, p. 297.
30) Yokoyama, K., Noro, M., and Takeshima, T.: On Factoring Multi-variate Polynomials over Algebraically Closed Fields. *RISC-LINZ, Res. Rep.*, **90**-26, 1990, 8p.
31) Kaltofen, E.: Polynomial-time Reductions from Multivariate to Bi- and Univariate Integral Polynomial Factorization. *SIAM J. Comput.*, **14**, pp. 469-489 (1983).
32) Kaltofen, E.: Fast Parallel Absolute Irreducible Testing. *J. Symbol. Comput.*, **1**, pp. 57-67 (1985).
33) Chistov, A.L., and Grigor'ev, D.Yu.: Subexponential-time Solving Systems of Algebraic Equations I. LOMI Prepr. E-9-83, Leningrad, 1983.
34) Yokoyama, K., Noro, M., and Takeshima, T.: Computing Primitive Elements of Extension Fields. *J. Symbol. Comput.*, **8**, 6, pp. 553-580 (1989).
35) Yokoyama, K., Noro, M., and Takeshima, T.: On Determining the Solvability of Polynomials. Proc. Int. Symp. Symbol. Algebra. Comput., New York, ACM, 1990, pp. 127-134.
36) Landau, S., and Miller, G.L.: Solvability by Radicals is in Polynomial Time. *J. Comput. Syst. Sci.*, **30**, pp. 179-208 (1985).
37) Sasaki, T., and Takeshima, T.: A Modular Method for Gröbner-basis Construction over $\mathbb{Q}$ and Solving System of Algebraic Equations. *J. Info. Proc.*, **12**, pp. 371-379 (1989).
38) Yokoyama, K., Noro, M., and Takeshima, T.: Solutions of Systems of Algebraic Equations and Linear Maps on Residue Rings. *IIAS-SIS Res. Rep.*, **94**, 1989, 20 p.
39) Yokoyama, K., Noro, M., and Takeshima, T.: Solutions of Systems of Algebraic Equations and Linear Maps on Residue Rings. *IIAS-SIS Res. Rep.*, **103**, 1990, 28 p., (submitted to J. Symbol. Comput.).

Taku Takeshima

International Institute for Advanced Study of Social Information Science, FUJITSU LABORATORIES LIMITED
Bachelor of Control Eng.
Tokyo Institute of Technology 1971
Master of Control Eng.
Tokyo Institute of Technology 1973
Specializing in Computer Algebra

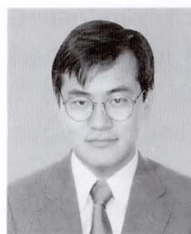

Kazuhiro Yokoyama

International Institute for Advanced Study of Social Information Science, FUJITSU LABORATORIES LIMITED
Bachelor of Science in Mathematics
The University of Tokyo 1981
Dr. of Science in Mathematics
Kyushu University 1991
Specializing in Algebraic Combinatorics and Computer Algebra

Masayuki Noro

International Institute for Advanced Study of Social Information Science, FUJITSU LABORATORIES LIMITED
Bachelor of Science in Mathematics
The University of Tokyo 1983
Master of Science in Mathematics
The University of Tokyo 1985
Specializing in Computer Algebra

UDC 620.168:681.327.634

Boron/Magnesium Sintered Composites for Computer Peripherals

• Eiji Horikoshi • Takehiko Sato *(Manuscript received June 3, 1991)*

A magnesium-based sintered composite, reinforced with boron particles, has been developed that has an increased modulus of elasticity and controllable thermal expansion coefficient. A 6vol%boron/magnesium-9wt% aluminum composite has an excellent modulus of elasticity 1.3 times that of the ordinary magnesium alloy and a thermal expansion coefficient close to aluminum alloy. This composite also has improved machinability as the size of the boron particles is controlled. A head-arm component for a disk drive was experimentally produced using this composite, and it was found that the composite causes greatly decreased thermal off-track error in the disk drive.

1. Introduction

Downsizing is the strongest trend in component design today.

Typical of computer peripherals illustrating this trend is the disk drive in which components, such as the head actuator arms and carriages, require lightweight, high-strength materials to meet needs for larger capacity and high-speed data access.

In the disk drive, many components made of aluminum (Al) alloy have been used because of its lightweight, high-strength properties. If there is any material which is lightweight, high-strength and has a thermal expansion coefficient close to that of Al alloy, it will become a suitable material for the components.

Magnesium-based (Mg-based) alloys have the greatest potential in this regard if their modulus of elasticity can be increased and if their thermal expansion coefficient can be brought close to that of Al alloy.

Approaches to improving the modulus of elasticity of these Mg-based alloys have used new techniques such as squeeze and pressure casting. These techniques are combined with composite material processing using reinforcing materials such as carbon fibers, sillicon-carbide whiskers, and alumina particles[1),2)]. Fortunately, the thermal expansion coefficient of these composite materials can be controlled by varying the amount of reinforcing materials[2)].

But precise components with uniform alloy structure have not yet been fabricated using these composite materials.

The sintering of near-net shapes produces small precise components with a uniform alloy structure. Very little work, however, has been done on Mg-based alloys[3)]. To develop a Mg-based alloy with an improved modulus of elasticity in the form of a precision component, the authors combined a composite material technique with sintering.

Since Al has a large solid solubility in Mg[4)], a Mg-Al alloy matrix was selected to obtain solid-solution hardening. Boron particles were used for reinforcement because boron does not react with Mg[5)].

Generally, composite materials show less machinability because they contain a large number of whiskers, fibers or particles which are very hard. Despite progress in powder metallurgy, it is not yet possible to produce certain geometrical features, such as transverse holes and undercuts, which thus frequently necessitate

machining, particularly drilling.

Against this background, the authors developed the boron/Mg-Al sintered composite having an increased modulus of elasticity, controllable termal expansion coefficient and excellent machinability. Then the composite was evaluated as a material for a head-arm component.

2. Experiment

A Mg-6wt%Al alloy was used in evaluating the sintering atmosphere for Mg-Al alloys. Boron particles were then used to reinforce the Mg-6wt%Al sintered alloy. The relationship between boron content and the modulus of elasticity was studied. To determine the dependence of the modulus of elasticity on the Al content, the Al content of the boron/Mg sintered composite system was varied. The dependence of the boron content on the thermal expansion coefficient was then measured.

The following sintering experiments were performed.

Table 1 shows the specifications for the starting powders, ground Mg powder (average particle size: 50 μm), gas-atomized Al powder (average particle size: 30 μm), and crushed or reduced boron. To study the effect of the boron particle size on machinability, the average particle size of boron was varied from 1 μm to 15 μm.

In mixing, special attention was paid to obtain a uniform mixture of coarse Mg powder and fine boron powder. Powders were mixed for two hours in a V-shell blender or a grinding mixer with ethyl alcohol. To investigate the optimum composition or thermal expansion coefficient, the boron content was varied between 0 vol% and 20 vol%. Then the Al content was varied between 0 wt% and 18 wt% to determine the composition with the highest modulus of elasticity.

Mixtures were compacted into a 97 mm x 6 mm x 4 mm tensile test piece under pressure of 400 MPa.

Mg-6wt%Al samples were sintered at 560 °C to 620 °C for one hour in an argon, hydrogen, or nitrogen atmosphere. Samples in which the ratios of boron and aluminum were varied were sintered under the conditions optimized for the Mg-6wt%Al alloy.

Table 1. Starting powder specification

Powder	Purity (%)	Particle size (μm)	Fabrication
Mg	99.9	50	Ground
Al	99.9	30	Gas-atomized
Boron	99.8	15	Crushed
Boron	99.7	10	Crushed
Boron	99.5	5	Crushed
Boron	95.7	1	Reduced

The mechanical properties were measured with an Instron Universal Test Machine at a cross-head speed of 1 mm/min.

Optical microscopy and XMA analysis were then used to evaluate the microstructures.

The machinability indices were determined by measuring the tool wear, cutting resistance, and cut chips during machining. Tool wear was determined by the outer corner wear of the cemented-carbide drill bits, 2 mm in dia, after three holes were drilled in a test piece 6 mm thick. Outer corner wear was measured as the difference between the virgin edge and the worn edge on the corner of the drill bit. The cutting resistance was measured by an oblique cutting test with sintered diamond cutting tools. The oblique cutting test was done with a lathe at a cutting speed of 200 m/min, a cutting depth of 0.5 mm, and a cutting feed of 0.1 mm/rev. Worn drill bits and cut chips were evaluated using SEM.

The thermal off-track error is thought to be caused by the difference in the thermal expansion coefficients between the disk material (aluminum) and the head-arm material (magnesium). To measure the improvement in thermal off-track error, a new head-arm was made using 6vol%boron/Mg-9wt%Al having a thermal expansion coefficient close to that of aluminum. The arm size is 57 mm x 24 mm x 4 mm. It has six small tapped holes 0.8 mm in dia.

3. Results and discussion

3.1 Sintering conditions

Figure 1 shows the relationship between the sintering temperature and the modulus of elas-

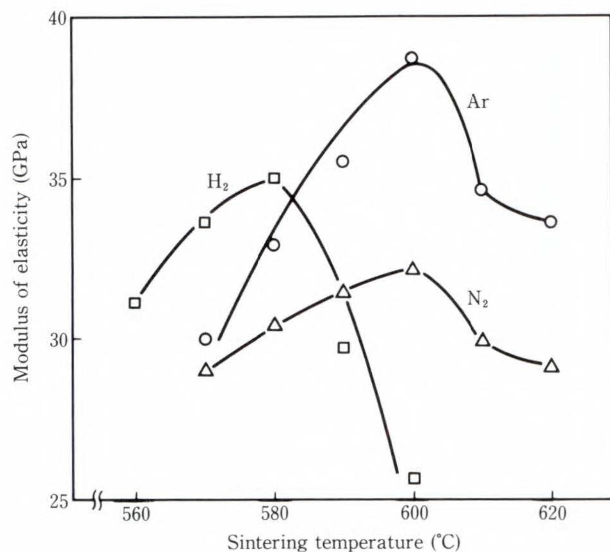

Fig. 1—Relationship between sintering temperature and the modulus of elasticity of the Mg-6wt%Al alloy sintered in an argon, hydrogen, or nitrogen atmosphere.

ticity of the Mg-6wt%Al alloy sintered for one hour in an argon, hydrogen, or nitrogen atmosphere. The maximum values for the modulus of elasticity are different for each atmosphere. The sample sintered at 600 °C for one hour in argon has the highest modulus of elasticity, 39 GPa. When the sample is sintered above 600 °C, the microstructure becomes coarse and the modulus of elasticity becomes lower. When the sample is sintered below 600 °C, the densification is insufficient. Consequently, the modulus of elasticity becomes lower.

The sample sintered in hydrogen has a maximum modulus of elasticity at a temperature 20 °C lower than the sample sintered in argon or nitrogen. Hydrogen makes the Mg-6wt%Al microstructure too coarse because the powders become more active in hydrogen. This is why the sample sintered in hydrogen has lower modulus of elasticity than the sample sintered in argon[6].

In the microstructure of the sample sintered in nitrogen, the formation of magnesium nitride (Mg_3N_2) is observed at the grain boundaries[6]. Mg_3N_2 is well known to be brittle[4]. Thus, the modulus of elasticity is less than that of the sample sintered in argon.

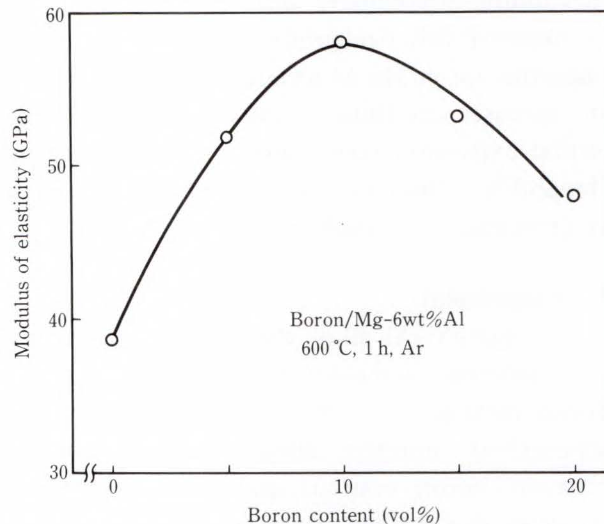

Fig. 2—Relationship between the modulus of elasticity and boron content in the Mg-6wt%Al alloy.

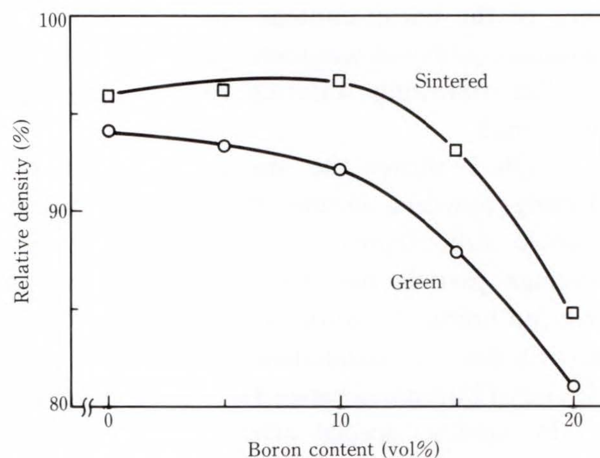

Fig. 3—Relationship between density and boron content.

Sintering in argon at 600 °C is therefore optimum for the Mg-6wt%Al alloy, since no brittle phases are formed and grain growth and densification are balanced.

3.2 Optimum composition and thermal expansion coefficient

3.2.1 Boron content

Figure 2 shows the relationship between the modulus of elasticity and boron content in the Mg-6wt%Al alloy sintered in argon at 600 °C for one hour. The average particle size of the boron is 15 μm. The modulus of elasticity increased with the addition of boron, probably because boron particles reinforce the matrix at the com-

posion of up to 10% by volume. When the boron content increases above this, the modulus of elasticity decreases. The reason is as follows.

The green and sintered densities are shown in Fig. 3 as a function of the boron content. The green density decreases abruptly when the boron content exceeds 10% by volume because boron particles tend to reduce the compactibility of the green sample. Hard boron particles reduce the smooth movement of the compacting dies. Correspondingly, the sintered density decreases, which results in reducing the modulus of elasticity.

3.2.2 Aluminum content

The dependence of the modulus of elasticity on Al content is shown in Fig. 4. The modulus of elasticity has a maximum value of 63 GPa, 1.4 times higher than that of the cast Mg-Al alloy without boron, when the Al content is 9% by weight.

A typical microstructure of the composite, 10vol%boron/Mg-9wt%Al, exhibiting a maximum modulus value, is shown in Fig. 5.

Figure 6 shows the result of XMA analysis for the samples containing 6%, and 9% Al by weight, and 10% boron by volume. The X-ray was scanned across boron particles. Both samples have a uniform distribution of Al and Mg in the matrix. However, the sample containing 9% Al by weight, the composite with the highest

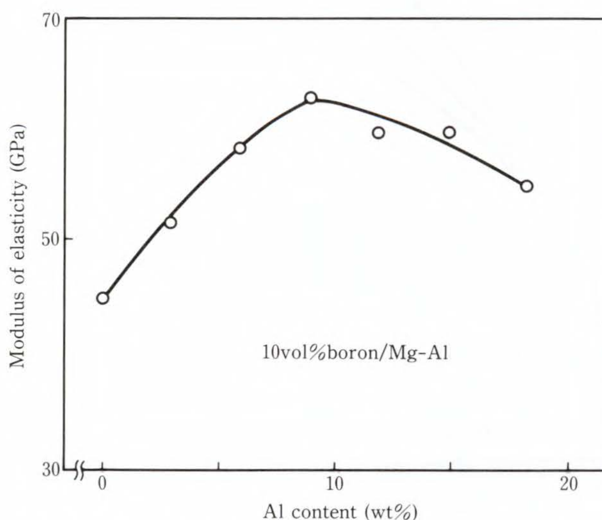

Fig. 4—Dependence of the modulus of elasticity on the aluminum content.

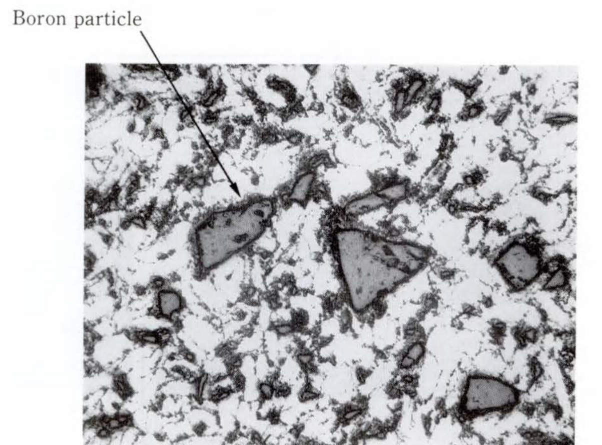

Fig. 5—Typical microstructure of the 10vol%boron/Mg-9wt%Al composite.

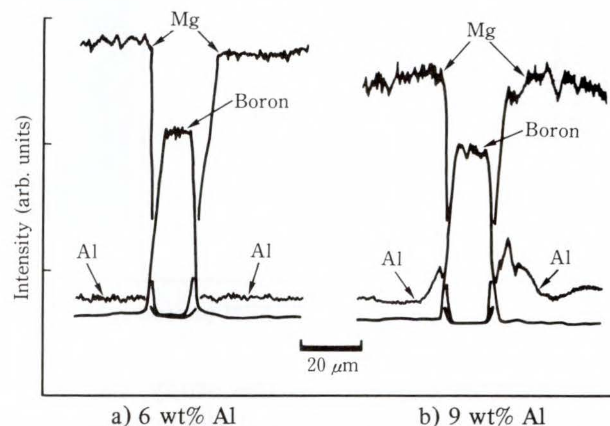

Fig. 6—Results of XMA analysis for two samples. The X-ray was scanned across boron particles.

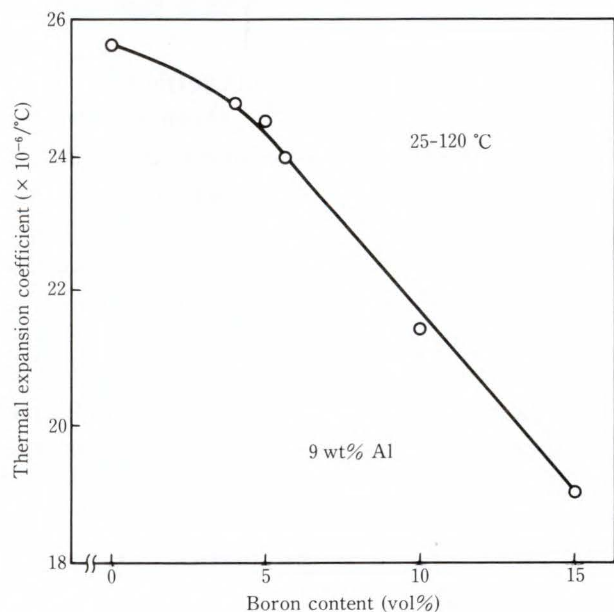

Fig. 7—Dependence of the thermal expansion coefficient on the boron content.

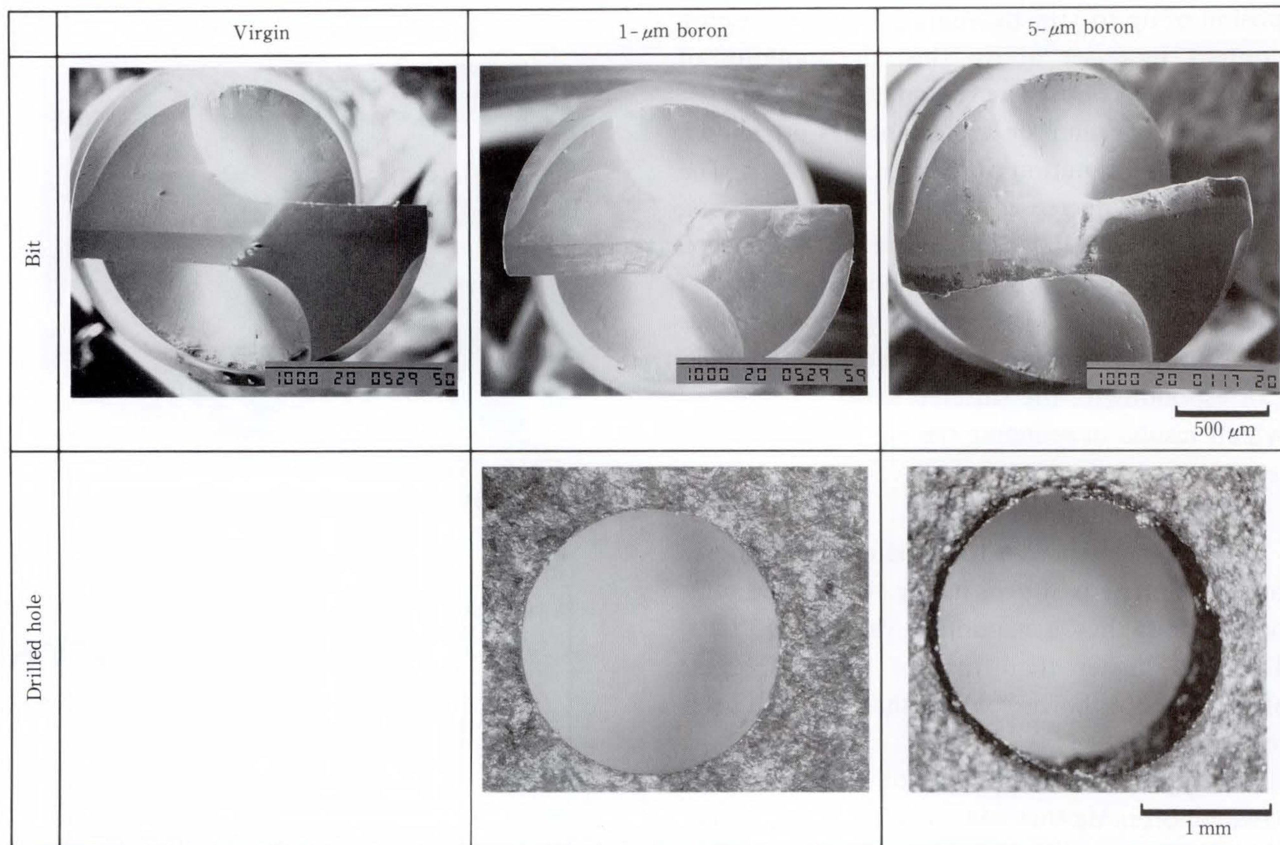

Fig. 8–SEM photographs of worn bits and optical photographs of holes.

modulus of elasticity in this study, has an Al-rich layer several microns thick around the boron particles. This concentration may promote the adhesion of boron and Mg, resulting in a boron/Mg-Al composite with a high modulus of elasticity.

3.2.3 Thermal expansion coefficient

The dependence of the thermal expansion coefficient on the boron content for the sample with 9% Al by weight is shown in Fig. 7. The thermal expansion coefficient decreases linearly with increasing boron content, indicating that the thermal expansion coefficient can also be controlled by the boron content. This provides more flexibility in how the alloy can be used. For example, the thermal expansion coefficient of a 6vol%boron/Mg-9wt%Al composite is close to that of the Al alloy (24×10^{-6} /°C).

3.3 Effect of the boron particle size on machinability

3.3.1 Tool wear

Perhaps the most meaningful measure of machinability is tool wear.

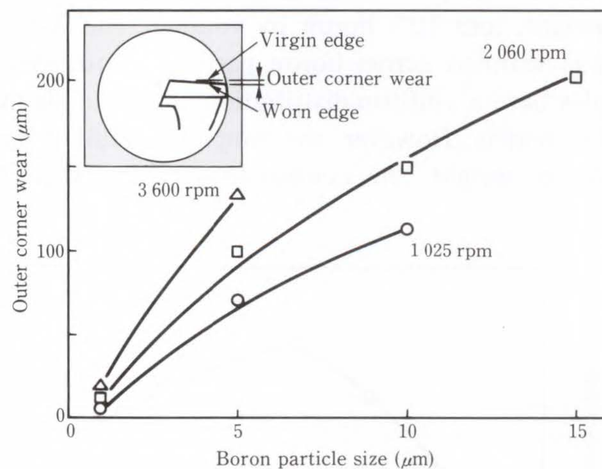

Fig. 9–Relationship between boron particle size and outer corner wear.

Figure 8 shows bits before and after three holes were drilled in the test piece, together with the holes through which bits exited. The cutting edge of the bit used for drilling the 1-μm boron sample had little damage, but that for drilling the 5-μm boron sample was heavily damaged,

especially at the outer corners. The hole features reflect these facts. The test piece with 5-μm boron particles shows chips around the hole. But the test piece with 1-μm boron particles shows no chips around the hole.

Figure 9 summarizes the outer corner wear as a function of boron particle size at different drilling speeds. Fine boron particles improve machinability.

The tool life is increased by over 30 times by using 1-μm boron particles instead of 5-μm particles.

3.3.2 Cutting resistance

The cutting resistance during machining can also be used to predict machinability. Low cutting resistance generally means low tool wear and good machinability[7].

Figure 10 shows the cutting resistances in an oblique-cutting test for samples with different boron particle sizes. The F_p curve crosses the F_v curve when the boron particle size exceeds 5 μm. This may be caused by the larger boron particles tending to remain not in the cut chip but in the workpiece. The cutting resistance F_z decreases with boron particle size, in agreement with the machinability obtained from the tool wear.

3.3.3 Cut chips

The sample with 1-μm boron particles gives long curled chips, a sign of good machinability as shown in Fig. 11. Chips of the sample with 5-μm boron particles are cracked and broken.

Figure 12 shows typical microstructures for sintered composites. In sample a), the fine boron particles (1 μm) collect together to from a network-like pattern in the grain boundaries, but individual particles are microscopically isolated in the sample with 6 vol% boron.

As shown in sample b) of Fig. 12, the larger boron particles (5 μm) are dispersed at random in the alloy matrix. In b) of Fig. 13, note how even one large boron particle can occupy a large

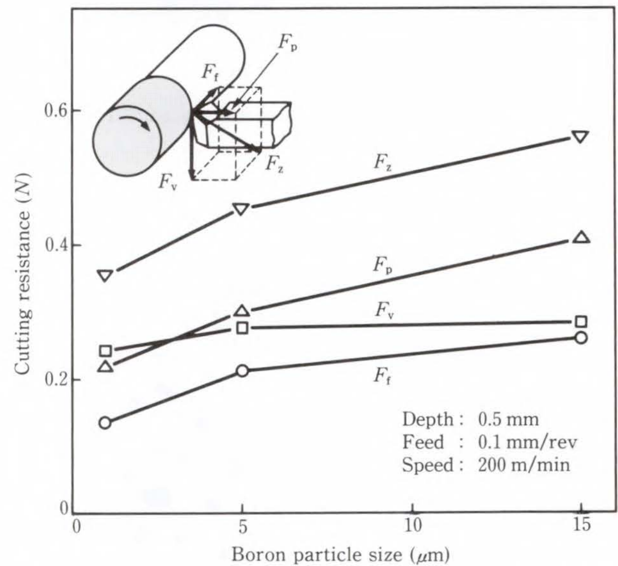

Fig. 10—Relationship between the cutting resistance and boron particle size.

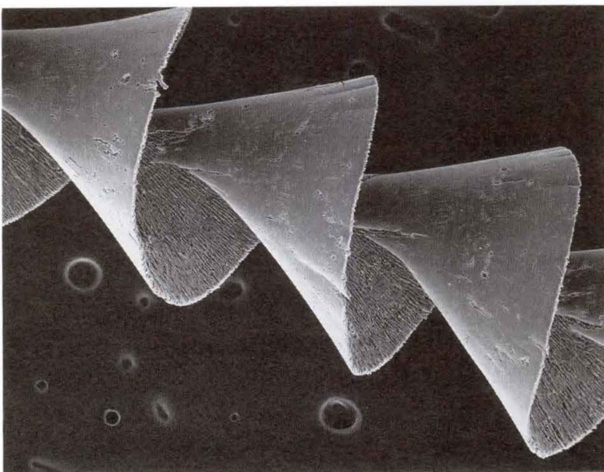

a) 1-μm boron

b) 5-μm boron

Fig. 11—Cut chips.

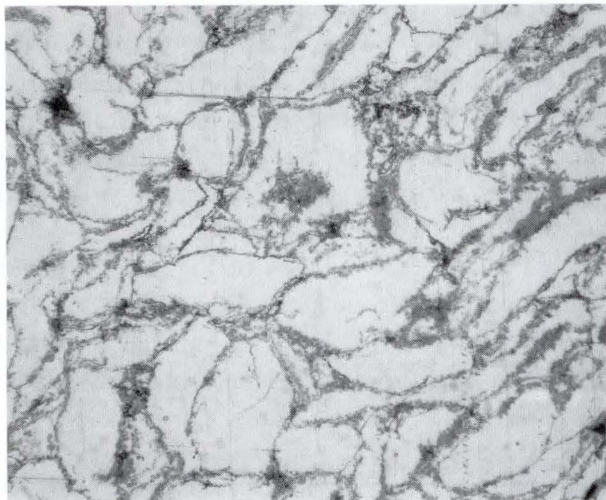

a) 1-μm boron

b) 5-μm boron

Fig. 12–Optical microstructures of the 6vol%boron/Mg-9wt%Al sintered composites.

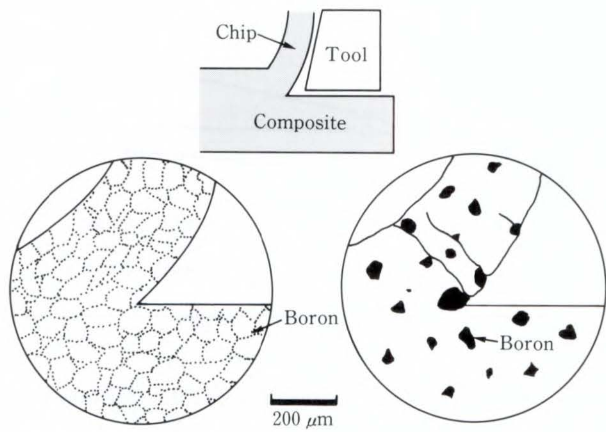

a) 1-μm boron b) 5-μm boron

Fig. 13–Cutting chips.

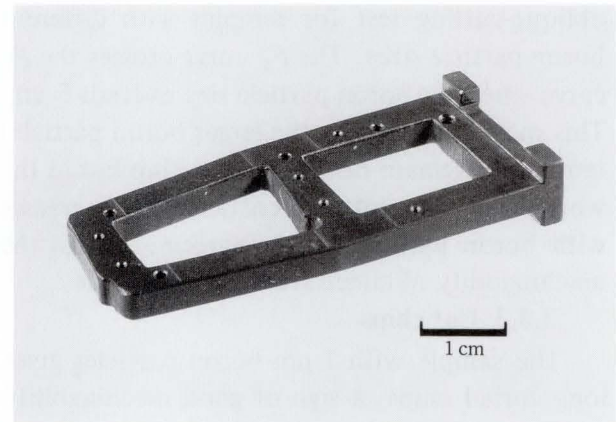

Fig. 14–Disk drive head actuator arm.

part of the chip. The weak interface between the boron and the alloy matrix may cause cracks under the bending stress caused by the cutting tool. The chip is then easily broken. This tendency increases as the ratio of cutting depth to boron particle size decreases. A small ratio causes boron particles to fall off and increases tool wear. Fine boron particles, such as those in sample a) of Fig. 13, do not cause this problem.

3.4 Application to a disk drive

To ascertain the improvement in machinability and the controllable thermal expansion coefficient, a head-arm for a disk drive was made

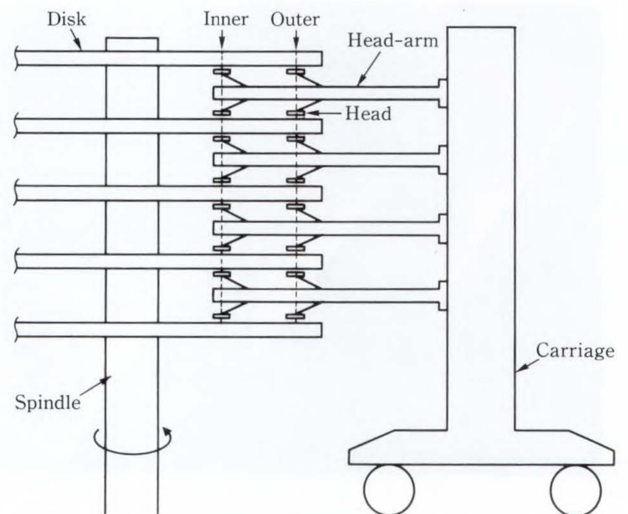

Fig. 15–Schematic drawing of measuring thermal off-track.

applying the new composite material, then the thermal off-track error was measured.

Figure 14 shows a head actuator arm. An experimental schema for measuring thermal off-track is shown in Fig. 15. This head-arm has two read-write heads on one side and a total of four heads on both sides. Four head-arms with 16 heads were assembled in a disk enclosure. The distance between outer and inner heads is 21 mm.

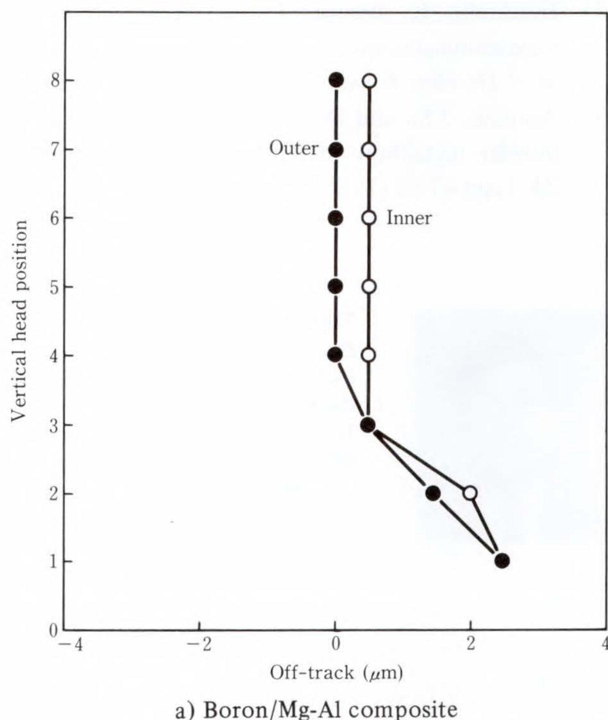

a) Boron/Mg-Al composite

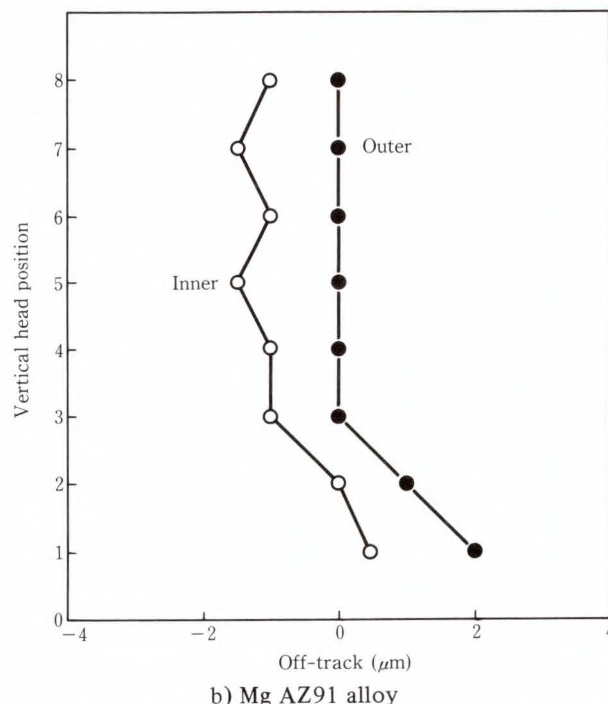

b) Mg AZ91 alloy

Fig. 16–Sample measurement of off-track error.

Figure 16a) shows a typical example of off-track measurement. As a reference, off-track data of a conventional head-arm component of the Mg AZ91 alloy (Mg-9wt%Al-1wt%Zn) is shown in Fig. 16b). The vertical fourth position of the outer head is the servo head used as the reference position. In the five upper head positions, the absolute values of off-track 1 μm to 1.5 μm are observed for the Mg AZ91 alloy. In the 6vol%boron/Mg-9wt%Al composite, the absolute value of the off-track decreased to 0.5 μm. Clearly, the off-track error decreased by 1/2 to 1/3 by using the composite. Here, the reason why the off-track value does not become zero despite using the same thermal expansion coefficient material as the disk material might be because the temperature in the head-arm is slightly lower than that in the disk. The off-track error of the two lower positions (1 and 2) are larger than that of the upper positions. The larger off-track is thought to be caused by the thermal deformation in the mechanical structure.

4. Conclusion

The authors developed a boron/Mg-Al sintered composite and applied it to the head-arm component of a disk drive.

The results can be summarized as follows:

1) A new boron/Mg-Al composite that exhibits an increased modulus of elasticity was developed by sintering. A maximum modulus of elasticity of 63 GPa is achieved in a 10vol%boron/Mg-9wt%Al composite. This modulus of elasticity is 1.4 times greater than that of the cast Mg-Al alloy.
2) The thermal expansion coefficient of the boron/Mg-Al system decreases linearly with increasing boron content. When the sample contains 6 vol% boron, the thermal expansion of the composite is close to that of Al.
3) The larger the boron particles, the greater the tool wear. Tool life is increased over 30 times using material containing 1-μm boron

particles instead of 5-μm particles, for example.

4) When the head-arm component is made of this sintered 6vol%boron/Mg-9wt%Al composite, the thermal off-track error is reduced by 1/2 to 1/3 of the error found in head-arms made of conventional materials.

References

1) Lewis, C.F.: The exciting promise of metal-matrix composites. *Materials Eng.*, **103**, 5, pp.33-37 (1986).
2) Sherman, R.: Auger analysis of metal matrix-ceramic fiber composites. *Surface and Interface Anal.*, **10**, pp.23-28 (1987).
3) Storchheim, S.: Magnesium powder metallurgy. *Int. J. Powder Met.*, **8**, pp.115-126 (1972).
4) Hansen, M.: Constitution of binary Alloys. 2nd ed., McGraw-Hill, 1958, pp.105-110, and p.909.
5) Alexander, J.A., Stuhrke, W.F., and Cung, K.O.: The elevated temperature reactivity in boron metal matrix composite materials. *SAMPE*, **10**, F-91 (1966).
6) Horikoshi, E., Iikawa, T., and Sato, T.: Boron/magnesium-aluminum sintered composite alloy. *Mod. Develop. Powder Met.*, **19**, pp.579-590 (1988).
7) Agapiou, J.S., and DeVries, M.F.: Machinability of powder metallurgy materials. *Int. J. Powder Met.*, **24**, 1, pp.47-52 (1988).

Eiji Horikoshi
Electronics Packaging Laboratory
FUJITSU LABORATORIES, ATSUGI
Bachelor of Materials Science
Tohoku University 1978
Master of Materials Science
Tohoku University 1980
Specializing in Materials Science

Takehiko Sato
Electronics Packaging Laboratory
FUJITSU LABORATORIES, ATSUGI
Bachelor of Materials Science
Tohoku University 1969
Specializing in Materials Science

UDC 621.395.65:621.391.6

Moving-Fiber Optical Switch Using $LiNbO_3$ Piezoelectric Actuator

• Noboru Wakatsuki • Hisashi Sawada • Masanori Ueda

(Manuscript received June 24, 1991)

The need for a fast, miniaturized, optical switch with low insertion loss has increased with the proliferation of optical communications and optical signal processing. This paper describes a moving-fiber optical switch consisting of a $LiNbO_3$ piezoelectric actuator having an antipolarized ferroelectric laminar domain (inversion layer). A new construction technique simplifies optical axis alignment and makes fiber end-face polishing unnecessary. A 2 x 2 moving-fiber optical switch constructed using the above techniques has an insertion loss within 0.8 dB and a switching time less than 10 ms.

1. Introduction

The need for a fast, compact, and inexpensive switch with low insertion loss has increased with the accelerating growth of optical communications and signal processing. Although most optical switches use mechanical components because of their low loss and optical mode independency, these components require precise assembly and adjustment, and are difficult to mass produce.

There are three types of mechanical switches: switches that use moving prisms, switches that use moving mirrors, and switches that move the fibers. Moving-fiber switches have following advantages:

1) Simple structure and low component count
2) Low insertion loss and fast switching speed

However, moving-fiber switches require precise fiber alignment.

To minimize size and cost, we derived the acceptable positioning margins from the optical losses caused by the following: the Fresnel reflection at the fiber end-faces, transverse offset, angular misalignment, longitudinal separation of the fiber ends, and incomplete fiber end-faces. For the new switch we chose a fifty-micron diameter graded index (GI) optical multimode fiber and an LED light source with a wavelength of 1.3 μm.

We developed a new switch structure that secures the fibers in V-shaped grooves anisotropically etched in silicon and a method of precisely mounting the fibers using a water-soluble resin. Array precision is obtained by cutting fibers using a dicing saw. This produces smooth fiber end-faces without the need for polishing.

A piezoelectric bimorph actuator compares favorably with electromagnetic actuators in terms of size and speed. However, conventional piezoelectric ceramic actuators have the disadvantages of hysteresis and creep (displacement during change-over) due to adhesion of the two ceramic plates. The $LiNbO_3$ piezoelectric actuator having an antipolarized ferroelectric laminar domain (inversion layer) proposed by Shimizu et al[1),2)] has no adhesion layer and executes fast and precise fiber movement.

We developed a 2 x 2 moving-fiber optical switch using multimode fiber. This switch features a switching time of 10 ms or less, and a loss of 0.8 dB or less.

2. Optical switching losses

Fresnel reflection at the fiber end-faces, transverse offset, angular misalignment, longitudinal separation of the fiber ends, and incomplete fiber end-faces contribute to the

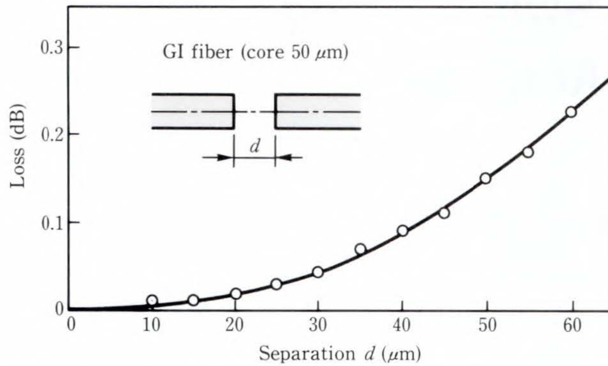

Fig. 1—Optical coupling loss due to fiber end-separation.

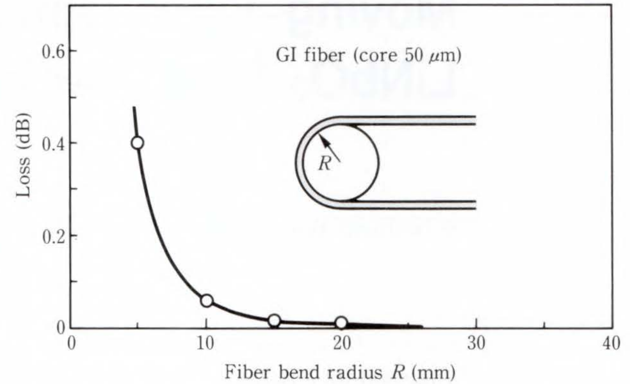

Fig. 3—Optical travelling loss due to fiber bending.

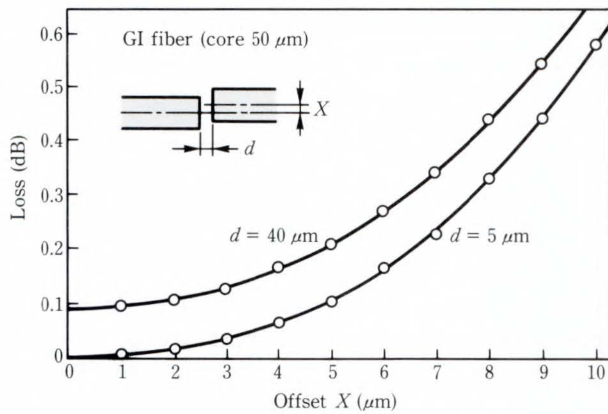

Fig. 2—Optical coupling loss due to transverse offset.

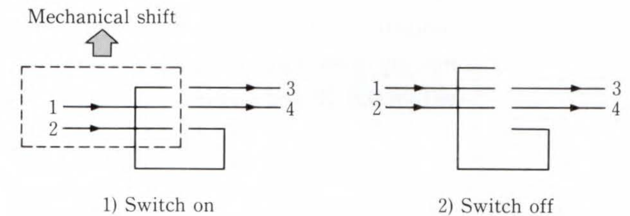

Fig. 4—Optical switching circuit.

Table 1. Estimated losses of moving-fiber optical switch

Loss factor	Loss	Condition
Fresnel reflection at fiber end-faces	0.31 dB	n = 1.5
Fiber end-separation	0.1 dB	Gap: 40 μm
Transverse offset	0.1 dB	Offset: 5 μm

overall coupling loss in fiber splices.[3)] Figures 1 and 2 show the optical coupling losses in 50 μm diameter GI fiber due to fiber end-separation and transverse offset, respectively. An LED emitting at 1.3 μm was used for the measurement. Using an optical fiber mode scrambler allows only traveling modes to pass through the fiber. Figure 1 shows the optical coupling loss due to the spacing between the fiber end-faces in the changeover section. A fiber separation of 40 μm increases the loss by 0.1 dB. Figure 2 shows the optical coupling loss due to transverse offset for two values of fiber end-separation. Table 1 shows the estimations of the optical coupling losses including the Fresnel reflection loss at the fiber end-faces. For an optical switch, losses due to angular misalignment, roughness, and contamination of end-faces must be added.

The relationship between fiber bending radii and traveling losses is important factors when miniaturizing a moving fiber switch. Figure 3 shows the experimental losses for traveling modes.

3. Structure of optical switch

Figure 4 shows the switching circuits for an experimental 2 x 2 optical switch. When the switch is off, fiber 1 is connected to fiber 4 and fiber 2 is connected to fiber 3. When the switch is on, fiber 1 is connected to fiber 3 and fiber 2 is connected to fiber 4. The loss in the optical path between fibers 2 and 3 is greater than in the other paths because light passes through the changeover section twice.

Figure 5 shows the structure of the optical switch. One fiber array is secured to a stationary table, while the other is mounted on top of the bimorph actuator. Switching is accomplished by

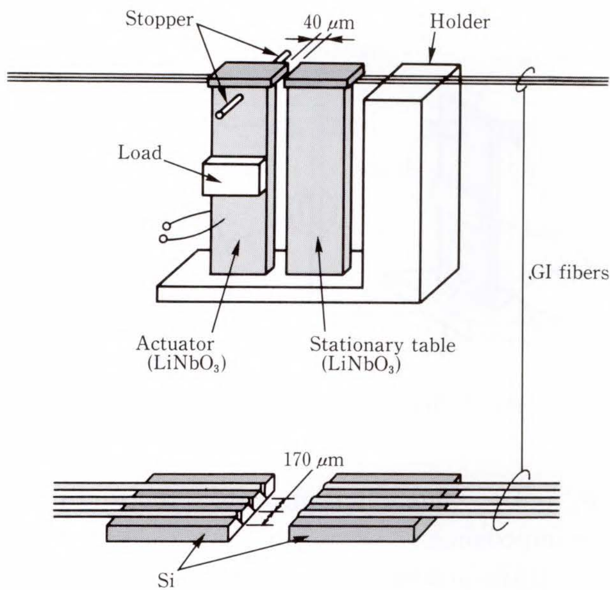

Fig. 5—Structure of the optical switch.

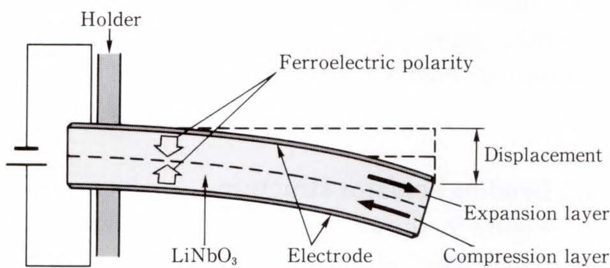

Fig. 6—Principle of piezoelectric $LiNbO_3$ actuator having oppositely-polarized layers.

a 170 μm lateral displacement of the actuator.

A piezoelectric bimorph (see Fig. 6) was selected for the actuator because of its smaller size and higher speed relative to solenoid-type actuators. A voltage applied across the two oppositely polarized layers of the actuator's piezoelectric plate causes one layer to expand and the other to contract. These movements bend the plate and reposition the movable array relative to the stationary array. The two fiber arrays are separated by a 40 μm gap and their optical axes are aligned. The fibers are arranged 170 μm apart in V-shaped grooves that are anisotropically etched in a silicon substrate. The fibers are 50 μm core GI fiber.

4. Piezoelectric bimorph actuator[1),2),4)]

A piezoelectric bimorph actuator consisting of a reverse-polarized $LiNbO_3$ crystal plate was developed to meet the requirements of precision positioning, simplified structure, and faster switching. $LiNbO_3$ crystal produces oppositely polarized layers when heated slightly below the Curie temperature. Unlike other types of ceramic piezoelectric bimorphs, the $LiNbO_3$ bimorph can be fabricated on a single plate.

4.1 Reverse-polarized $LiNbO_3$ crystal

An antipolar ferroelectric laminar domain (inversion layer) can be obtained from single $LiNbO_3$ crystals by Ti diffusion or by heat treatment at a temperature slightly below the Curie point. These polarization inversion phenomena occur without an external electrical field.

Piezoelectric devices based on such an inversion layer include resonators, filters, ultrasonic transducers, and actuators. Because the polarity of ferroelectricity in a piezoelectric plate defines the direction of the strain caused by an electric field, applying a voltage to both sides of the $LiNbO_3$ plate causes strain in opposite directions in the inversion and noninversion domains, and therefore produces mechanical displacement.

Conventional piezoelectric actuators consist of two piezoelectric plates of opposite polarity cemented together. These actuators are difficult to fabricate and are subject to irregularity due to variations in characteristics such as hysteresis and creep. Actuators based on $LiNbO_3$ with an inversion layer are better suited to volume production because they can be manufactured by heat treatment without cementing, and have no hysteresis or creep.

To make the new actuator, an inversion layer was formed on 140°-rotated *Y*-cut $LiNbO_3$ with a maximum piezoelectric strain constant of d_{23} ($d_{23} = -30 \times 10^{-12}$ C/N). This was achieved by heating to 1 155 °C for 24 hours in a mixture of oxygen and nitrogen after Ti diffusion. The resulting crystal was cut parallel to the *X*-axis, then etched in a mixture of boiling HNO_3 and HF. The inversion layer of the crystal cross section progresses to the center of the plate. Figure 7 shows the cross section of 140°-rotated *Y*-cut $LiNbO_3$.

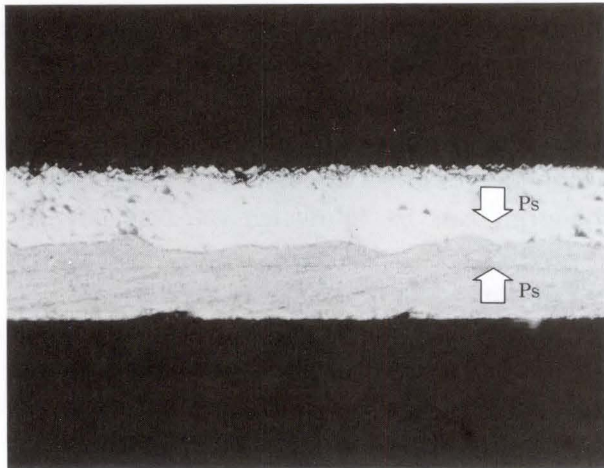

Fig. 7–Cross section of a 200-μm thick 140 °-rotated Y-cut $LiNbO_3$ plate with inversion layer.

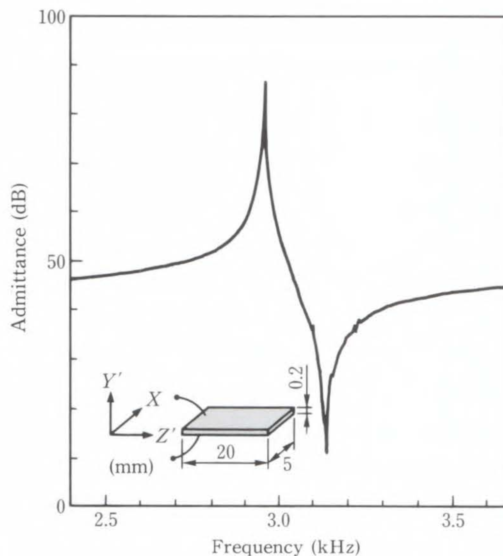

Fig. 8–Bending vibration of 140 °-rotated Y-cut $LiNbO_3$ plate with inversion layer.

To evaluate the material, the bending vibration response was measured for a $LiNbO_3$ plate cut from a wafer with electrode layers deposited on both sides. The existence of the inversion layer was confirmed by measuring the capacitance ratio C_d/C of bending vibration and by comparing it with the theoretical value. The capacitance ratio was determined from the resonant frequency F_r and the antiresonant frequency f_a as shown in Equation (1).

$$C_d/C = F_r^2/(F_a^2 - F_r^2). \qquad \text{(1)}$$

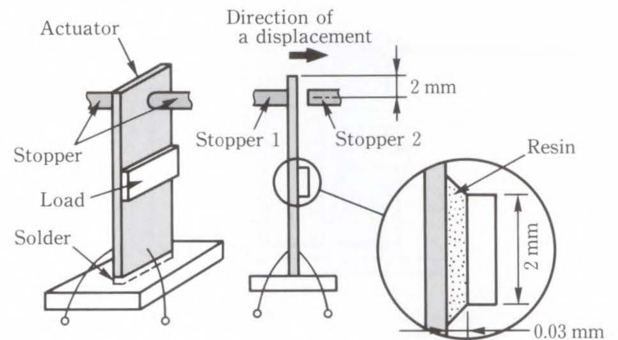

Fig. 9–Structure of piezoelectric actuator.

F_r and F_a were determined from the admittance or impedance.

If the inversion layer progresses to the center of the plate, the value of C_d/C should agree with the theoretical value. Figure 8 shows the bending vibration response of a 140 °-rotated Y-cut $LiNbO_3$ plate. The measured C_d/C was 7.37, somewhat higher than the theoretical value of 6.42.

4.2 Bending actuator structure

Figure 9 shows the basic structure of the actuator. The actuator consists of a $LiNbO_3$ plate that flexes when a voltage is applied across it. Three GI fibers are mounted on the top of the plate so that their alignment with three corresponding fibers on a stationary table changes when the plate is flexed. Adjacent fibers are secured 170 μm apart in V-shaped grooves anisotropically etched in Si. This spacing means that the optical path can be switched by a 170-μm displacement of the $LiNbO_3$ plate.

The gap between opposing fiber arrays is 40 μm. The optical array weighs about 10 mg. Stoppers on both sides of the plate ensure that the plate is moved by the correct amounts. These stoppers also dampen plate vibration and protect against external vibration.

4.3 Bending displacement

A 26 x 5 x 0.2 mm plate was cut from a $LiNbO_3$ wafer on which Au/NiCr electrode layers were deposited on both sides. One millimeter of one end was then inserted in a plated metallic holder and soldered in place. Leads

were bounded to both sides of the plate. A 2 x 3 mm square reflector plate weighing about 3 mg was bonded to the top of the actuator to enable displacement measurement using a laser-based displacement gauge. A 140 °-rotated *Y*-cut $LiNbO_3$ plate was used for the actuator. Figure 10 shows that the measurements agree well with the values calculated from Equation (2). No hysteresis was observed.

$$u = (3/2) \cdot |d_{23}| \cdot (l/t)^2 \cdot V, \quad \ldots\ldots\ldots (2)$$

where

u: Displacement
d_{23}: Piezoelectric strain constant
V: Applied voltage
t: Thickness of $LiNbO_3$ plate
l: Length of $LiNbO_3$ plate.

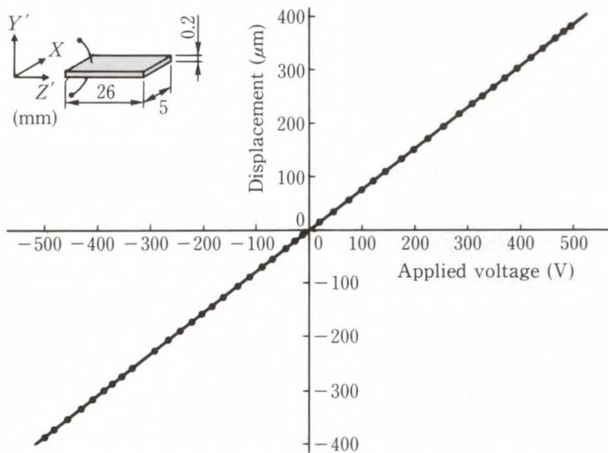

Fig. 10—Displacement vs. applied voltage for 140 °-rotated *Y*-cut $LiNbO_3$ actuator.

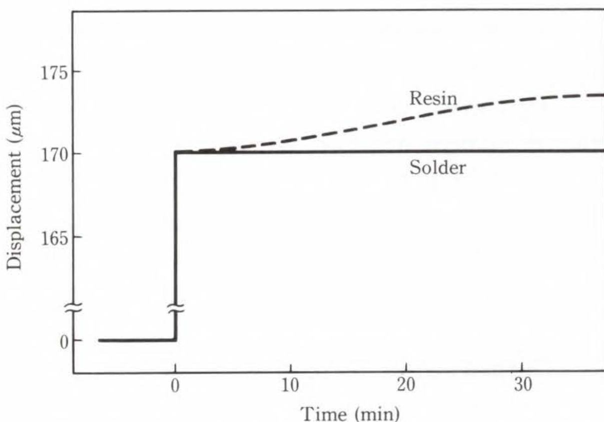

Fig. 11—Displacements of two types of actuators.

A voltage of 220 V was applied, and the creep in actuator displacement was monitored for 30 min. Two types of actuators were made. The $LiNbO_3$ plate of the first type was soldered to the base, and that of the other was fixed using resin. As can be seen in Figure 11, creep in the soldered actuator did not exceed 0.2 μm, but was significant in the resin fixed actuator.

Both actuators produced displacements with good linearity for the applied voltage. The actuators were then modified for a displacement of 170 μm.

4.4 Damping of actuator response.

Optical LAN applications require that loss is within 1.5 dB, that the switching time is within 10 ms, and that vibration after application of a

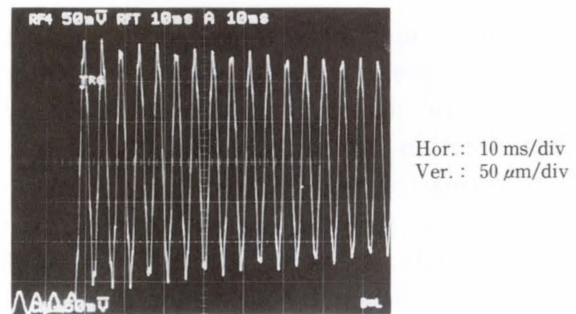

a) Without stoppers

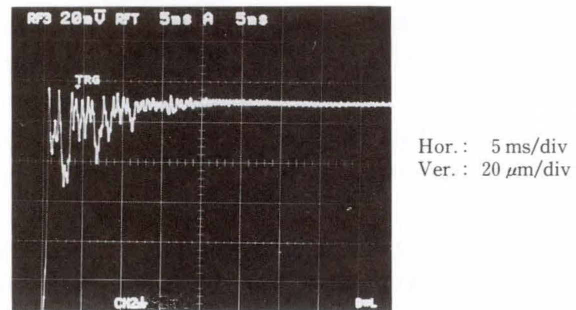

b) With stoppers

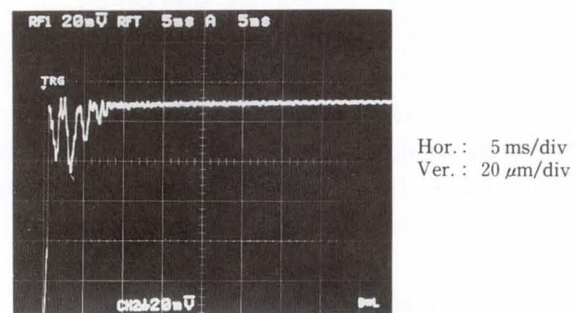

c) With stoppers and load

Fig. 12—Actuator responses to a step voltage.

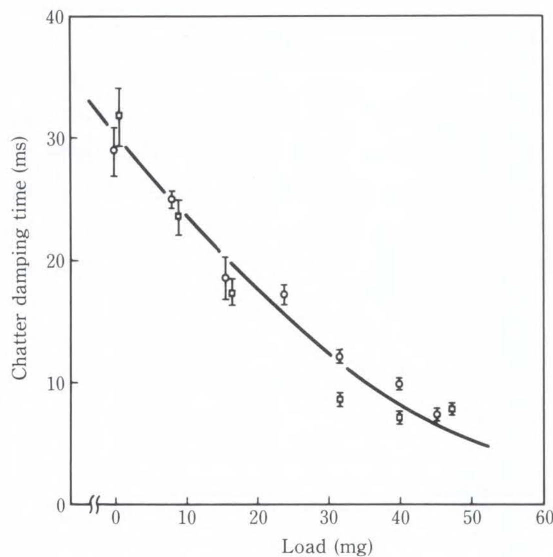

Fig. 13—Chatter in $LiNbO_3$ plate damped by various loads.

step voltage must be within 4 μm in 10 ms. The primary response to a high step voltage without stoppers or damping is shown in Fig. 12a). This vibration stops after about 200 ms, which is too long for an optical switch actuator. We then placed stoppers on both sides of the $LiNbO_3$ plate as shown in Fig. 9 and applied a voltage sufficient for a 170-μm displacement and a 450 mg stress between the plate and stoppers. Without stoppers, this voltage would produce a 250-μm displacement. The stoppers and the additional stress protect against external vibration. Figure 12b) shows the response of the actuator with stoppers. The impact between the $LiNbO_3$ plate and the stoppers produces chatter composed mainly of secondary resonances. The vibration fell to 4 μm or less after 30 ms. Therefore, an additional load of soft resin was bonded to the center of the $LiNbO_3$ plate to suppress chatter (see Fig. 9). Figure 13 shows the relationship between the load weight and chatter damping time. A load of 40 mg or more damped chatter within 10 ms. Figure 12c) shows how a 45 mg load damps actuator chatter to within the required limits.

4.5 Actuator specifications

A stress of 2 g or more is needed to move three fibers at the required speed.

Table 2. Optical switch actuator specifications

Item	Specification
Displacement	>170 μm
Switching time	<10 ms
Position accuracy	<4 μm
Produced stress	>2 g
Drive voltage	500 V
Drive current	0.5 nA

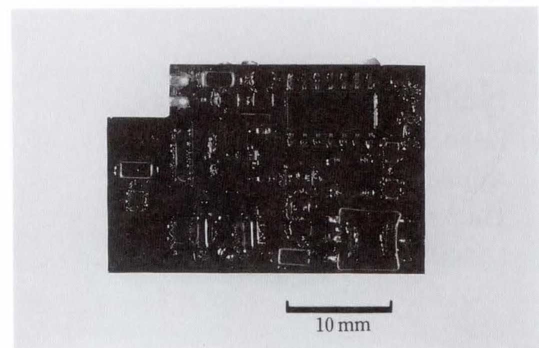

Fig. 14—Actuator drive circuit.

Therefore, the required actuator dimensions are 26 x 5 x 0.2 mm. Plate vibration is generated when the plate hits the stopper, resulting in fiber-axis deviation. Because the loss due to vibration must not exceed 0.3 dB, the axis deviation must not exceed 4 μm (see Figs 1 and 2). Therefore, plate vibration due to a step voltage must be damped to 4 μm or less within 10 ms. (see Table 2).

4.6 Electrical drive circuit

To move the fibers, when chatter is within acceptable limits, this piezoelectric actuator requires at least 500 V but no more than 0.5 nA.

This drive voltage can easily be supplied by the miniature inverter and small step-up transformer shown in Fig. 14. The input voltage of this circuit is 5 V, and the input current is 100 mA. The circuit measures 31 x 20 x 5.3 mm, and easily fits into the optical switch enclosure.

5. Optical switching path

Important requirements for an optical switch include precise spacing of the fibers on

the actuator and stationary table, smooth fiber end-faces, and precise alignment of the moving fibers with respect to the stationary fibers.

For precise spacing, the fibers were arranged in V-shaped grooves anisotropically etched in silicon. For smooth fiber end-faces the fibers were precision-cut using a dicing saw. For precise alignment, the fibers were mounted using a water-soluble resin.

5.1 Construction

Figure 15 shows how the optical path is constructed. First, a silicon crystal plate holds the optical fibers in V-shaped grooves. Second, the fiber array is secured to the transfer substrate using a water soluble resin. Third, the fiber array is cut with a dicing saw to produce the changeover section. (The array is cut using a dicing saw so that the end-faces are smooth and flat.) Fourth, a dicing saw is used to secure the array and the transfer substrate to the holder with resin. When the resin is cured, the array is immersed in water to dissolve the resin securing the transfer substrate so that the transfer substrate can be removed. (This takes up to two hours.) Fifth, the array is transferred to the holder and the assembly is dried at room temperature. The main optical paths are therefore constructed without the need for adjustment or fiber end-face polishing.

The fiber array stoppers are trimmed for the correct fiber movement after the switch is assembled.

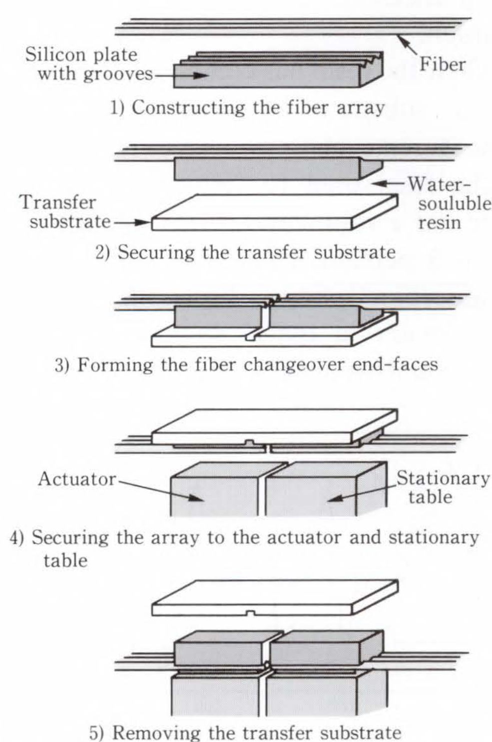

Fig. 15–Constructing the optical switching path.

5.2 Forming the V-shaped grooves

Three V-shaped grooves 150-μm wide is formed at intervals of 170 μm. Figure 16 shows the V-shaped grooves. A (100)-oriented silicon wafer is etched with an anisotropic etching solution in the < 001 > direction.

The anisotropic etching solution consists of ethylene diamine, pyrocatechol, and water.[5), 6)]

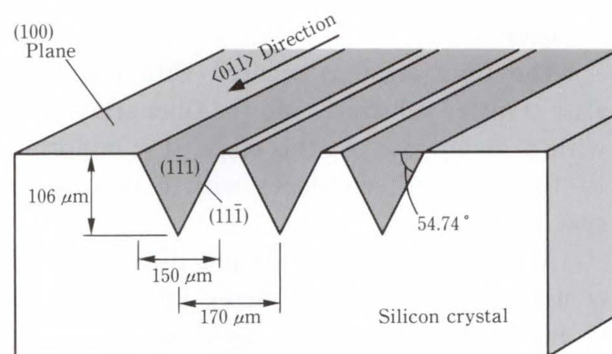

Fig. 16–V-shaped grooves.

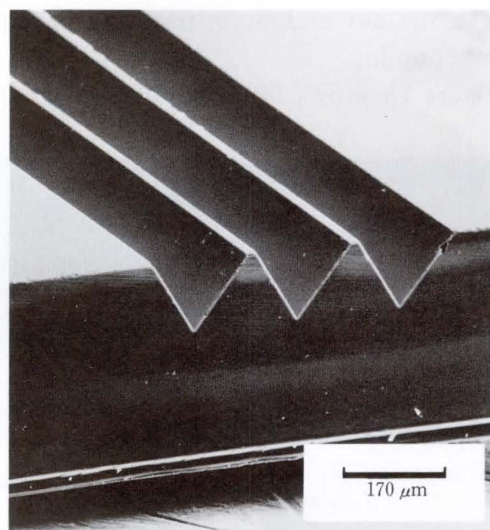

Fig. 17–Silicon wafer etched V-shaped groove (SEM).

Etching is performed at 118 °C for about three hours. During etching, nitrogen is used to bubble the etching solution to prevent oxidization, and the solution is stirred to keep the composition uniform. Buffered hydrofluoric acid is used for oxide film etching, and hot concentrated sulfuric acid is used for resist removal.

If the composition of the etching solution is incorrect or changes during etching, small, quadrangular, pyramid-like projections (micropyramids) develop on the etched surface, thus preventing the formation of smooth grooves.[7] Figure 17 shows successfully formed V-shaped grooves as seen under a scanning electron microscope. Using the above technique, V-shaped grooves can be formed with an arrangement precision of 2 μm or better.

5.3 Forming the end-faces of the fiber changeover

The fiber array is secured with resin to a glass transfer substrate, and the fiber array is cut with a dicing saw. At this stage, it is important to form smooth end-faces with a narrow cut spacing.

A dicing saw with a 35-μm diamond blade is used to cut the fiber array into two parts. A hard adhesive resin is used to secure the fibers to the V-shaped grooves, and the resin is completely cured before cutting. If the resin is not sufficiently cured, the resin may cling to the cut end-faces, resulting in reduced optical coupling.

Figure 18 shows fiber end-faces after cutting. For samples with a 40-μm spacing between fiber end-faces, the optical coupling losses ranged from 0.5 dB to 0.8 dB. We cut the synthetic quartz glass of these samples and inspected the roughness of the end-faces. Figure 19 shows that the roughness is within 0.1 μm. This figure suggests a low scattering loss because it is much smaller than the 1.3-μm optical wavelength.

5.4 Transfering the fiber arrays to the holder

The actuator is then assembled in the holder and adjusted to the initial position. The cut fiber array on the transfer substrate is secured to the actuator and the stationary table. Then, the array is attached to the holder so that the cut section is between the fixed and moving sections. To do this, we use a jig that supports the array, provides fine holder adjustment, and supports the holder. The planes of the supports on which the array and holder are retained are parallel. The position of the holder is finely adjusted in the X, Y, and Z directions and in the direction of horizontal rotation. When the holder is correctly positioned, resin is applied between the holder and the array to fasten them together. The holder positioning is then checked visually, and the resin allowed to harden.

When the resin has completely hardened, the transfer substrate is immersed in water to enable its removal.

The resin used to fasten the array to the holder has a volumetric shrinkage factor as low as 2 or 3 percent when fully cured. This resin can absorb a relative displacement of up to about 50 μm in the Z direction between the array mounting positions on the two sections.

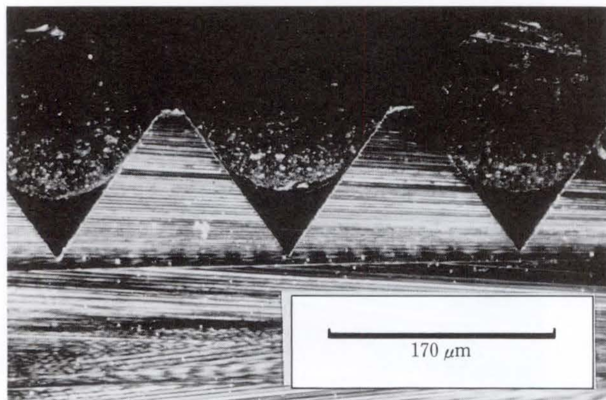

Fig. 18–Fiber end-faces after cutting.

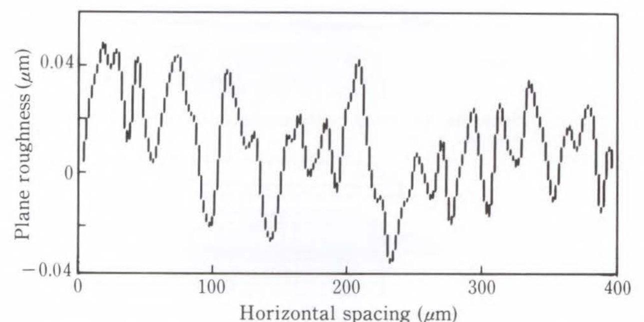

Fig. 19–Roughness of quartz glass cutting plane.

Table 3. Characteristics of the optical switch

Item	Specification
Optical characteristics Insertion loss Cross talk Switching speed	 0.8 dB < −50 dB 10 ms
Electrical characteristics Input voltage Input current	 5 V 100 mA
Case dimensions	55 x 30 x 6 mm

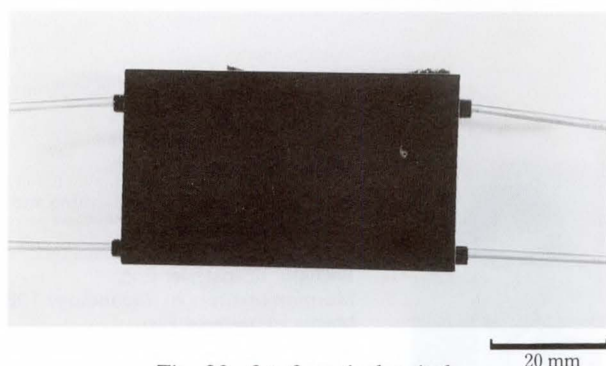

Fig. 20−2 x 2 optical switch.

This absorbtion keeps the relative displacement between the transferred arrays to within 2 μm. The increase in insertion loss due to the transfer is from 0.05 dB to 0.1 dB, and is mainly caused by optical axis displacement and bending along the *Z* axis.

6. Optical switch evaluation

Table 3 shows the basic characteristics of a 2 x 2 moving fiber optical switch using multi-mode fiber.

The insertion loss is within 0.8 dB and the switching time is within 10 ms. The insertion loss is greater than the estimated value of 0.4 dB. This discrepancy is caused by resin contamination of the fiber changeover end-faces during their manufacture, and by optical axis displacement in the *Z* direction and bending when the array is transferred. The increase in insertion loss caused by forming the fiber changeover end-faces is from 0.05 dB to 0.4 dB, and the increase caused by transfer is from 0.05 dB to 0.1 dB. The switching speed is affected by chatter caused by second harmonic vibration of the $LiNbO_3$ bimorph cell. The $LiNbO_3$ bimorph actuator provides faster switching and lower loss than conventional optical switches which use solenoids to move prisms or mirrors. This improvement makes it possible to downsize devices. Figure 20 shows a completed 2 x 2 optical switch.

7. Conclusion

A bending displacement actuator that was free of hysteresis and creep was developed using a $LiNbO_3$ plate having an inversion layer. Placing stoppers on both sides of the actuator and a load on the $LiNbO_3$ plate damps vibration so that the actuator can switch within 10 ms. A new construction technique was developed to simplify optical axis alignment and to obviate the need for fiber end-face polishing. The technique consists of the following three steps:

1) A highly precise fiber array is constructed by arranging fibers in V-shape grooves anisotropically etched in silicon. The arrangement precision is within 2 μm.
2) The fiber array is precision-cut to produce changeover sections having a cut surface roughness within 0.1 μm.
3) The cut fiber array is precisely mounted on a holder to form the optical circuit.

The only adjustment required is the trimming of the stoppers to obtain the correct fiber displacement. A 2 x 2 moving-fiber optical switch constructed using the above technique features an insertion loss that is within 0.8 dB.

Such a switch switches faster and has fewer components than ordinary optical switches that use solenoids to move prisms or mirrors. This improvement enables device miniaturization. The construction technique can also be applied to microoptical systems.

8. Acknowledgments

The authors would like to thank Professor H. Shimizu of Aomori University and Professor K. Nakamura of Tohoku University for their technical advice on the piezoelectric actuator.

References

1) Nakamura, K., Ando, H., and Shimuzu, H.: Bending Vibrator Consisting of a $LiNbO_3$ Plate with a Ferro-

electric Inversion Layer. *Jpn. J. Appl. Phys.*, **26**, Suppl., 26-2 pp. 198-200 (1987).

2) Nakamura, K., and Shimuzu, H.: Hysteresis-free Piezoelectric Actuators Using $LiNbO_3$ Plate with Ferroelectric Inversion Layer. *Ferroelectronics*, **93**, pp. 211-216 (1989).
3) Marcuse, D.: Loss Analysis of Single-mode Fiber Splices, *B. S. T. J.*, **56**, 5, pp. 703-718 (1977).
4) Ueda, M., Sawada, H., Tanaka, A., and Wakatsuki, N.: Piezoelectric Actuator Using a $LiNbO_3$ Bimorph for an Optical Switch. Proc., IEEE 1990 Ultrasonic Symp., **3**, pp. 1183-1186.
5) Naraoka, K.: Wet Etching. (in Japanese), *Oyo Buturi*, **53**, 10, pp. 877-883 (1984).
6) Bassous, E. and Baran, E. F.: The Fabrication of High Precision Nozzles by Anisotropic Etching of (100) Silicon. *J. Electrochem. Soc.*, **125**, 8, pp. 1321-1327 (1987).
7) Kishi, H., Okada, K., and Yagawara, S.: Micro-pyramid Inhibition Method in Anisotropic Etching of Silicon. (in Japanese), *J. Vacuum Soc. Jpn.*, **29**, 2, pp. 85-91 (1986).

Noboru Wakatsuki

Electronic Components Planning and Development Dep.
FUJITSU LIMITED
Bachelor of Electronic Eng.
Tohoku University 1967
Dr. of Electronic Eng.
Tohoku University 1972
Specializing in Piezoelectric and Optical Devices

Masanori Ueda

Electronic Components Planning and Development Dep.
FUJITSU LIMITED
Bachelor of material Eng.
Muroran Institute of Technology 1986
Master of material Eng.
Muroran Institute of Technology 1988
Specializing in Functional Components

Hisashi Sawada

Electronic Components Planning and Development Dep.
FUJITSU LIMITED
Bachelor of Physics
Toyama University 1980
Master of Physics
Tohoku University 1982
Specializing in Optical Devices

FUJITSU

SCIENTIFIC & TECHNICAL JOURNAL

VOL.27, NOs.1-4

INDEX

● SUBJECT INDEX ● AUTHOR INDEX

Spring 1991 VOL.27, NO.1

Summer 1991 VOL.27, NO.2
Special Issue on Supercomputer VP2000 Series

Autumn 1991 VOL.27, NO.3

Winter 1991 VOL.27, NO.4

Subject Index

(Ⓡ mark are Reviews.)

A

Atomic-Scale Simulations for Semiconductors by Supercomputer **2**, 211
●Minoru Ikeda ●Kumiko Furuya ●Takahiro Yamasaki
●Masuhiro Mikami

Atomic Structure and Interface States at CaF_2/Si (111) **3**, 260
●Hideaki Fujitani ●Setsuro Asano

B

Basic Software for FUJITSU VP2000 Series **2**, 197
●Koh-Ichiro Hotta ●Takashi Kunai ●Yoshio Honma

Boron/Magnesium Sintered Composites for Computer Peripherals **4**, 360
●Eiji Horikoshi ●Takehiko Sato

C

CIM System for PC Board Design and Manufacture **1**, 132
●Tsuyoshi Kobayashi ●Hideaki Kuwabara

Color Printing Characteristics of a Thermal Transfer Ink Sheet for Continuous-Tone Full Color Printers **3**, 290
●Michinori Kutami ●Shigeharu Suzuki ●Katsunori Yamagishi

Computational Fluid Dynamics and Computers **2**, 222
●Satoru Ogawa ●Yoko Takakura

Conductive Fur Brush Charging of a Dielectric Surface **1**, 107
●Masahiro Wanou ●Masatoshi Kimura

D

Design Automation System for FUJITSU VP2000 Series **2**, 187
●Hirofumi Hamamura ●Akihiko Hanafusa ●Minoru Saitoh
●Toshihiko Tada

Design of Organic Nonlinear Optical Materials for Electro-Optic and All-Optical Devices by Computer Simulation **1**, 115
●Tetsuzo Yoshimura

E

Electro Optical Switching of Bookshelf Layer Structure Ferroelectric Liquid-Crystal **3**, 233
●Akihiro Mochizuki ●Masakatsu Nakatsuka ●Yoichi Takanishi

H

Hardware Technology for FUJITSU VP2000 Series **2**, 158
●Akira Kaneko ●Kiyoshi Kuwabara ●Shun-ichi Kikuchi
●Takanobu Kano

High-Speed Monolithic GaInAs Twin PIN Photodiodes for Coherent Optical Receivers **1**, 84
●Masao Makiuchi ●Hisashi Hamaguchi ●Osamu Wada

High-Speed Structural Analysis Program: POPLAS®/FEM5 on Supercomputer **1**, 141
●Yasuhiro Komori ●Katsuhiko Akahori

J

® Josephson Integrated Circuits I Fabrication Technology **1**, 1
●Takeshi Imamura

® Josephson Integrated Circuits II High-Speed Digital Circuits **1**, 28
●Shinya Hasuo

® Josephson Integrated Circuits III A Single-Chip SQUID Magnetometer **1**, 59
●Norio Fujimaki

M

Moving-Fiber Optical Switch Using $LiNbO_3$ Piezoelectric Actuator **4**, 369
●Noboru Wakatsuki ●Hisashi Sawada ●Masanori Ueda

Multilayer Glass-Ceramic-Composite Circuit Board for FUJITSU VP2000 Series **2**, 179
●Koichi Niwa ●Yukichi Takeda

P

® Photoexcited Processes for Semiconductors I: Low Temperature Epitaxy **4**, 299
●Tatsuya Yamazaki ●Takashi Ito

® Photoexcited Processes for Semiconductors II: Dry Cleaning and Dry Etching **4**, 317
●Yasuhisa Sato ●Rinshi Sugino ●Takashi Ito

R

Rapid Analysis Methodology for Gene Sequences Using a Parallel Processor **3**, 270
●Masahito Kawai ●Atsuko Kishino ●Kimitoshi Naito

Report on Computer Algebra Research **4**, 338
●Taku Takeshima ●Masayuki Noro ●Kazuhiro Yokoyama

S

Semiconductor Devices for FUJITSU VP2000 Series **2**, 169
●Ken-ichi Ohno ●Kazuo Ooami ●Hideo Itoh
●Katsuhiko Suyama

® Semiconductor Laser Light Sources and Receivers for Next Generation Optical Communication Systems **4**, 329
●Hiroshi Ishikawa

SONET System for North America **1**, 92
●Masahiro Shinbashi ●Akihiko Ichikawa ●Kenji Sato

Synchrotron Radiation-Excited Deposition of Silicon Film **3**, 278
●Yasuo Nara ●Yoshihiro Sugita

System Overview of FUJITSU VP2000 Series **2**, 149
●Nobuo Uchida ●Yuji Oinaga ●(Hiroshi Tamura
●Kazuyuki Shimizu

T

A Test Generation System Using a Logic Simulation Engine **3**, 285
●Koichiro Takayama ●Fumiyasu Hirose ●Nobuaki Kawato

Theoretical and Experimental Study of the Optical Absorption Spectrum of Exciton Resonance in $In_{0.53}Ga_{0.47}As/InP$ Quantum Wells **3**, 243
●Mitsuru Sugawara ●Takuya Fujii

Author Index

(Ⓡ mark are Reviews.)

A

Akahori Katsuhiko see **Komori** Yasuhiro
Asano Setsuro see **Fujitani** Hideaki

F

Fujii Takuya see **Sugawara** Mitsuru
Fujimaki Norio
Ⓡ Josephson Integrated Circuits III A Single-Chip SQUID Magnetometer **1**, 59
Fujitani Hideaki
Atomic Structure and Interface States at CaF_2/Si (111) **3**, 260
Furuya Kumiko see **Ikeda** Minoru

H

Hamaguchi Hisashi see **Makiuchi** Masao
Hamamura Hirofumi
Design Automation System for FUJITSU VP2000 Series **2**, 187
Hanafusa Akihiko see **Hamamura** Hirofumi
Hasuo Shinya
Ⓡ Josephson Integrated Circuits II High-Speed Digital Circuits **1**, 28
Hirose Fumiyasu see **Takayama** Koichiro
Honma Yoshio see **Hotta** Koh-Ichiro
Horikoshi Eiji
Boron/Magnesium Sintered Composites for Computer Peripherals **4**, 360
Hotta Koh-Ichiro
Basic Software for FUJITSU VP2000 Series **2**, 197

I

Ichikawa Akihiko see **Shinbashi** Masahiro
Ikeda Minoru
Atomic-Scale Simulations for Semiconductors by Supercomputer **2**, 211
Imamura Takeshi
Ⓡ Josephson Integrated Circuits I Fabrication Technology **1**, 1
Ishikawa Hiroshi
Ⓡ Semiconductor Laser Light Sources and Receivers for Next Generation Optical Communication System **4**, 329
Ito Takashi see **Sato** Yasuhisa
Ito Takashi see **Yamazaki** Tatsuya
Itoh Hideo see **Ohno** Ken-ichi

K

Kaneko Akira

Hardware Technology for FUJITSU VP2000 Series **2**, 158

Kano Takanobu see **Kaneko** Akira

Kawai Masahito

Rapid Analysis Methodology for Gene Sequences Using a Parallel Processor **3**, 270

Kawato Nobuaki see **Takayama** Koichiro

Kikuchi Shun-ichi see **Kaneko** Akira

Kimura Masatoshi see **Wanou** Masahiro

Kishino Atsuko see **Kawai** Masahito

Kobayashi Tsuyoshi

CIM System for PC Board Design and Manufacture **1**, 132

Komori Yasuhiro

High-Speed Structural Analysis Program POPLAS®/FEM5 on Supercomputer **1**, 141

Kunai Takashi see **Hotta** Koh-Ichiro

Kutami Michinori

Color Printing Characteristics of a Thermal Transfer Ink Sheet for Continuous-Tone Full Color Printers **3**, 290

Kuwabara Hideaki see **Kobayashi** Tsuyoshi

Kuwabara Kiyoshi see **Kaneko** Akira

M

Makiuchi Masao

High-Speed Monolithic GaInAs Twin PIN Photodiodes for Coherent Optical Receivers **1**, 84

Mikami Masuhiro see **Ikeda** Minoru

Mochizuki Akihiro

Electro Optical Switching of Bookshelf Layer Structure Ferroelectric Liquid-Crystal **3**, 233

N

Naito Kimitoshi see **Kawai** Masahito

Nakatsuka Masakatsu see **Mochizuki** Akihiro

Nara Yasuo

Synchrotron Radiation-Excited Deposition of Silicon Film **3**, 278

Niwa Koichi

Multilayer Glass-Ceramic-Composite Circuit Board for FUJITSU VP2000 Series **2**, 179

Noro Masayuki see **Takeshima** Taku

O

Ogawa Satoru

Computational Fluid Dynamics and Computers **2**, 222

Ohno Ken-ichi

Semiconductor Devices for FUJITSU VP2000 Series **2**, 169

Oinaga Yuji see **Uchida** Nobuo

Ooami Kazuo see **Ohno** Ken-ichi

S

Saitoh Minoru see **Hamamura** Hirofumi
Sato Kenji see **Shinbashi** Masahiro
Sato Takehiko see **Horikoshi** Eiji
Sato Yasuhisa
® Photoexcited Processes for Semiconductors II: Dry Cleaning and Dry Etching **4**, 317
Sawada Hisashi see **Wakatsuki** Noboru
Shimizu Kazuyuki see **Uchida** Nobuo
Shinbashi Masahiro
SONET System for North America **1**, 92
Sugawara Mitsuru
Theoretical and Experimental Study of the Optical Absorption Spectrum of Exciton Resonance in $In_{0.53}Ga_{0.47}As/InP$ Quantum Wells **3**, 243
Sugino Rinshi see **Sato** Yasuhisa
Sugita Yoshihiro see **Nara** Yasuo
Suyama Katsuhiko see **Ohno** Ken-ichi
Suzuki Shigeharu see **Kutami** Michinori

T

Tada Toshihiko see **Hamamura** Hirofumi
Takakura Yoko see **Ogawa** Satoru
Takanishi Yoichi see **Mochizuki** Akihiro
Takayama Koichiro
A Test Generation System Using a Logic Simulation Engine **3**, 285
Takeda Yukichi see **Niwa** Koichi
Takeshima Taku
Report on Computer Algebra Research **4**, 338
Tamura Hiroshi see **Uchida** Nobuo

U

Uchida Nobuo
System Overview of FUJITSU VP2000 Series **2**, 149
Ueda Masanori see **Wakatsuki** Noboru

W

Wada Osamu see **Makiuchi** Masao
Wakatsuki Noboru
Moving-Fiber Optical Switch Using $LiNbO_3$ Piezoelectric Actuator **4**, 369
Wanou Masahiro
Conductive Fur Brush Charging of a Dielectric Surface **1**, 107

Y

Yamagishi Katsunori see **Kutami** Michinori
Yamasaki Takahiro see **Ikeda** Minoru
Yamazaki Tatsuya
® Photoexcited Processes for Semiconductors I: Low Temperature Epitaxy **4**, 299
Yokoyama Kazuhiro see **Takeshima** Taku
Yoshimura Tetsuzo
Design of Organic Nonlinear Optical Materials for Electro-Optic and All-Optical Devices by Computer Simulation **1**, 115

FUJITSU

Overseas Offices

Abu Dhabi Office
P.O. Box 47047 Suite 802,
A1 Masaood Tower, Sheikh Hamdan Street, Abu Dhabi, U.A.E.
Telephone : (971-2)-333440
FAX : (971-2)-333436

Algiers Office
9, Rue Louis Rougie Chateau Neuf, EL Biar, Alger 16030, Algeria
Telephone : (213)-2-78-5542
Telex : 408-67522

Amman Office
P.O. Box 5420, Ammān, Jordan
Telephone : (962)-6-662417
FAX : (962)-6-673275

Bangkok Office
3rd Floor, Dusit Thani Bldg., 1-3, Rama IV, Bangkok, Thailand
Telephone : (66-2)-236-7930
FAX : (66-2)-238-3666

Beijing Office
Room 2101, Fortune Building
5 Dong San Huan Bei-lu, Chao Yang District, Beijing, People's Republic of China
Telephone : (86-1)-501-3261
FAX : (86-1)-501-3260

Bogotá Office
Cra. 13 No. 27-50,
Edificio Centro Internacional Tequendama, Oficina 326/328
Bogotá, D.E. Colombia
Telephone : (57-1)-286-7061
FAX : (57-1)-286-7148

Brussels Office
Avenue Louise 176, Bte 2
1050 Brussels, Belgium
Telephone : (32-2)-648-7622
FAX : (32-2)-648-6876

Hawaii Branch
6660 Hawaii Kai Drive, Honolulu, Hawaii 96825, U.S.A.
Telephone : (1-808)-395-2314
FAX : (1-808)-396-7111

Indonesia Project Office
16th Floor, Skyline Bldg., Jalan M.H. Thamrin No. 9, Jakarta, Indonesia
Telephone : (62-21)-3105710
FAX : (62-21)-3105983

Jakarta Office
16th Floor, Skyline Bldg., Jalan M.H. Thamrin No. 9, Jakarta, Indonesia
Telephone : (62-21)-333245
FAX : (62-21)-327904

Kuala Lumpur Office
Letter Box No. 47, 22nd Floor, UBN Tower No. 10, Jalan P. Ramlee, 50250, Kuala Lumpur, Malaysia
Telephone : (60-3)-238-4870
FAX : (60-3)-238-4869

Munich Office
c/o DV18 Siemens A.G.
Otto-Hahn-Ring 6, D-8000, München 83, Germany
Telephone : (49-89)-636-3244
FAX : (49-89)-636-45345

New Delhi Office
1st Floor, 15 Katsurba Gandhi Marg
New Delhi-110001, India
Telephone : (91-11)-331-1311
FAX : (91-11)-332-1321

New York Office
680 Fifth Avenue, New York, N.Y. 10019, U.S.A.
Telephone : (1-212)-265-5360
FAX : (1-212)-541-9071

Paris Office
Bâtiment Aristote, Rue Olof Palme 94006, Creteil Cedex, France
Telephone : (33-1)-4-399-0897
FAX : (33-1)-4-399-0700

Shanghai Office
Room 1504 Ruijin Bldg., 205 Maoming Road South, Shanghai, People's Republic of China
Telephone : (86-21)-433-6462
FAX : (86-21)-433-6480

Taipei Office
Sunglow Bldg., 66, Sung Chiang Road, Taipei, Taiwan
Telephone : (886-2)-551-0233
FAX : (886-2)-536-7454

Washington, D.C. Office
1776 Eye Street, N.W., Suite 880, Washington, D.C., 20006, U.S.A.
Telephone : (1-202)-331-8750
FAX : (1-202)-331-8797

Overseas Subsidiaries

		Telephone	Facsimile
FKL Dong-Hwa Ltd.	338-13, Daehong-Ri, Sunghwan-Eub, Chunwon-Gun, Chungnam, Republic of Korea	(82-417)-581-0701	(82-417)-581-0700
Fujian Fujitsu Communications Software Ltd.	Wuliting Fuma Road, Fuzhou, Fujian Province, People's Republic of China	(86-591)-660070	(86-591)-660022
Fujitsu Network Transmission Systems, Inc.	2801 Telecom Parkway Richardson, TX 75082, USA	(1-214)-690-6000	(1-214)-497-6900
Fujitsu Australia Ltd.	475 Victoria Ave., Chatswood, NSW 2067, Australia	(61-2)-410-4555	(61-2)-411-8603
Fujitsu Australia Software Technology Pty. Ltd.	1st Floor. Techway House 18 Rodborough Road, Frenchs Forest, N.S.W. 2086, Australia	(61-2)-936-1111	(61-2)-975-2899
Fujitsu Business Communication Systems, Inc.	3190 Miraloma Ave., Anaheim, CA 92806-1906, USA	(1-714)-630-7721	(1-714)-630-7660
Fujitsu Canada, Inc.	2800 Matheson Boulevard East, Mississauga, Ontario L4W 4×5 Canada	(1-416)-602-5454	(1-416)-602-5457
Fujitsu Computer Packaging Technologies, Inc.	Building 8A, 3811 Zanker Road, San Jose, CA 95134-1402, USA	(1-408)-943-7700	(1-408)-943-7790
Fujitsu Component (Malaysia) Sdn. Bhd.	No. 1, Lorong Satu, Kawasan Perindustrian Parit Raja, 86400 Batu Pahat, Johor, Malaysia	(60-7)-482-111	(60-7)-481-771
Fujitsu Component of America, Inc.	3545 North First Street, San Jose, CA 95134-1804, USA	(1-408)-922-9000	(1-408)-428-0640
Fujitsu Customer Service of America, Inc.	11085 N. Torrey Pines Rd. La Jolla, CA 92037, USA	(1-619)-457-9900	(1-619)-457-9968
Fujitsu Deutschland GmbH	Frankfurter Ring 211, 8000 München 40, F.R. Germany	(49-89)-323-780	(49-89)-323-78100
Fujitsu do Brasil Ltda.	Rua Manoel da Nóbrega, 1280-2Ä Andar, C.E.P. 04001, São Paulo, Brazil	(55-11)-885-2933	(55-11)-885-9132
Fujitsu España, S.A.	Edificio Torre Europa 5ª, Paseo de la Castellana, 95, 28046 Madrid, Spain	(34-1)-581-8000	(34-1)-581-8300
Fujitsu Europe Ltd.	2, Longwalk Road, Stockley Park, Uxbridge, Middlesex, UB11 1AB, England	(44-81)-573-4444	(44-81)-573-2643
Fujitsu Europe Telecom R&D Centre Limited	2, Longwalk Road., Stockley Park, Uxbridge, Middlesex, UB11 1AB, England	(44-81)-573-4444	(44-81)-573-3602
Fujitsu Finance (U.K.) PLC	2, Longwalk Road, Stockley Park, Uxbridge, Middlesex, UB11 1AB, England	(44-81)-569-1628	(44-81)-573-2643
Fujitsu France S.A.	Bâtiment Aristote 17, Rue Olof Palme 94006, Creteil Cedex, Paris, France	(33-1)-4-399-4000	(33-1)-4-399-0700
Fujitsu Hong Kong Ltd.	Room 2521, Sun Hung Kai Centre, 30 Harbour Road, Hong Kong	(852)-8275780	(852)-8274724
Fujitsu Imaging Systems of America, Inc.	3 Corporate Drive, Commerce Park, Danbury, CT 06810, USA	(1-203)-796-5400	(1-203)-796-5665
Fujitsu International Finance (Netherlands) B.V.	Officia 1, De Boelelaan 7, 1083 HJ Amsterdam, The Netherlands	(31-20)-465996	(31-20)-427675
Fujitsu Italia S.p.A.	Via Melchiorre, Gioia No.8, 20124 Milano, Italy	(39-2)-657-2741	(39-2)-657-2257
Fujitsu Korea Ltd.	9th Floor, Korean Reinsurance Bldg., 80, Susong-Dong, Chongro-Gu, Seoul Special City, Republic of Korea	(82-2)-739-3281	(82-2)-739-3294
Fujitsu Microelectronics Asia Pte. Ltd.	No.2, Second Chin Bee Road, Jurong Town, Singapore 2261, Singapore	(65)-265-6511	(65)-265-6275
Fujitsu Microelectronics, Inc.	3545 North First Street, San Jose, CA 95134-1804, USA	(1-408)-922-9000	(1-408)-432-9044
Fujitsu Microelectronics Ireland Limited	Greenhills Centre, Greenhills Road, Tallaght, Dublin 24, Ireland	(353-1)-520744	(353-1)-520539
Fujitsu Microelectronics Italia S.r.l.	Centro Direzionale, Milanofiori, Strada No.4-Palazzo A2, 20090 Assago-Milano, Italy	(39-2)-824-6170	(39-2)-824-6189
Fujitsu Microelectronics Limited	Hargrave House, Belmont Road, Maidenhead, Berkshire SL6 6NE, U.K.	(44-628)-76100	(44)-628-781484
Fujitsu Microelectronics (Malaysia) Sdn. Bhd.	Persiaran Kuala Selangor, Seksyen 26,40000 Shah Alam, Selangor Darul Ehsan, Malaysia	(60-3)-511-1155	(60-3)-511-1227
Fujitsu Microelectronics Pacific Asia Limited	Rooms 616-617, Tower B, New Mandarin Plaza, 14 Science Museum Road, Tsimshatsui East, Kowloon, Hong Kong	(852-3)-723-0393	(852-3)-721-6555
Fujitsu Mikroelectronik Gm bH	Am Siebenstein 6-10, 6072 Dreieich Buchschlag, Germany	(49-6103)-690-0	(49-6103)-690-122
Fujitsu Network Switching of America, Inc.	4403 Bland Road, Somerset Park, Raleigh, NC 27609, USA	(1-919)-790-2211	(1-919)-790-8376
Fujitsu New Zealand Ltd.	6th Floor, National Insurance House, 119-123 Featherston Street, Wellington, New Zealand	(64-4)-473-3240	(64-4)-473-3429
Fujitsu Nordic AB	Torggatan 8, S-171 54 Solna, Sweden	(46-8)-764-7690	(46-8)-28-0345
Fujitsu Philippines, Inc.	2nd Floor, United Life Bldg., Pasay Road, Legaspi Village, Makati, Metro Manila, Philippines	(63-2)-812-4001	(63-2)-817-7576
Fujitsu (Singapore) Pte.Ltd.	75, Science Park Drive, #02-06 CINTECH II Singapore 0511. Singapore	(65)-777-6577	(65)-778-2055
Fujitsu Systems Business of America, Inc.	2986 Oakmead Village Court, Santa Clara, CA 95051, USA	(1-408)-988-8012	(1-408)-492-1982
Fujitsu Systems Business (Malaysia) Sdn. Bhd.	No. 11-4 Right Angel Building, Jalan 14/22 Section 14, Petaling Jaya, Malaysia	(60-3)-755-0844	(60-3)-755-6010
Fujitsu Systems Business (Thailand) Limited	492, 494 Mini Office, Rachada Complex, Rachadapisek Road, Bangkok, Thailand	(662)-513-9148	(662)-513-9147
Fujitsu Systems of America, Inc.	12670 High Bluff Drive, San Diego, CA 92130-2103, USA	(1-619)-481-4004	(1-619)-259-2603
Fujitsu (Thailand) Co., Ltd.	60/90 (Nava Nakorn Industrial Estate Zone 3) Moo 19, Phaholyothin Road, Tambon Klongnung, Kmphur Klongluang, Pathumthani 12120, Thailand	(66-2)-529-2630	(66-2)-529-2581
Fujitsu Vitória Computodores e Serviços Ltda.	Avenida Nossa, Senhora da Penha, 570-8-S/801 Praia do Canto-Vitória-Espirito Santo, Brazil	(55-27)-225-0355	(55-27)-225-0954
Information Switching Technology Pty. Ltd.	Level 32, 200 Queen Street, Melbourne 3000, Australia	(61-3)-670-4755	(61-3)-670-6183
Intellistor, Inc.	2402 Clover Basin Drive commerce Park, Longmont, Colorado 80503, USA	(1-303)-682-6400	(1-303)-682-6401
Tatung-Fujitsu Co., Ltd.	5 Floor Tatung Bldg., 225, Nanking East Road 3rd Section, Taipei, Taiwan	(886-2)-713-5396	(886-2)-717-4644

(The information here as of November 30, 1991)

FUJITSU LIMITED

6-1, Marunouchi 1-chome, Chiyoda-ku, Tokyo 100, Japan
Phone: National (03) 3216-3211 International (Int'l Prefix) 81-3-3216-3211 Telex: J22833 Cable: "FUJITSULIMITED TOKYO"